ECAP-2017-003

Analysis of neutron induced background in CANDLES

Master's Thesis in Physics

by

Michael Moser

Osaka, March 17, 2017

Department of Physics
Erlangen Centre for Astroparticle Physics
Friedrich-Alexander-Universität Erlangen-Nürnberg

Department of Physics, Graduate School of Science
Nuclear and Particle Physics, Kishimoto Group
Osaka University

Supervisor: Prof. Tadafumi Kishimoto
Chief Examiner: Prof. Dr. Gisela Anton
Co-Examiner: Dr. Thomas Eberl

Contents

1. Abstract

Neutrinoless double beta decay is a process beyond the Standard Model of particle physics which could prove the existence of massive Majorana neutrinos and lepton number violation. The CANDLES experiment studies the double beta decay of ^{48}Ca contained in CaF_2 crystals in order to observe neutrinoless double beta decay.
Measurements have to be made in a very low background condition, as neutrinoless double beta decay is a strongly suppressed mechanism. After the construction of the CANDLES III detector, located in the Kamioka underground laboratory, unexpected high energy events ($E > Q_{\beta\beta}$) were observed. They have been identified as γ-rays that are caused by (n,γ) neutron capture events in the rock surrounding the detector and in the stainless steel tank that contains the experimental apparatus. Since this background is almost three times larger than the second most significant background caused by ^{208}Tl, a passive shield has been installed. The shielding consists of about 10 cm of lead and about 5 mm of boron sheet. Shield construction was finished in March 2016 and the expected remaining background in the region of interest ($Q_{\beta\beta} = 4274$ keV) is 0.34 $\pm$ 0.14 events/year (rock) and 0.4 $\pm$ 0.2 events/year (tank). The total background caused by (n,γ) reactions is expected to be reduced by 1/80 based on Monte Carlo simulations.

In this work, the results of an analysis that investigates the reduction of (n,γ) events due to the additional lead and boron shield are presented. ^{252}Cf source run data as well as normal physics run data (132.6 d) is used in order to deduce a reduction factor for both rock and tank (n,γ) events. Based on simulations, the expected reduction in the high energy region (5.5 MeV $-$ 10 MeV) for rock and tank is about 1/350 and 1/40 respectively.
Analysis shows that the reduction is $0.028^{+0.012}_{-0.013}$ for rock ($\approx$ 1/36) and $0.027^{+0.015}_{-0.014}$ for tank ($\approx$ 1/37) at 68% CI. Due to the very low statistics of (n,γ) reactions after the shielding, errors on the reduction are high and a reduction of 1/350 for rock is well contained in the 95% CI.
As a consequence, the analysis should be repeated in the future with more data.

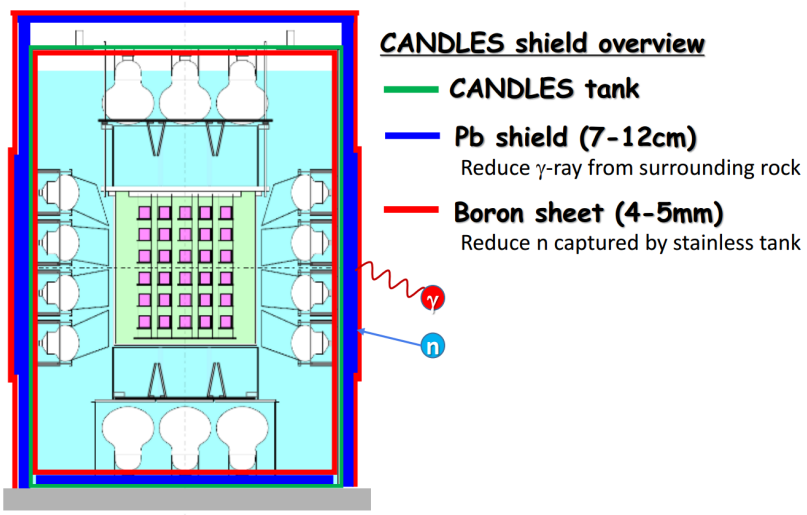

Figure 1.1.: Schematic view of the CANDLES shield system

2. Introduction

Neutrinoless double beta decay (0νββ) is a second-order weak process where two neutrons decay into two protons and two electrons without the additional emission of neutrinos.
In contrast to classical double beta decay (2νββ), this mechanism has not been observed yet.

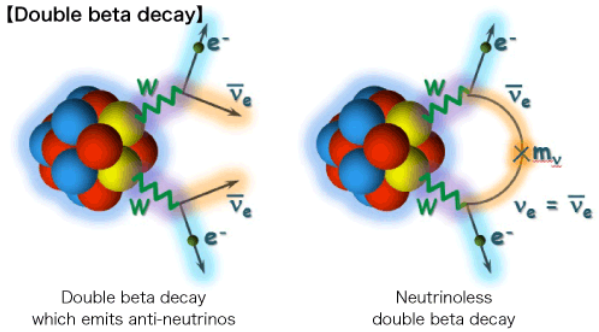

Figure 2.1.: Illustration of the observed double beta decay (left, 2νββ) compared to neutrinoless double beta decay (right, 0νββ). In the latter case, no neutrinos are emitted. [1]

A verification of 0νββ would have profound consequences on the theoretical foundation of particle physics, as it would be the first measurement of an effective neutrino mass.
Furthermore, this process can only occur if neutrinos are Majorana particles. These kind of particles were first proposed by Ettore Majorana in 1937 as part of a neutrino theory. In his work, no distinction between neutrinos and antineutrinos is made if neutrinos are massive [2][3]. In this case, the so-called Majorana condition $\nu^c = \nu$ with $\nu^c = C\bar{\nu}^T$ as the CP conjugate of the spinor ν is met. There are no experimentally confirmed Majorana fermions yet, as all Standard Model fermions, except the neutrinos, are confirmed to be of Dirac nature. Thus, as the massive nature of neutrinos has recently been proven experimentally through neutrino oscillations [4][5][6], neutrinos could be the first observed Majorana fermions.
This would give insight on the origin of small neutrino masses, as Majorana neutrinos are required for the seesaw mechanism which creates their masses in theories beyond the Standard Model.

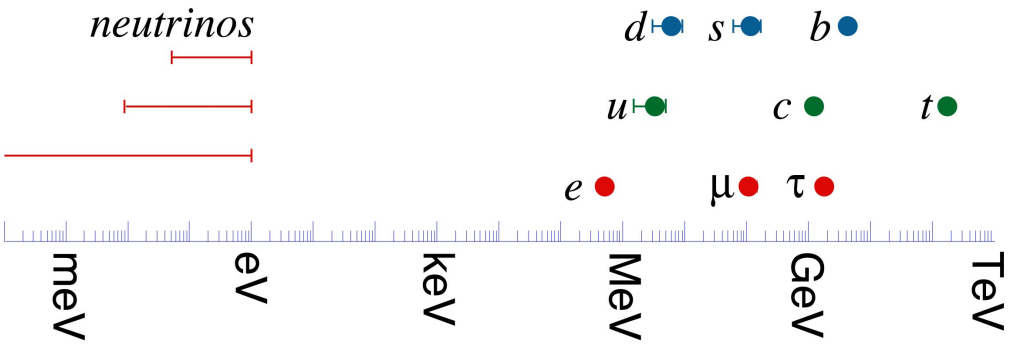

Figure 2.2.: Mass comparison for all fundamental fermions. X-axis: Masses in electronvolt. The upper limit on the mass of the heaviest neutrino is more than six magnitudes smaller than the mass of the next lightest particle, the electron. [7]

At last, neutrinoless double beta decay violates lepton number conservation by two units.
However, this is not unexpected, as the lepton number is only an accidentally conserved global symmetry in the Standard Model [8]. The same applies to the conservation of baryon number, which is expected to be violated due to the matter-antimatter asymmetry in the universe [9]. Hence, if nature does not treat lepton and baryon number in a completely different way, lepton number violation can be expected as well [8].

3. Theoretical framework

3.1. Basic neutrino properties

Neutrinos play a puzzling role in the Standard Model of particle physics, since some of their basic properties are very different to those of the other elementary particles.
The most distinct property of neutrinos is their small mass, as the current cosmological upper limit for three neutrino generations is $\sum m_\nu = (0.320 \pm 0.081)\,\mathrm{eV}\,c^{-2}$ [10]. This is very small compared to the next lightest particle in the Standard Model, the electron, with a mass of $m_e = 0.511 \times 10^6\,\mathrm{eV}\,c^{-2}$ [11]. Furthermore, the neutrino only interacts via the weak force, since it carries no electric charge or hypercharge.
Then, each neutrino is part of a leptonic $SU(2)_L$ doublet with three confirmed generations.

$$\textit{Lepton Doublets:} \quad \begin{bmatrix} e \\ \nu_e \end{bmatrix} \begin{bmatrix} \mu \\ \nu_\mu \end{bmatrix} \begin{bmatrix} \tau \\ \nu_\tau \end{bmatrix}$$

However, unlike quarks or the neutrinos' doublet partners like the electron, neutrinos can change their family through a mechanism called "neutrino oscillation".

3.2. Neutrino oscillations

While neutrino oscillations were first considered by Bruno Pontecorvo in 1957 [12], it was not until the last decade that this mechanism has been observed experimentally by atmospheric, solar, reactor and accelerator experiments [13]. These observations established that the neutrino has a mass. This is in contrast to the Standard Model, which assumes that neutrinos are massless.

The principal idea of neutrino oscillations is that there are two different kinds of neutrino eigenstates: flavor eigenstates $\nu_{e,\mu,\tau}$ and mass eigenstates $\nu_{1,2,3}$. The flavor eigenstates only take part in interactions, while the mass eigenstates propagate through space. The relation between the flavor and mass eigenstates is described by a 3×3 matrix U, similar to the CKM matrix in the quark sector:

$$\nu_\alpha = U^*_{\alpha i} \nu_i \tag{3.1}$$

with $\alpha = e, \mu, \tau$, $i = 1, 2, 3$ and the PMNS (Pontecorvo–Maki–Nakagawa–Sakata) matrix U.

As the PMNS matrix is not the identity matrix, flavor eigenstates and mass eigenstates differ from each other. Hence, one can show that the probability for measuring a particular flavor of a neutrino created at t_0 differs from the probability for the same flavor at some point in time $t_0 + t$. This means that neutrinos can change their flavor while propagating through space.
In vacuum, the probability of the transition $\nu_l \to \nu_{l'}$ is given by the following formula [14]:

$$\begin{aligned} P_{\nu_\alpha \to \nu_{\alpha'}} = \delta_{\alpha\alpha'} &- 4 \sum_{i>k} \mathrm{Re}[U^*_{\alpha i} U_{\alpha' i} U_{\alpha k} U^*_{\alpha' k}] \sin^2\left(\frac{\Delta m^2_{ki} L}{4E}\right) \\ &+ 2 \sum_{i>k} \mathrm{Im}[U^*_{\alpha i} U_{\alpha' i} U_{\alpha k} U^*_{\alpha' k}] \sin\left(\frac{\Delta m^2_{ki} L}{2E}\right) \end{aligned} \tag{3.2}$$

where E is the neutrino energy, L is the oscillation length, $\Delta m^2_{ki} = m^2_i - m^2_k$ is the mass difference between the eigenstates i and k, and α is the neutrino flavor index.

Therefore, only the mass differences Δm_{ki}, but not the absolute masses m_k can be measured in neutrino oscillation experiments. Thus, the absolute hierarchy of the masses is not known.
There are two possible configurations, the "normal" and the "inverted" hierarchy, cf. figure 3.1.

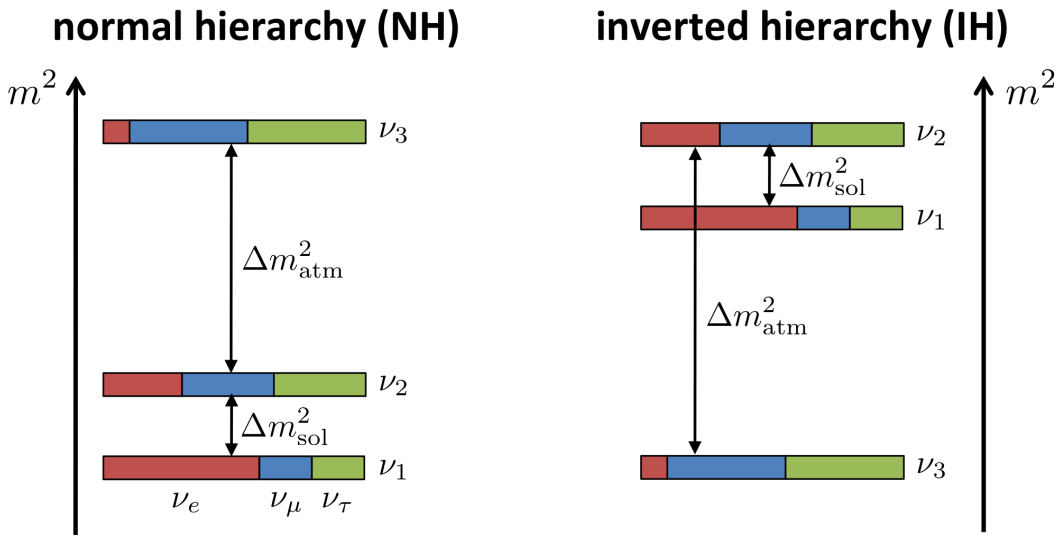

Figure 3.1.: Normal (left) and inverted (right) hierarchy of the neutrino mass eigenstates. Δm^2_{sol} and Δm^2_{atm} are synonyms for Δm^2_{21} and Δm^2_{32} respectively. The absolute mass scale (i.e. m^2_{lightest}) is not known. [15]

It is not established yet which hierarchy is the correct one, however future experiments will determine the neutrino mass hierarchy in the next decade [16]. As we will see later on, the half-life of 0νββ depends on the arrangement of the hierarchy. Hence, the determination of the neutrino mass hierarchy is also important within the context of neutrinoless double beta decay.

3.3. Neutrino mass generation: the seesaw mechanism

While the fact that neutrinos have masses has been established in the last decade, it doesn't give a clue about the actual mechanism behind the neutrino mass generation.
In principal, neutrinos can obtain masses through the standard Higgs mechanism. However, the associated Yukawa coupling constant would have to be very small, $h \sim 10^{-12}$ [17]. This is generally considered to be unnatural [17][18][19].

A more popular approach is the seesaw mechanism, especially the standard seesaw type 1 mechanism, which will be introduced now.

The first assumption that one has to make, is that a right-handed neutrino ν_R exists apart from the usual left-handed neutrino ν_L. The right-handed neutrino has not been observed yet, but it is also not forbidden by the Standard Model.
For the ease of readability, it is assumed that only one neutrino generation exists.

Now, it is possible to construct the Dirac mass term and the two Majorana ones [20][21][22][23]:

$$\mathcal{L}^{D}_{\text{vmass}} = \frac{1}{2} m_D (\overline{\nu_R}\nu_L + \overline{\nu^c_L}\nu^c_R) + \text{h.c.} \tag{3.3}$$

$$\mathcal{L}^{L}_{\text{vmass}} = \frac{1}{2} m_L \overline{\nu^c_L}\nu_L + \text{h.c.} \tag{3.4}$$

$$\mathcal{L}^{R}_{\text{vmass}} = \frac{1}{2} m_R \overline{\nu_R}\nu^c_R + \text{h.c.} \tag{3.5}$$

with $\nu^c_{L,R} = (\nu_{L,R})^c = C\bar{\nu}^T_{L,R}$ as the CP conjugate and h.c. signifying the Hermitian conjugate.

A summation of these terms in a matrix form yields the following:

$$\mathcal{L}^{\text{D+M}}_{\text{vmass}} = \mathcal{L}^{D}_{\text{vmass}} + \mathcal{L}^{L}_{\text{vmass}} + \mathcal{L}^{R}_{\text{vmass}} = \frac{1}{2}\overline{n^c_L} M^{\text{D+M}} n_L \tag{3.6}$$

with a left-handed vector containing the neutrino spinors and a mass matrix:

$$n_L = \begin{pmatrix} \nu_L \\ \nu^c_R \end{pmatrix} \quad , \quad \overline{n^c_L} = \begin{pmatrix} \overline{\nu^c_L} & \overline{\nu_R} \end{pmatrix} \tag{3.7}$$

$$M^{\text{D+M}} = \begin{pmatrix} m_L & m_D \\ m_D & m_R \end{pmatrix} \tag{3.8}$$

The absolute mass eigenvalues of the mass matrix are as follows.

$$m_{1,2} = \frac{1}{2}\left|\left(m_L + m_R \pm \sqrt{(m_L - m_R)^2 + 4m_D^2}\right)\right| \tag{3.9}$$

Remember that the left-handed neutrino ν_L is part of a $SU(2)_L$ doublet. Hence, it can have no Majorana mass term, because $\overline{\nu^c_L}\nu_L$ is not gauge invariant [24]. This means that $m_L = 0$. On the other hand, the right-handed neutrino is not affected, as it's a $SU(2)$ singlet and not a doublet. Furthermore, one should notice that the right-handed Majorana mass term violates lepton number by two units. As such a violation has not been observed yet, one can assume with good reason that lepton number is violated at a scale much larger than the electroweak scale [20]. Therefore, $m_R \gg m_D$ if the Dirac mass term is generated by the Higgs mechanism [20].

With all these considerations, one obtains two fundamental mass eigenvalues.

$$m_1 \approx \frac{m_D^2}{m_R} \ll m_D \tag{3.10}$$

$$m_2 \approx m_R \gg m_D \tag{3.11}$$

This is the origin of the expression "seesaw mechanism", because there is one very light particle with mass m_1 (the experimentally observed neutrino) and one very heavy particle with mass m_2 (the "sterile", not yet experimentally confirmed neutrino).
We can now estimate the mass scale of the neutrino if we put in the experimentally observed values, i.e. $m_D \simeq m_{\text{top}}$ and m_1 as the upper limit of light neutrino masses. As a result, one finds

$$m_R \simeq \frac{m_D^2}{m_1} \simeq 10^{15}\,\text{GeV} \tag{3.12}$$

which is similar to the GUT (Grand Unified Theory) scale [20]. This is far out of reach of the world's largest accelerator, the LHC at CERN. As such, it makes sense that the sterile neutrino, if it exists, hasn't been observed yet. However, neutrinoless double beta decay can study the

actual nature of neutrinos (Majorana or Dirac), supporting or rejecting the seesaw approach.

3.4. Measurement of neutrino masses

There are three different main approaches that are being pursued in order to measure neutrino masses [8]: Cosmology, Kurie-plot experiments and neutrinoless double beta decay experiments. They all probe different values connected to neutrino masses [8]:

$$\text{Cosmological:} \quad \Sigma = \sum m_i \tag{3.13}$$

$$\text{Kurie-plot:} \quad m_\beta = \sqrt{\sum |U_{ei}|^2 m_i^2} \tag{3.14}$$

$$0\nu\beta\beta: \quad |m_{ee}| = \left|\sum U_{ei}^2 m_i\right| \tag{3.15}$$

Cosmology probes the sum of all neutrino masses with a current (2015) mass limit of 0.7 eV. However, it is based on the input of cosmological models and it includes difficult systematics [8]. On the other hand, Kurie-plot experiments like KATRIN [25], that measure the electron spectrum of single beta decay, are practically model-independent [8]. These kind of experiments probe the incoherent neutrino sum m_β and the best mass limit up to 2015 is 2.3 eV [8]. Unfortunately, it is very unlikely that masses below 0.1 eV can be probed with this experimental approach, even in the far future [8].
As with the other two approaches, neutrinoless double beta decay has its advantages and disadvantages too, which we will see in the next chapter.

3.5. Double beta decay

Double beta decay ($2\nu\beta\beta$) is a rare second-order weak process, where two neutrons are simultaneously transformed into protons inside of an atomic nucleus. Hence, the nucleus with atomic number Z undergoes a transition into its isobar with an atomic number $Z+2$ [21]:

$$(A, Z) \rightarrow (A, Z+2) + 2e^- + 2\bar{\nu}_e \qquad (2\nu\beta\beta) \tag{3.16}$$

In principal, this process can happen as long as the isobar with atomic number $Z+2$ is lighter than the initial nucleus with atomic number Z. Practically though, double beta decay can only be observed if single beta decay is forbidden energetically, because of the very small branching ratio of double beta decay compared to single beta decay.

Possible nuclear transitions can be estimated with the Weizsäcker mass formula [21]:

$$m(A, Z) \propto \alpha Z + \beta Z + \delta_P(A, Z) + \text{constant} \tag{3.17}$$

where Z is the atomic number, A the number of nucleons in the atom, δ_P the pairing term and α, β arbitrary coefficients. The pairing energy is dependent on the multiplicity of the number of neutrons N and the number of protons Z:

$$\delta_P(A, Z) = \begin{cases} a_P A^{-\frac{1}{2}} & Z, N \text{ even } \rightarrow \text{even-even} \rightarrow \text{A even} \\ 0 & \text{even-odd, odd-even} \rightarrow \text{A odd} \\ -a_P A^{-\frac{1}{2}} & Z, N \text{ odd } \rightarrow \text{odd-odd} \rightarrow \text{A even} \end{cases} \tag{3.18}$$

where the constant a_P has to be measured experimentally.

For odd A we get a single parabola, whereas we get two parabolas for even A, cf. figure 3.2.

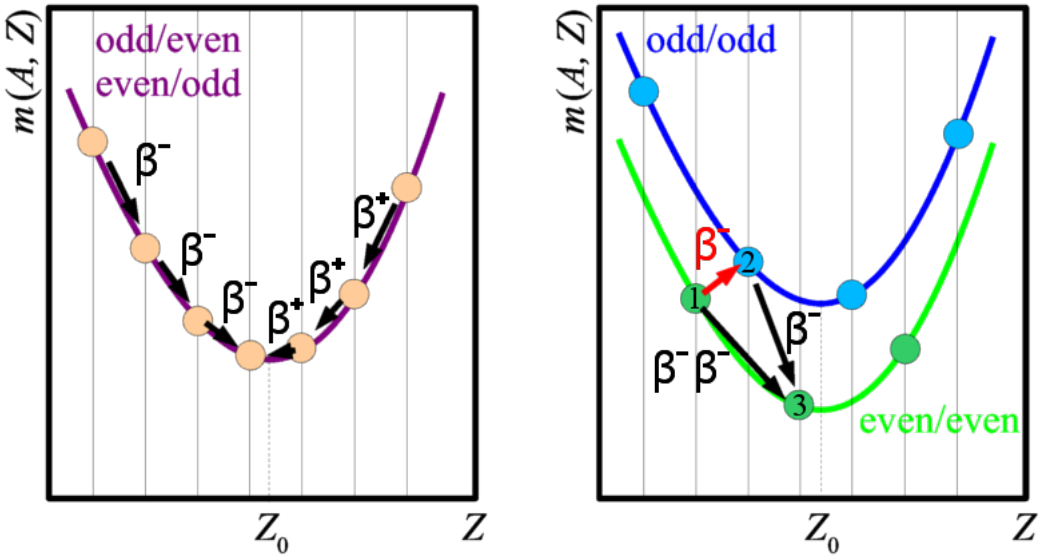

Figure 3.2.: Nuclear mass as a function of Atomic Number Z for odd A (left) and even A (right). In the latter case, single beta decay is kinematically forbidden for even/even nuclei. [26]

Thus, even-even nuclei are lighter than odd-odd nuclei such that single beta decay is forbidden kinematically. Hence, candidates for $0\nu\beta\beta$ must be even-even nuclei.
Although double beta decay is a rare process, it has already been observed in some nuclei with lifetimes above 10^{19} years [27].

4. Neutrinoless double beta decay

Neutrinoless double beta decay is similar to classical beta decay, with the exception that the outgoing neutrinos are missing:

$$(A, Z) \rightarrow (A, Z + 2) + 2e^- \qquad (0\nu\beta\beta) \tag{4.1}$$

This process violates lepton number by two units ($\Delta L = 2$), supporting the idea that leptons could have played a major role in the matter-antimatter asymmetry of the universe (Leptogenesis) [28]. Furthermore, it can be shown that the observation of neutrinoless double beta decay induces the Majorana nature of neutrinos via the black box theorem [8], although there is some discussion about the details [28].
The Majorana nature of neutrinos would reduce the number of distinguishable light neutrinos in one family from four to two ($\nu = \nu^c$).

The general concept of Majorana particles is shown in figure 4.1.

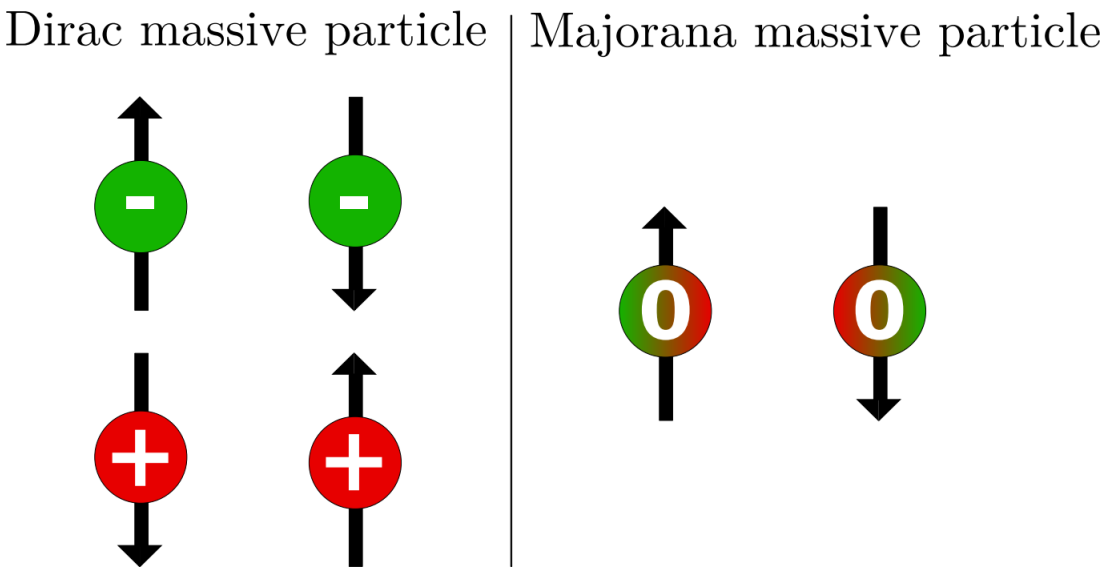

Figure 4.1.: Dirac and Majorana particles in their rest frames. The arrows show the two possible spin directions. (Left) In the Dirac case, matter and antimatter is separated by charge (- matter, + antimatter). For each of them two spin possibilities exist, resulting in four distinguishable particles. (Right) In the Majorana scenario, no $U(1)$ charge exists (0), such that only two different particle states emerge: particles and antiparticles are the same. [28]

Neutrinoless double beta decay can be realized through various theories.
In fact, its total amplitude may be caused by multiple processes in nature. However, the simplest and most standard mechanism is the light Majorana neutrino exchange, which will be presented now based on [23].

4.1. The light Majorana neutrino exchange

In this case, the parent nucleus emits two correlated virtual W^- bosons caused by neutron to proton decays. Subsequently, the W^- bosons exchange a virtual light Majorana neutrino, inducing the production of two outgoing electrons.

A Feynman diagram of this process can be seen in figure 4.2.

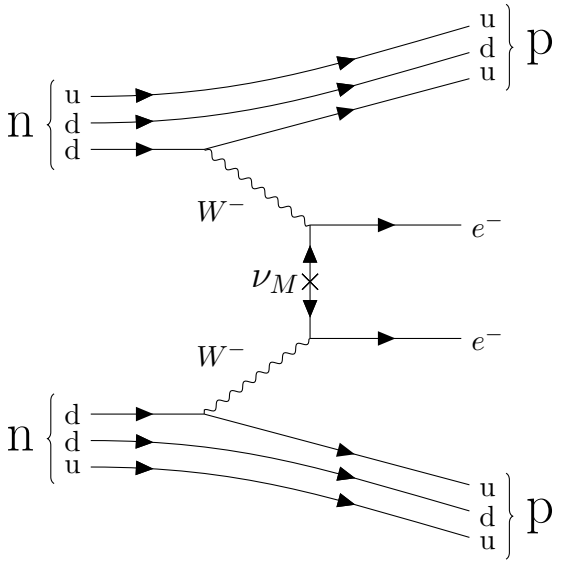

Figure 4.2.: Feynman diagram of neutrinoless double beta decay.

It is vital, that the neutrino is massive in order to get a non-zero amplitude.
This can be understood by starting with one W^- boson, that emits the neutrino and an electron. The neutrino has an almost positive helicity, as it is produced via the weak interaction as a right-handed particle $\bar{\nu}_R$. However, because of the massive character of the Majorana neutrino, it still has a small negative helicity component of the order $\mathcal{O}(m/e)$. Only this small, negative helicity part is absorbed at the other W^- vertex by the electroweak current [23].
Consequently, it can already be seen that this mechanism is strongly suppressed. Additionally, the neutrino has to be its own antiparticle, since it is emitted as a right-handed antineutrino $\bar{\nu}_R$ at the first vertex, but absorbed as a left-handed neutrino ν_L at the second vertex.

4.2. 0νββ half life

In the case of light Majorana exchange, the half-life of 0νββ can be calculated as follows [2][20]:

$$(T^{0\nu}_{1/2})^{-1} = \Gamma^{0\nu} = |m_{\beta\beta}|^2 \left| M^{0\nu} \right|^2 G^{0\nu}(Q_{\beta\beta}, Z) \tag{4.2}$$

Here, $G^{0\nu}$ is a phase space factor that can be calculated with aid of the atomic number Z and the total released energy by the neutrinoless double beta decay reaction, $Q_{\beta\beta}$.
Furthermore, $m_{\beta\beta}$ is the so called effective Majorana mass of the electron neutrino:

$$m_{\beta\beta} = \sum_i U^2_{ei} m_i \tag{4.3}$$

Thus, the measurement of the half-life $T^{0\nu}_{1/2}$ can be used to get clues about the PMNS matrix elements and the neutrino mass eigenstates. Likewise, it is also possible to express the sensitivity and hence the half-life limit on neutrinoless double beta decay of an experiment in terms of the effective Majorana neutrino mass.
The last variable in the 0νββ half-life formula is the nuclear matrix element (NME), which is unfortunately difficult to calculate precisely [28]. There are various models for NME calculations, but unfortunately they differ by a substantial amount.

The calculated nuclear matrix elements for various isotopes with different theoretical models are shown in figure 4.3.

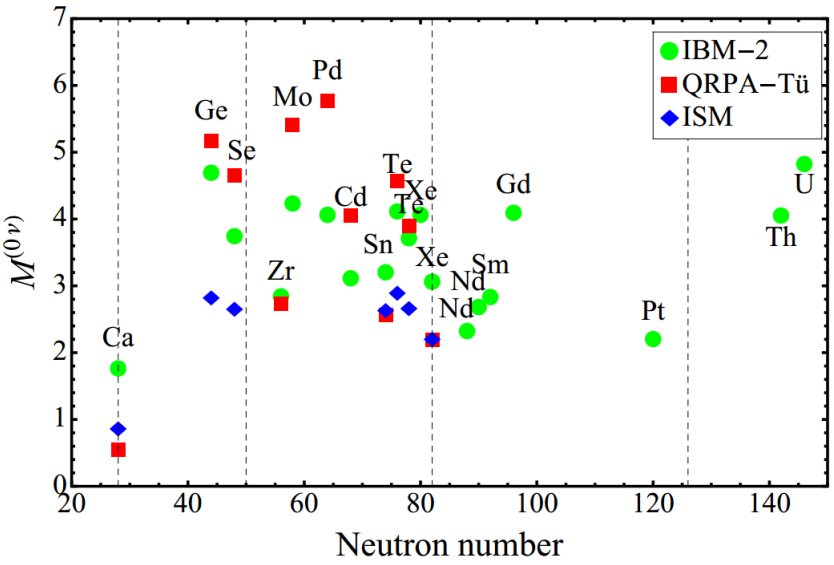

Figure 4.3.: Calculations for the nuclear matrix elements based on three different theoretical models. The agreement of these models varies among multiple nuclei. [29]

4.3. Effective Majorana mass predictions

Using the observed oscillation parameters, it is possible to give limits on the effective Majorana mass $m_{\beta\beta}$, dependent on the mass of the lightest neutrino, m_{lightest} [28].
However, in the case of Majorana neutrinos, there are two additional phases in the PMNS matrix that cannot be probed by oscillation experiments [28].
As a result, the allowed range of $m_{\beta\beta}$ values is rather broad, cf. figure 4.4.
Likewise, measured half life limits $T^{0\nu}_{1/2}$ of experiments can be converted to Majorana masses $m_{\beta\beta}$ using equation 4.2. Unfortunately, this approach is limited by uncertainties in the NME calculations, especially regarding the specific value of the axial coupling constant g_A in the nuclear medium (due to the nuclear quenching factor, cf. [29] for further details).
Based on the predictions for the effective Majorana mass, it can be seen that until now, only the degenerate region has been probed by experiments. Assuming $g_A = g_{\text{nucleon}}$, near future experiments like nEXO [19] intend to probe the the inverted hierarchy regime for the first time.

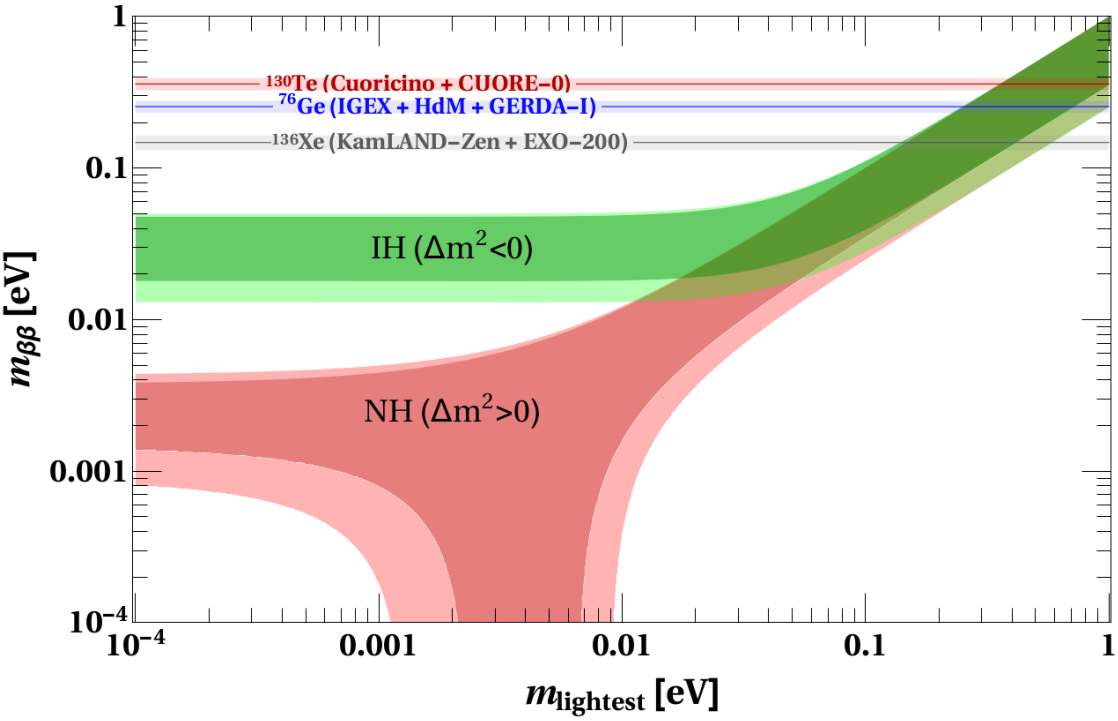

Figure 4.4.: Predictions for the effective Majorana mass based on oscillation observations in the SM three neutrino scenario. The results for the inverted hierarchy scenario are shown in green, whereas the normal hierarchy values are indicated in red. Shaded areas correspond to 3σ regions caused by the uncertainty of oscillation parameters. For the normal hierarchy, the effective Majorana mass can vanish. The horizontal bars indicate the combined lower limits of 0νββ experiments for different nuclei with the assumption $g_A = g_{\text{nucleon}}$. Shaded regions around the bars indicate the uncertainties of the NME calculations and the phase space factor $G^{0\nu}$. However, it should be kept in mind that the absolute value of the lower limits depends largely on the assumed g_A. [28]

5. Experimental challenges in detecting 0νββ

In order to observe neutrinoless double beta decay experimentally, one needs to be able to distinguish between 2νββ events and 0νββ events. For this purpose, the total energy spectrum of the two outgoing electrons, emitted by the double beta decay, can be used.
In the 2νββ case, the sum of the kinetic energy of the two electrons forms a continuous spectrum, because the neutrinos also carry away a part of the released energy. In the case of 0νββ however, there are no neutrinos that can carry away kinetic energy. Keeping in mind that the recoil of the daughter nucleus is small enough to be negligible [30], the two emitted electrons must carry all of the kinetic energy. Thus, the spectrum of 0νββ should consist of a single peak at the Q-value of the decay, making the signature very clear. In reality however, the 0νββ peak is continuous as well, because of a limited energy resolution. As a result, the tail of the 2νββ spectrum can contribute significantly to the event rate in the region of interest around the Q-value of the transition. Therefore, it can already be seen that a good energy resolution is crucial for 0νββ experiments.

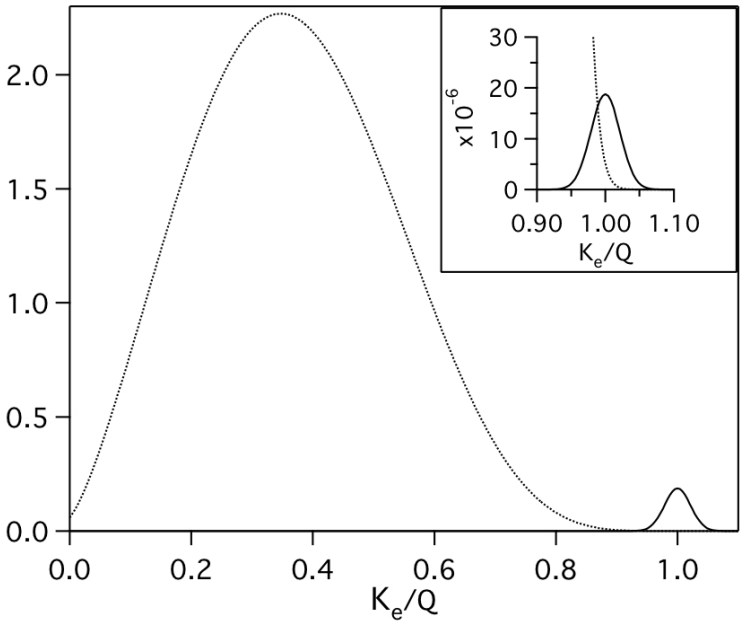

Figure 5.1.: Spectrum of the sum of the electrons' kinetic energies, normalized to the Q-value of the transition. The scale of the y-axis that shows the amount of events is arbitrary. In the top right it can be seen that the tail of the 2νββ spectrum can also contribute significantly to the background in the Q-value regime. [31]

Additionally, basically every background process that takes place around the Q-value of the chosen isotope, can mask the 0νββ signal as well. Hence, sufficient background reduction is essential for any neutrinoless double beta decay experiment.

5.1. Ingredients for the ideal 0νββ experiment

For the ideal neutrinoless double beta decay experiment, a multitude of criteria has to be met. In example, the perfect isotope should unite the following properties:

- **High Q-value ($Q_{\beta\beta}$).** This influences the phase space factor $G^{0\nu}$ and, even more important, the ease of background suppression [32].
- **High Isotopic abundance and ease of enrichment** for large isotope masses. Except ^{130}Te, all of the candidate isotopes have a natural abundance of less than 10% [28]. However,

in order to probe the inverted hierarchy, at least 100 kg of isotope mass are needed [32]. Thus, enrichment is crucial for increasing the sensitivity on 0νββ half life, and even more for the normal hierarchy regime.

- **Slow 2νββ mode**, as energy resolution is limited in practice. Thus, a higher 2νββ half-life of the isotope results in less backgrounds events from 2νββ in the region of interest around the Q-value.

Unfortunately, a perfect isotope, fulfilling every need, does not exist. However, there are nine 0νββ candidate isotopes consisting of ^{48}Ca, ^{76}Ge, ^{82}Se, ^{96}Zr, ^{100}Mo, ^{116}Cd, ^{130}Te, ^{136}Xe and ^{150}Nd [32]. Each of them has their own advantages and disadvantages, such that experimentalists have to choose the most suitable one for their specific experiment.

Besides that, other important experimental properties have to be met, in example:

- **Low background condition**. This requires underground laboratories that shield sufficiently against cosmic rays [27]. Other than that, radiopure materials and active/or passive shielding are required as well [32].
- **Good energy resolution**. This is required to identify the sharp 0νββ peak over an almost flat background [28]. Additionally, it prevents the tail of the continuous 2νββ spectrum from spreading too much into the region of interest around the Q-value.

5.2. Experimental sensitivity

The sensitivity of a neutrinoless double beta decay experiment on the effective neutrino mass $m_{\beta\beta}$ depends fundamentally on the fact if background does or does not exist. The background-free experiment is achieved when the expected number of background events in the region of interest and for the whole lifetime of the detector is less than one [28].
For these two cases, the proportionality to the mass sensitivity is as follows [21][27]:

$$\langle m_{\beta\beta}\rangle \propto \left(\frac{W}{fx\epsilon G^{0\nu}|M^{0\nu}|^2}\right)^{\frac{1}{2}} \left(\frac{b\Delta E}{MT}\right)^{\frac{1}{4}} \qquad \textbf{background-limited} \tag{5.1}$$

$$\langle m_{\beta\beta}\rangle \propto \left(\frac{W}{fx\epsilon G^{0\nu}|M^{0\nu}|^2}\right)^{\frac{1}{2}} \left(\frac{1}{MT}\right)^{\frac{1}{2}} \qquad \textbf{background-free} \tag{5.2}$$

Here, W is the weight of the used source material, f is the abundance of the isotope, x is the proportion of double beta decay candidate atoms in the material, ϵ is the detector efficiency, b is the number of background events per kg $\cdot$ year $\cdot$ keV, ΔE is the energy window for the 0νββ search, M is the mass of the isotope and T is the lifetime of the experiment.
Therefore, any background is a major limitation, as the sensitivity only improves with a factor of $(MT)^{-1/4}$ compared to the background-free case with $(MT)^{-1/2}$.

5.3. General Backgrounds

As we have seen in the last section, even the mere existence of background in the region of interest limits the sensitivity of neutrinoless double beta decay experiments dramatically. Hence, background reduction is a task that every experimental group has to tackle.
In scintillating crystal experiments, like CANDLES, photomultipliers are used to detect the 0νββ signal. Thus, every highly energetic background event that can eventually produce detectable

light in the region of interest (in principle even neutrinos) has to be considered. This includes radioactive transitions with a higher Q-value, because the spectrum of β and γ rays can be continuous [27].
The main initial background consists of α, β or γ rays. α and β rays are easy to shield and as such they are only problematic inside or on the surface of the detector. γ rays however can penetrate matter easily, so they have to be shielded by a sufficiently thick material, e.g. lead. In the next part of this chapter, some possible backgrounds will be presented. One of them is background caused by neutrons, which is the major subject of this thesis.

2νββ events

2νββ events from the tail of the energy spectrum form an inevitable background for every 0νββ experiment. In general, the 2νββ half-life of the used isotopes is very high (e.g. 10^{21} y for ^{136}Xe [32]), but compared to the expected half-life of 0νββ it is not.
It can be shown that the ratio of 0νββ to 2νββ counts is as follows [33]:

$$R_{0\nu/2\nu} = \frac{m_e}{7Q\delta^6} \frac{T_{1/2}^{2\nu\beta\beta}}{T_{1/2}^{0\nu\beta\beta}} \tag{5.3}$$

with $\delta = \Delta E_{\mathrm{FWHM}}/Q$ as the fractional energy resolution at Q. As a result of this strong dependence on ΔE_{FWHM}, a high energy resolution is necessary to suppress 2νββ background.

Natural radiation in the U, Th chain

Natural radioactive elements play a major part in the expected background, because they are present in all materials as contaminations [2]. The half-lives of the decay chains are of the order of the age of the universe [23], but compared to the 0νββ half-life they are short-lived.
Two common decay chains are the U and Th series with ^{208}TI and ^{214}Bi as the most important daughter nuclei. ^{208}TI provides the end point of natural "single pulse" γ ray emissions with 2.6 MeV, which is higher than the Q-value of almost all 0νββ candidate isotopes [27]. Other events can even reach energies above 4 MeV , e.g. through Bi-Po serial decays or $\beta + \gamma$ events caused by ^{208}TI [21]. Hence, radiopure detector materials are advised and analytical methods are necessary to suppress internal background.

Cosmic rays

Cosmic rays and their induced reactions can be a significant contribution to the background. They can produce background events through electromagnetic or hadronic showers. For the most part, this can be solved by going underground. Then, the only surviving radiation consists of muons and neutrinos. Muon interactions can produce highly energetic γ rays, neutrons or electromagnetic showers [2]. On the other side, neutrinos are generally not considered to be a significant background for current experiments, because of their small cross section [2]. In the Kamioka Observatory, where the CANDLES detector is located, the muon flux is reduced by about 1/200.000 [21]. However, the event rate of this flux is still a lot larger than the rate of 0νββ decays with an expected half-life of more than 10^{26} years [21]. As a consequence, most experiments use a veto layer to eliminate events produced by the muon itself or by secondary prompt activities [2]. Nevertheless, secondary high energy neutrons may still penetrate the shield from the outside of the detector. This can be a major source of background, as we will see in the next paragraph.

Neutrons

Neutron induced reactions like (n, γ) reactions can constitute a significant amount of the expected experimental background signal. The initial neutrons are produced by fission, (α, n) reactions and muon reactions in the rock [2]. Fission and (α, n) neutrons have energies up to 10 MeV [2]. On the other hand side, neutrons produced by muon interactions can have very high energies above 1 GeV [2], such that they may penetrate the shielding. On top of that, neutrons can produce external as well as internal background. One of the possible external backgrounds is neutron capture in the rock through (n,γ) reactions. The resulting γ rays can be highly energetic, e.g. 7.6 MeV in iron [21], exceeding the Q-value of all 0νββ isotopes. As a consequence, the shielding needs to handle primary neutrons as well as secondary γ rays. Unfortunately, high density materials used for γ ray shielding like lead are ineffective in neutron shielding. Thus, the shielding needs several layers with different materials to block various kinds of radiation. In CANDLES, it has been found that neutrons are currently the major cause of background events in the region of interest.

5.4. Experimental overview

As demonstrated in this chapter, there is no ideal 0νββ isotope and thus also no ideal experiment. Hence, there are a lot of different experimental approaches that can be pursued for 0νββ search. One major experimental choice is, if the source also acts as the detector (calorimeter) or if the detector is separate from the (external) source [32]. Besides that, some experiments favor a higher energy resolution over an effective tracking capability and vice versa [32]. A selection of current experiments will be presented in the next paragraphs.

GERDA [21][32]

GERDA (GERmanium Detector Array) is a calorimetric 0νββ experiment that uses ^{76}Ge as an isotope. It is located in the underground laboratories of the LNGS (Laboratori Nazionali del Gran Sasso) in Italy. The germanium is contained in Ge diodes that also act as the detector (detector = source). The usage of semiconductor Ge diodes leads to a high energy resolution (0.25% FWHM). Furthermore, the source is immersed in liquid argon which is used for cooling and as an active shield. The current lower limit for neutrinoless double beta decay in ^{76}Ge has been derived by GERDA (Phase 1) as follows:

$$T^{0\nu}_{1/2}(^{76}\mathrm{Ge}) > 3.0 \times 10^{25}\mathrm{yr} \quad (90\%\ \mathrm{C.L.})$$

The second phase of GERDA, which is currently running, combines more target material and a reduced background, in order to improve the sensitivity.

CUORE [32]

CUORE (Cryogenic Underground Observatory for Rare Event), which is currently still under construction, uses the same calorimetric approach as GERDA. However, the detection method is very different: CUORE consists of TeO_2 bolometers that measure the thermal signature of the electrons that are emitted in double beta decay. It features the same high energy resolution as GERDA (0.25 % FWHM), while also being located in the Gran Sasso underground laboratory. The expected sensitivity after 5 years of data taking is the following:

$$T^{0\nu}_{1/2}(\mathrm{TeO_2}) > 9.7 \times 10^{25}\mathrm{yr} \quad (90\%\ \mathrm{C.L.})$$

EXO [23][32]

EXO (Enriched Xenon Observatory) is a calorimetric experiment with the ability to measure the topology of events. EXO consists of a time projection chamber (TPC) with 200 kg of enriched liquid xenon. Events can be measured through two separate techniques. As xenon is a scintillator, one method is to measure the scintillation light produced by the decay particles. The other one is to collect the ionization electrons in the detector. By combining both techniques, the TPC can measure the 3D coordinates and the ionization deposits for each event. This allows for the discrimination of single-site (possible signal) and multi-site (background) events. Unfortunately, the Xe-TPC detection technique also leads to a worse energy resolution compared to GERDA or CUORE: 3.9% at FWHM in the region of interest around Q. The best half-life limit obtained by EXO till now is as follows:

$$T_{1/2}^{0\nu}(^{136}\mathrm{Xe}) > 1.6 \times 10^{25}\mathrm{yr} \quad (90\%\ \mathrm{C.L.})$$

ELEGANT VI and CANDLES [21]

ELEGANT VI and its successor CANDLES use Calcium 48 as $0\nu\beta\beta$ isotope. In ELEGANT VI, the Calcium is contained in 23 scintillating $CaF_2(Eu)$ crystals with sizes of $4.5\,\mathrm{cm} \times 4.5\,\mathrm{cm} \times 4.5\,\mathrm{cm}$. ELEGANT VI achieved the background-free measurement with an exposure of $4947\,\mathrm{kg} \cdot \mathrm{d}$, which amounts to about two years of measurement. With this setup, the most sensitive limit for the neutrinoless double beta decay in ^{48}Ca could be derived:

$$T_{1/2}^{0\nu}(^{48}\mathrm{Ca}) > 5.8 \times 10^{22}\mathrm{yr} \quad (90\%\ \mathrm{C.L.})$$

CANDLES aims to improve this limit by employing 40 times the amount of target mass. The details of this project will be discussed in the next chapter.

6. The CANDLES experiment

CANDLES (**CA**lcium fluoride for studies of **N**eutrino and **D**ark matters by **L**ow **E**nergy **S**pectrometer) is a neutrinoless double beta decay experiment that uses ^{48}Ca as isotope.
The advantage of using ^{48}Ca is that it has the highest Q-value among all $0\nu\beta\beta$ candidate isotopes ($Q_{\beta\beta} = 4274\,\text{keV}$ [21]). This simplifies the task of background suppression, as e.g. the endpoint of natural single γ ray radiation is 2.6 MeV from ^{208}Ti decay [21]. In addition, a higher Q-value leads to a better energy resolution in the region of interest, which is needed for the rejection of $2\nu\beta\beta$ events. On the contrary, the main disadvantage of ^{48}Ca is its low abundance (0.187% [34]) and the difficulty of enrichment. Because ^{48}Ca has no gaseous compound, it cannot be enriched by centrifugation. Unfortunately, other techniques for ^{48}Ca enrichment are not exploited industrially yet (only R&D) and thus they are very expensive compared to centrifugation [32]. Nonetheless, enrichment methods by laser excitation or by using resin-treated crown ether are currently being studied in the CANDLES collaboration [21].

6.1. Experimental setup

The CANDLES detector is currently operating at the Kamioka Observatory, next to Hida-city, Gifu Prefecture, Japan. More specifically, it is located inside the abandoned Mozumi mine and thus shielded by about 1000 m [35] of concrete rock (2700 m water equivalent [36]).
The setup of CANDLES consists of a 3 m diameter $\times$ 4 m height stainless steel water tank containing 96 cubic CaF_2(pure) crystals weighting 305 kg in total [21]. The emission wavelength of scintillation photons by CaF_2(pure) crystals is in the UV region and thus beyond the sensitive region of the used photomultipliers [27]. Therefore, each crystal is encased in a wave length shifter (WLS) module with 5 mm thickness that converts scintillating UV photons into visible region photons [21]. One CaF_2(pure) crystal combined with a WLS forms a cubic CaF_2 module with 10 cm edge length [21]. The CaF_2 modules themselves are immersed in a $2\,\text{m}^3$ liquid scintillator (LS) with a decay time constant of a few tens ns. This is different to the decay time of CaF_2(pure) crystals (about 1 µs) [36]. Hence, the LS can be used as a 4π active shield vetoing external background by applying pulse shape discrimination (PSD) [36].
Other than that, the detector is cooled down to about 5 °C, which increases the scintillation light of CaF_2 by about 30%. The LS and the crystal modules are contained in a secondary transparent acryl tank that is placed inside the larger 3 m $\times$ 4 m water tank. The crystals inside the secondary tank are arranged in 6 layers with 16 crystals each, observed by 14 20-inch PMTs and 48 13-inch PMTs [36], cf. figure 6.2.

6.2. Triggering

As demonstrated in the last section, pulse shape discrimination can be used for the differentiation of CaF_2 and LS events. This technique can already be exploited during triggering. The main trigger in CANDLES is made up of a dual gate trigger system (DGT). This system can reject LS events immediately on a hardware level by examining the integrated digital pulses of two "gate" areas, S1 and S2 (cf. figure 6.3) [21].
For each gate, the trigger is issued when the integrated pulse value is above a certain threshold. The timing window for S1 is 128 ns and for S2 it is 168 ns while the time delay between S1 and S2 is 384 ns. Now, one can exploit the different decay time constants of CaF_2 and LS events. Because of the short decay time, LS events only trigger S1 and not S2. CaF_2 events on the other hand side trigger both S1 and S2. Hence, the DAQ system of CANDLES can reject LS events by only recording data with S1 and S2 coincidence with a very high trigger efficiency (cf. [21] for more information).

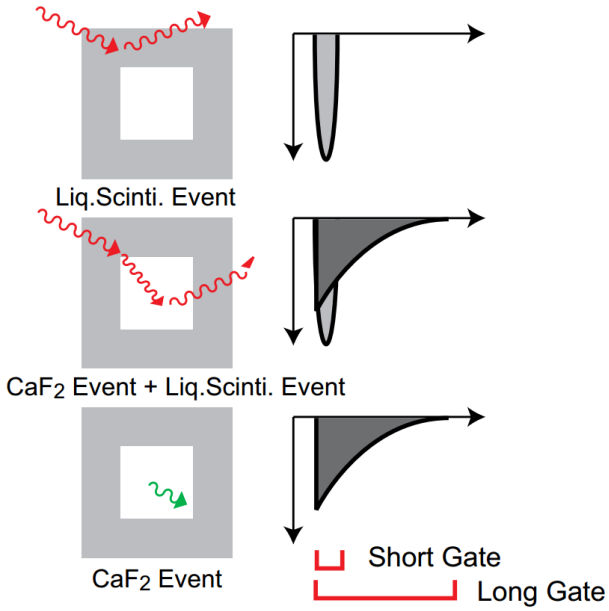

Figure 6.1.: Illustration of the different pulse waveforms of scintillation light. CaF_2 events have a long decay constant (about 1 µs, long gate) while the pulse length of LS events is much shorter (few tens ns, short gate). CaF_2 + LS events can still be rejected by pulse shape discrimination in offline analysis. [27]

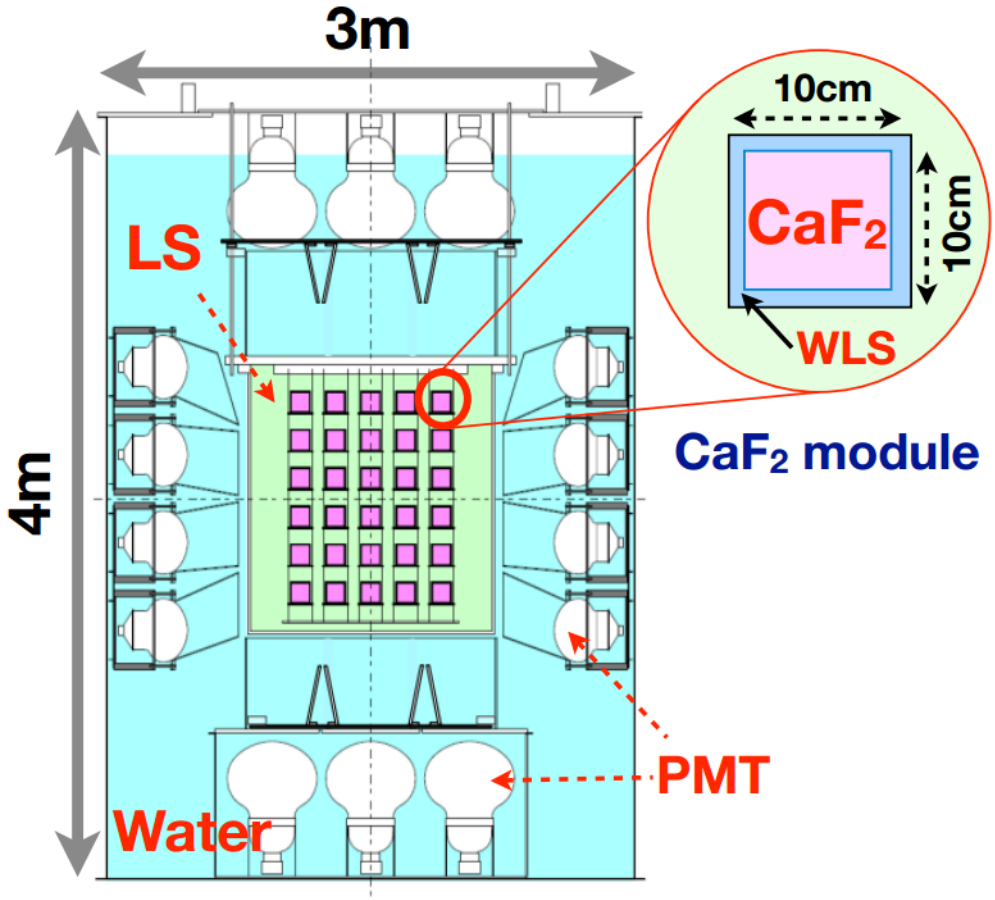

Figure 6.2.: Setup of the CANDLES detector. [21]

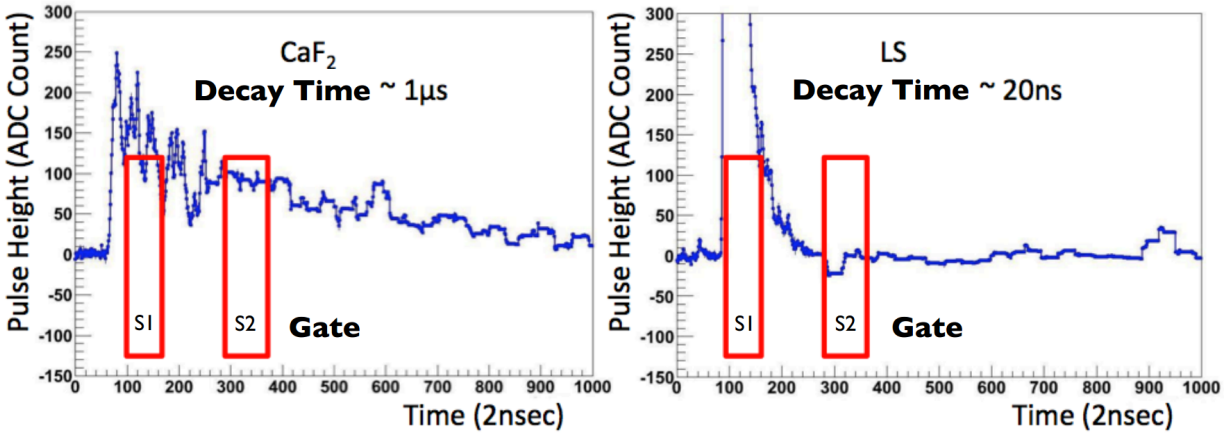

Figure 6.3.: Basic principle of the dual gate trigger system that is used in CANDLES. The red rectangles indicate the time window used for the integration of pulse values for the S1 and S2 gate. On the left hand side, the CaF_2 event has a comparatively long decay constant such that both S1 and S2 are triggered. On the right hand side, the decay constant of the LS event is so short, that only S1 and not S2 is triggered. [21]

6.3. Event reconstruction

Since neutrinoless double beta decay is a very rare process, every event recorded by the detector has to be characterized in detail, in order to reject as much background as possible. This is done in both online (through triggering) and offline analysis.

At first, scintillation light is measured by the 62 PMTs surrounding the CaF_2 crystals. For each PMT, the "raw data" is recorded as a voltage on each bin paired with a time stamp by a 500 MHz Flash ADC (FADC). Data is collected within a 8 µs time window with 256 bins per 2 ns for the first 512 ns and 128 bins per 64 ns for the remaining 8.2 µs. The resulting pulse shape of a recorded event can then be used in offline analysis for background reduction through pulse shape discrimination.

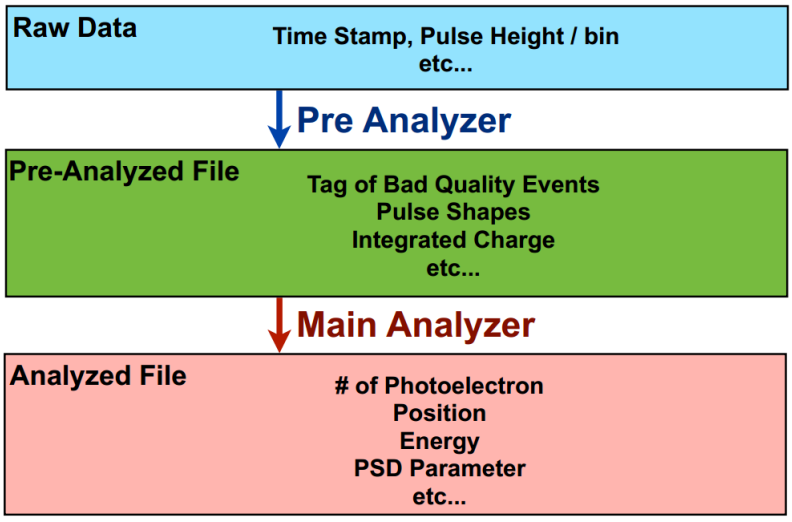

Figure 6.4.: Illustration of the CANDLES Analysis Chain. [21]

Subsequently, the raw data is analyzed by a "Pre Analyzer" algorithm in offline analysis. In the first step, the tool tags bad quality events (e.g. events with saturated PMTs). Afterwards, the integrated charge for 4 µs (beginning with the pulse-starting channel) is calculated for every PMT. The pedestal that is needed for this calculation is gained by non-pulse events taken by a 1 Hz clock trigger. After the Pre Analyzer is finished, a "Pre-Analyzed File" is created and the "Main Analyzer" can be applied on that file. This second tool calculates various "high-level" parameters like Position, Energy and the PSD parameters (to reject e.g. CaF_2+LS events). The position of an event can be reconstructed by analyzing the integrated charge for each PMT while the reconstruction of energy uses the total amount of photoelectrons measured by the PMTs. For the calculation of the PSD parameters, the 62 pulses are summed up after aligning the pulse-starting timing. The resulting "Analyzed File" can now be used for further Physics analysis.

The data itself is divided into "Runs" and "Subruns", e.g. "Run001-001" (Run-Subrun). During a normal "Physics-Run" (used for 0νββ data taking), one Subrun takes about 24 h in the latest Run (Run009). The data that is used for this work consists of Run007, Run008 and Run009.

6.4. Background of CANDLES

Even though the high Q-value of Ca^{48} and the 4π active LS shield strongly suppress the background, there are still three different types of remaining background (besides the inevitable 2νββ). The following overview is based on [36], [37] and [38].

Consecutive Bi → Po decays by impurities within CaF_2 crystals

Although the contamination of the CaF_2 crystals in CANDLES is very low (less than 0.6 mBq kg^{-1} [27]), it is still significant in the context of the search for 0νββ.
These impurities can lead to sequential Bi → Po decays:

$$^{212}\text{Bi} \xrightarrow{Q_\beta=2.25\,\text{MeV}} {}^{212}\text{Po}\ (\text{T}_{1/2} = 0.299\,\mu\text{s}) \xrightarrow{Q_\alpha=8.79\,\text{MeV}} {}^{208}\text{Pb} \qquad (^{232}\text{Th-Chain})$$

Due to optical quenching, the observed energies of α rays are smaller than the Q-value of the decay. The quenching factor in CaF_2 crystals is about 0.3. Thus, single decays of Polonium-212 do not have to be considered as a background. However, ^{212}Po has a half-life of 0.299 µs, shorter than the event window of CANDLES (4 µs). Thus, the sequential decay is identified as one event with a maximum energy of $E_{max} = 4.9$ MeV, larger than the Q-value of ^{48}Ca. Nevertheless, these double pulse events can be rejected by using PSD, reducing the background by two orders of magnitude. The remaining number of events is so small that they can be ignored.

$\beta + \gamma$ decays by ^{208}Tl from the ^{232}Th-Chain

Similar to the Bi → Po sequential decay, ^{208}Tl is also internal background, contained in the crystals through the Th-Chain. With a Q_β-value of 5 MeV, the Tl decay has to be considered as a background.

$$^{212}\text{Bi} \xrightarrow{Q_\beta=2.25\,\text{MeV}} {}^{208}\text{Tl}\ (\text{T}_{1/2} = 3.053\,\text{min}) \xrightarrow{Q_\beta=5.00\,\text{MeV}} {}^{208}\text{Pb} \qquad (^{232}\text{Th-Chain})$$

Part of the background can be rejected with a time coincidence method using PSD, as the half-life of ^{208}Tl is 3 minutes. Unfortunately, accidental coincidence is high, such that the rejection efficiency is only about 60%. The remaining background is about one event per 60 days. The decay scheme for ^{208}Tl is shown in figure 6.5.

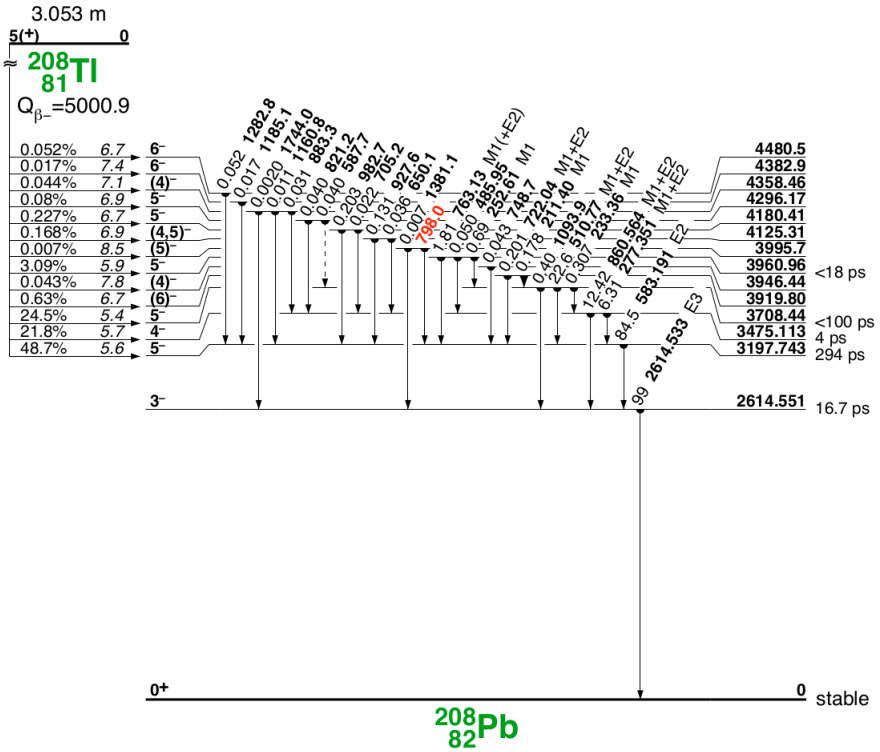

Figure 6.5.: ^{208}Tl decay scheme. $\beta + \gamma$ decays by ^{208}Tl are a major source of background. [39]

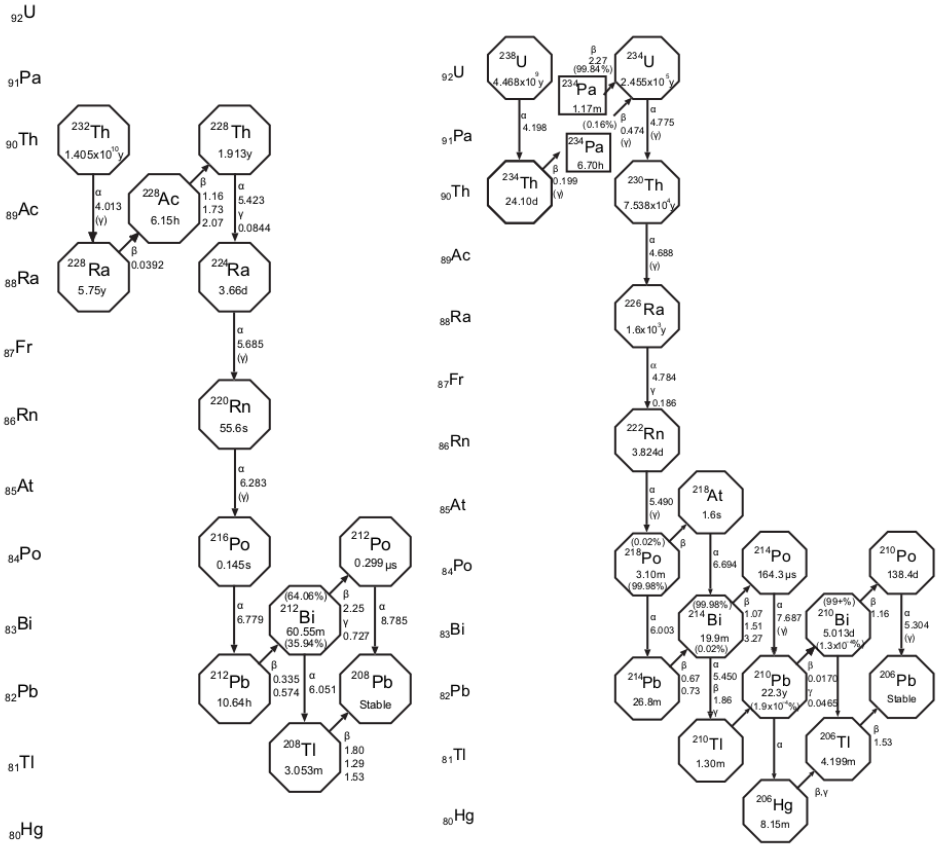

Figure 6.6.: Thorium and Uranium decay chain. [27]

γ-rays by (n, γ) neutron capture reactions

After taking the first data underground with the newly constructed CANDLES detector in 2012, unexpected high energy events ($E > Q_{\beta\beta}$) were observed. It has been found that these events are γ-rays that are caused by neutron capture in the material surrounding the detector.

Neutron capture is nuclear process where thermal neutrons and atomic nuclei interact and then merge to form a heavier nucleus. This nuclear transition can be accompanied by highly energetic γ-ray emissions (n, γ reaction). In CANDLES, there are 2 different major origins of (n,γ) reactions: events caused by neutron capture in the rock surrounding the detector or neutron capture in the stainless steel tank of the detector. In the first case, neutrons are captured by the rock surrounding the experimental apparatus. This mechanism produces high energy γ-rays that can enter the detector easily. In the second case, the neutrons are captured by the the stainless steel tank that contains the detector.

As the resulting γ-ray spectrum depends on the material where the neutrons are captured, there is a difference in the spectrum for the rock compared to that of the tank (cf. figure 6.8 and 6.9). There are two main observed high-energy peaks in the spectrum, one around ≈ 7.6 MeV and the other one around ≈ 9 MeV. Their origin is the Fe and Cr/Ni respectively contained in the rock and the stainless steel tank.

To confirm that the observed high-energy peaks are indeed caused by (n,γ) reactions, additional measurements were made with a radioactive ^{252}Cf neutron source set outside of the tank. The statistics in a 1.5 h ^{252}Cf run is almost equivalent with the statistics of a 1 year physics run. Comparing the energy spectrum of a 3.1 hour ^{252}Cf run with the normal "physics" run (no source), demonstrates that the observed high-energy background is in fact caused by (n,γ) reactions due to neutron capture (cf. figure 6.7).

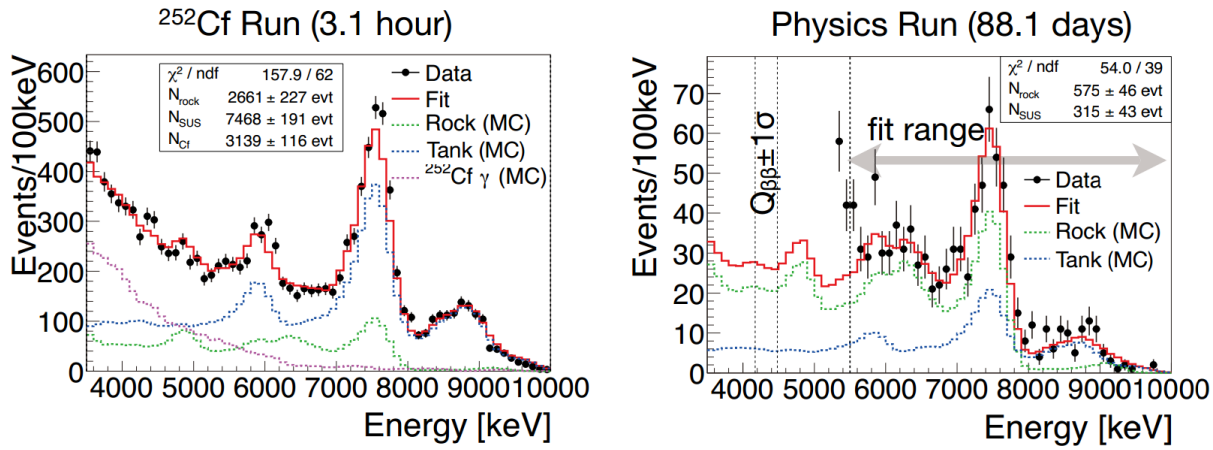

Figure 6.7.: (Left) Energy spectrum taken with a ^{252}Cf neutron source. (Right) Energy spectrum taken in a normal physics run. The observed data is fit based upon a Monte Carlo simulation for each background component. [38]

The amount of background in the $Q_{\beta\beta}$ region caused by the (n,γ) reactions can be estimated by using Monte Carlo simulations. The result is 76 ± 9(stat.) events/year/96crystals. This is three times more than the ^{208}Tl background, making it the largest background in the CANDLES experiment [40]. This circumstance makes the (n,γ) background reduction a first priority.

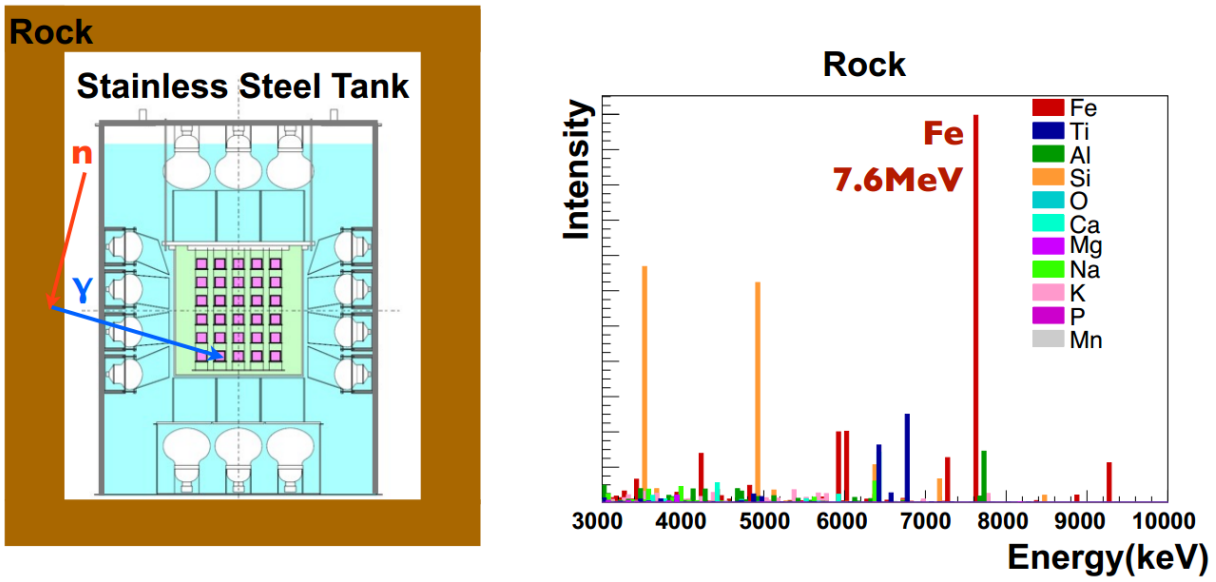

Figure 6.8.: (Left) Illustration of neutron capture in the rock, causing high-energy γ-rays in effect. (Right) Calculated γ-ray spectrum of (n,γ) events in the rock. The ratio for the intensity of each element is dependent on its cross section and also on the abundance in the material due to the chemical composition of the rock. The major emission of rock events is caused by iron with a peak energy of about 7.6 MeV. Furthermore, two lower-energy (< 5 MeV) silicon peaks are close to the Q-value of Calcium-48. [21]

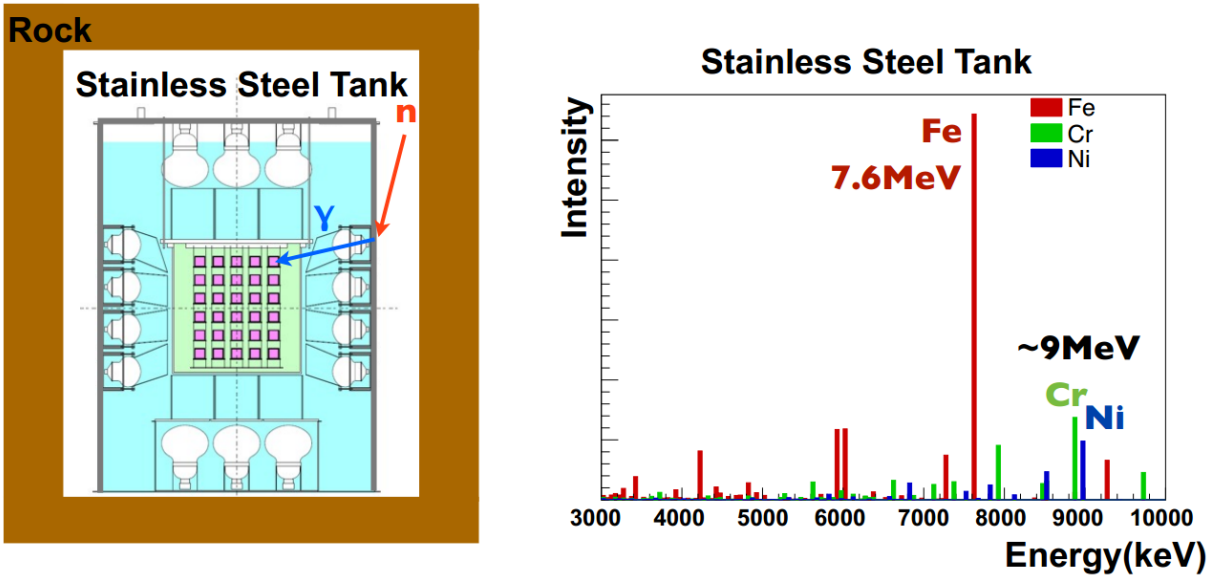

Figure 6.9.: (Left) Illustration of neutron capture in the tank, causing high-energy γ-rays in effect. (Right) Calculated γ-ray spectrum of (n,γ) events in the stainless steel tank. The ratio for the intensity of each element is dependent on its cross section and also on the abundance in the material due to the chemical composition of the tank. The major emission of tank events is caused by the 7.6 MeV iron peak as well as chromium and nickel with peak energies of about 9 MeV. There are no major silicon emissions compared to the rock energy spectrum, because of the chemical composition of the stainless steel tank (Type: "SUS304"). [21]

6.5. Shield construction to lower (n,γ) background

Fortunately, the amount of background caused by neutron capture can be reduced by shielding the detector. Hence, a passive shield has been built around the CANDLES detector, with the construction finished in early 2016. An illustration of the shield design can be seen in figure 6.10.

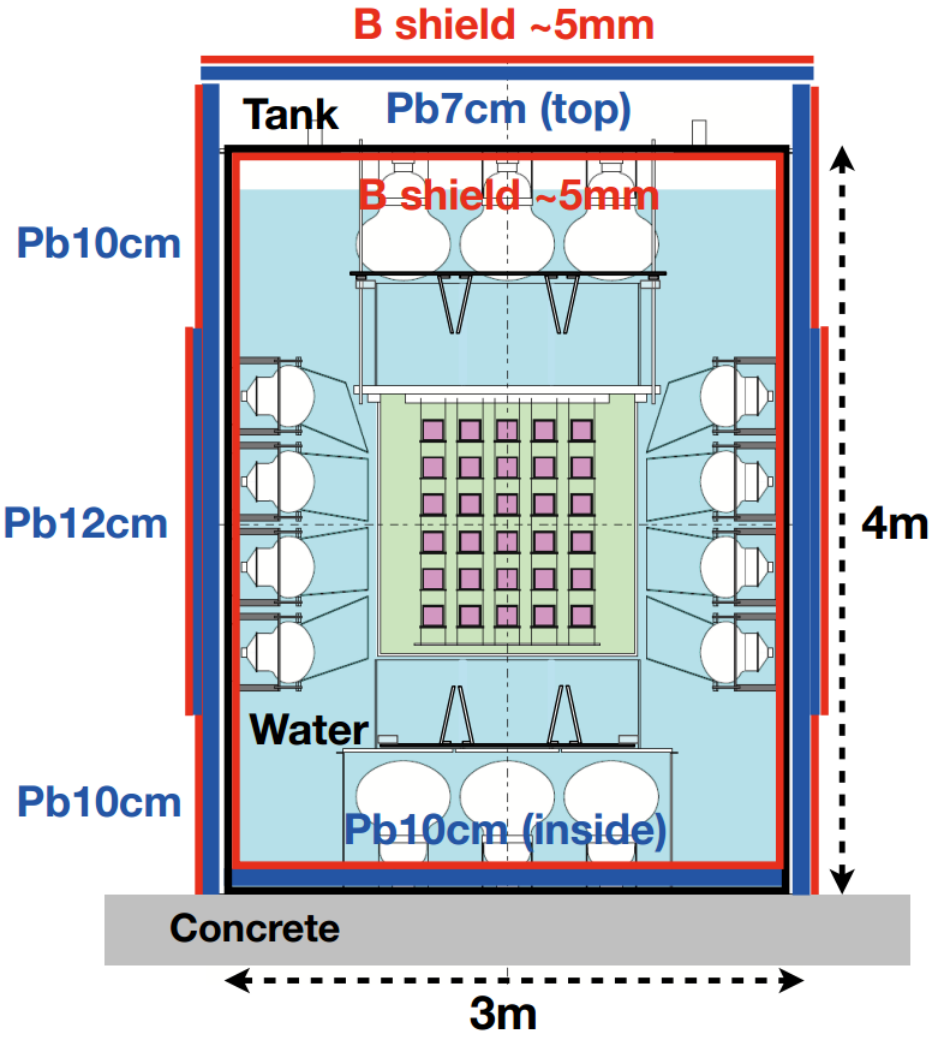

Figure 6.10.: Schematic view of the CANDLES (n,γ) background shield design. The lead is required for rock events, whereas the boron rubber sheet reduces tank events. [38]

The shield consists of two elements, a lead (Pb) shield to attenuate γ-rays and a boron rubber sheet to shield thermal neutrons. The purpose of the Pb shield is to lower the background of (n,γ) rock events. In this case, neutrons are captured in the rock surrounding the detector, accompanied with the subsequent emission of high-energy γ-rays that can enter the detector. Lead with a thickness of 10 cm reduces γ-rays with several MeV to a few hundreds [38]. This is estimated to be enough in order to achieve the final desired background rate [21]. As there are restrictions on the maximum weight on the top of the detector tank, the top lead shield is only 7 cm thick. On the other hand side, the lead around the center of the side of the tank is 12 cm thick, because the passive water shield is thinnest in that area.

The type of shielding required for tank (n,γ) events is different. In this case, thermal neutrons that have already passed the lead shield are captured in the stainless steel tank, causing γ-rays. These neutrons can be shielded by a material with a high neutron capture cross section, whose neutron capture reaction does not produce problematic high-energy γ-rays (e.g. boron ^{10}B).

In CANDLES, a 5 mm thick silicone rubber sheet with 40wt% of boron carbide (B_4C) is used [21]. This sheet is applied to the top of the lead shield and also to the inside of the tank, since non-thermal neutrons passing the detector can be thermalized due to the water inside of the tank.

The desired (n,γ) background rate with shielding is about 1 event/year/96crystals, which is 1/80 of the rate without a shield [38]. The main goal of this thesis is to estimate the effect of the constructed shield on the (n,γ) background and also to analyze the background caused by neutrons in general.

7. Methods

In this chapter, the main analysis methods ("cuts" in various parameters) that are used for the neutron background analysis are discussed. This is necessary, because the goal is to only estimate the effect of the shield for certain types of events. In example, the reduction of LS events due to shielding is not of interest, because they can be rejected by the Dual Gate Trigger anyways. As such, the event selection for the (n,γ) background analysis is similar to the one used in 0$\nu\beta\beta$ search.

7.1. Bad quality events

The first important cut criterion is the rejection of bad quality events.
Examples are e.g. events with saturated PMTs, overshoot PMTs or start channel errors. However, in the search for 0$\nu\beta\beta$, events with saturated signals are still included in the analysis in order to not reject $Q_{\beta\beta}$ region events falsely. In the data, every recorded event has a "DataQuality" vector, that contains the required information to reject those events.

Exemplary pulse shapes can be found in figure 7.1.

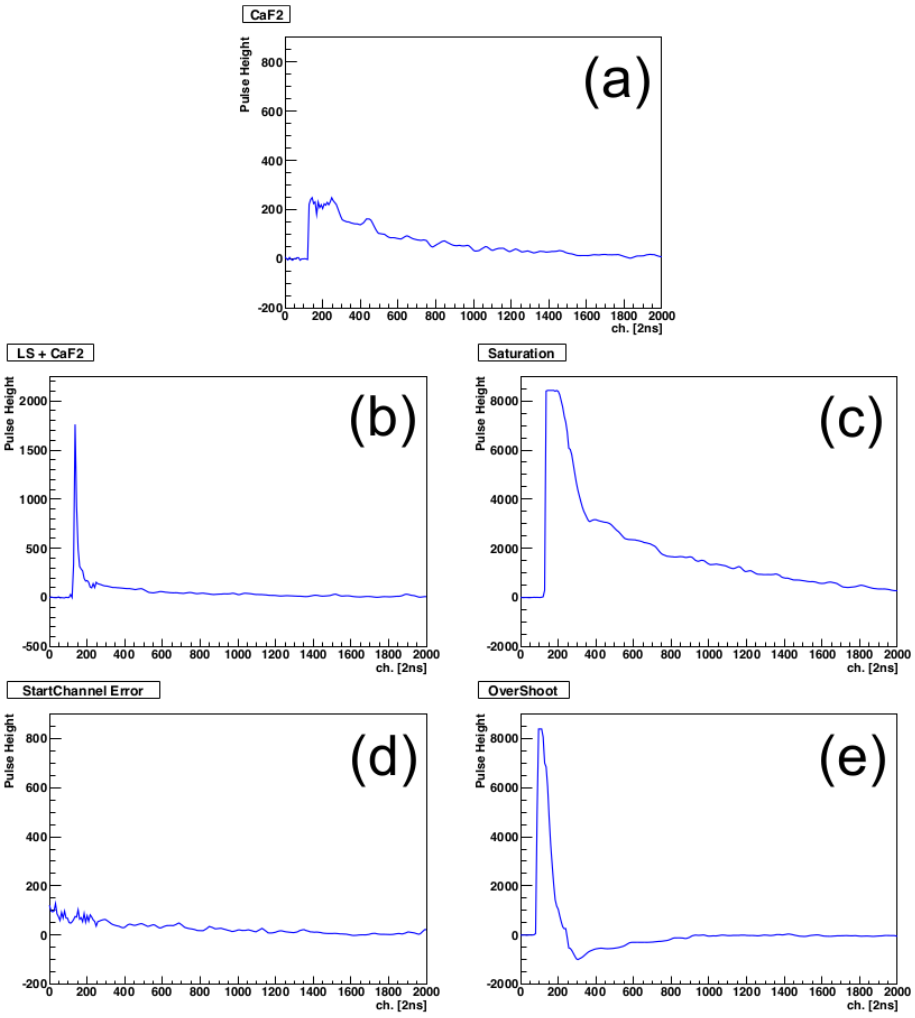

Figure 7.1.: Pulse shapes for different types of events. (a) Normal CaF_2 pulse shape. (b) CaF_2 + LS pulse shape. (c) A saturated signal. (d) A start channel error. (e) An overshoot signal. [21]

7.2. Position reconstruction

In CANDLES, neutrinoless double beta decay can only occur inside of the CaF_2 crystals. Hence, among other reasons, the position is an essential cut criterion. As such, a method to reconstruct the position of events is necessary.
For this purpose, a weighted mean method can be used for every event reconstruction [21]:

$$\vec{r} = \frac{\sum_{n=1}^{62} I_n F_n \overrightarrow{\mathrm{PMT}}_n}{\sum_{n=1}^{62} I_n F_n} \tag{7.1}$$

Here, $\vec{r}$ is the reconstructed position vector (x,y,z) of each event, n is the PMT number, I_n is the integrated pulse charge for each PMT, F_n is a photoelectron number correction factor that is given for each PMT and $\overrightarrow{\mathrm{PMT}}_n$ is the position vector of the n-th PMT.
The result can be seen in figure 7.2.

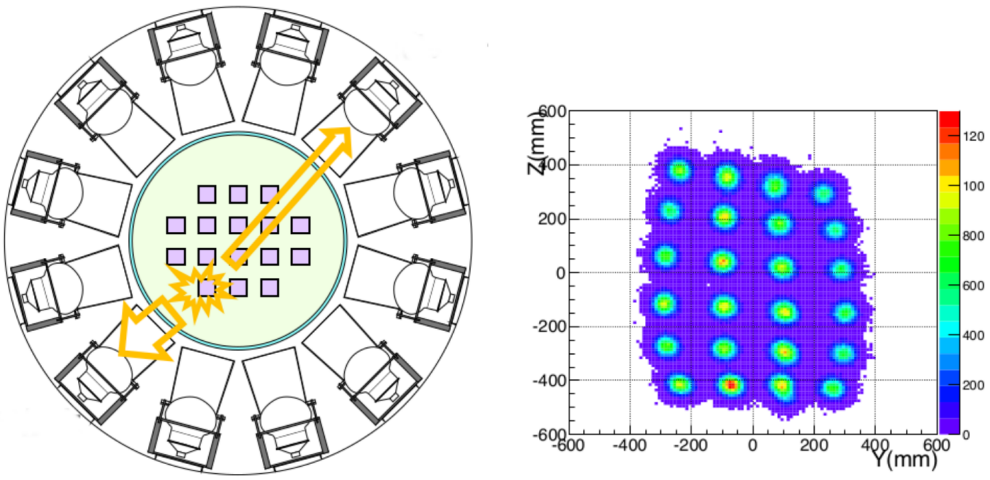

Figure 7.2.: Event position reconstruction in CANDLES. (Left) The vectors of PMTs that are close to the event origin contribute with a higher "weight" $I_n F_n$ in the calculations. As such, the initial position of an event can be reconstructed. (Right) Exemplary distribution of the position reconstruction for the y-z axis. Spots with a high number of events correspond to the CaF_2 crystals. [41]

After reconstruction, the crystals can be identified as spots with a high number of events. Around each of those crystals, a Gaussian distribution is observed. If the event is contained in such a Gaussian distribution, it is checked if the event's position is within 1σ, 1.5σ, 2σ, etc. of the Gaussian function (=crystal). Thus, it is possible to select events that are contained in a certain crystal based on various standard deviations. Still, it has to be kept in mind that this method only reconstructs the weighted mean based on the scintillation light.

7.3. Pulse shape discrimination: separation of α, β and β+LS

As CANDLES is looking for a possible neutrinoless double beta decay signal, the background can be reduced significantly by the identification of the different event types (e.g. LS, α, β, β+LS and γ). Although β and γ events cannot be separated by pulse shape discrimination (PSD), it is still possible to discriminate LS, α, β and β+LS (like $\beta + \gamma$) events from each other. LS events are rejected through the dual gate trigger with a high trigger efficiency, but CaF_2+LS events (e.g. $\beta + \gamma$) with a small energy deposit in the liquid scintillator are still left. The situation can be improved again by exploiting the different pulse shapes of CaF_2 and CaF_2+LS events caused by the different decay constants of the crystals and the LS (cf. figure 6.1). The amount of

difference in the pulse shapes of CaF_2 and CaF_2+LS events depends on the fraction of energy that is deposited in the LS compared to the CaF_2 energy deposit. The same method can be applied to α and β events, because the decay constant of α signals in CaF_2 crystals is a little bit shorter than those of β signals (cf. figure 7.3).

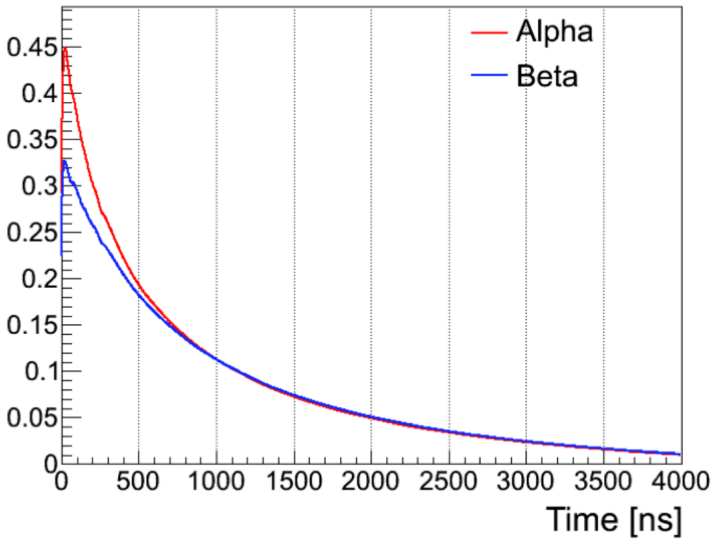

Figure 7.3.: Pulse shapes of α (red) and β (blue) events where the X-axis shows the summed pulse height of the PMTs. The different decay constants lead to a small gap between the pulse shapes of α and β events. The difference is especially large in the first 500 ns. This effect can be exploited in PSD analysis. [21]

The first step in the PSD analysis is to create an averaged reference pulse for each event type (α, β, β+LS) based on about 10.000 events from data [21]. In the next step, each event is fit to the reference pulses, leading to three reduced chi square values (χ^2_α, χ^2_β, $\chi^2_{\beta+\mathrm{LS}}$). These parameters in turn can be used for selecting a certain type of event. In example, imposing a tight upper limit on χ^2_β rejects most α and β+LS events. An illustration of the distributions for χ^2_α and χ^2_β can be found in figure 7.4. The cut efficiencies for this procedure will be discussed in the relevant sections in the next chapters.

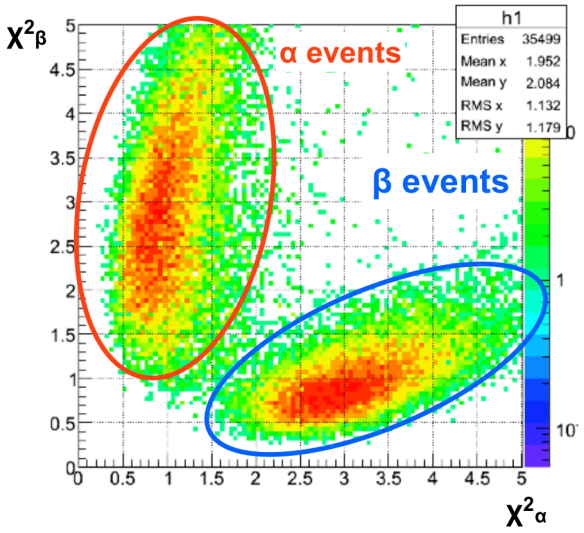

Figure 7.4.: Distributions of χ^2_α and χ^2_β values for exemplary CANDLES data. In this instance, imposing an upper cut limit on χ^2_β, e.g. 1.5, rejects most α events. [21]

8. CANDLES detector performance - Energy scale and event rate stability

A major technical challenge in neutrinoless double beta decay experiments that hasn't been mentioned yet is running the detector over a long period of time, i.e. many years. During this time, the experimental conditions can change significantly, e.g. due to varying temperature or degrading equipment like PMTs. As a consequence, the performance and stability of the CANDLES detector has to be monitored regularly.
In this chapter, we will introduce an analysis that focuses on checking the energy scale and the event rate stability of the CANDLES detector over time based on beta events.

8.1. Introduction and purpose of the analysis

The principal part of this analysis consists of checking the energy scale of the calibrated data with beta signature events that are detected in the crystals. Since the differentiation between β and γ signals with a pulse shape discrimination is not possible in CANDLES, the selected "beta" events can include both β (electrons) as well as γ-ray signals.
For the purpose of this analysis, one can use the natural background spectrum in the region of 1 MeV to 3 MeV that contains two major peaks: ^{40}K and ^{208}Tl.
An exemplary background spectrum for Run008 is shown in figure 8.1.

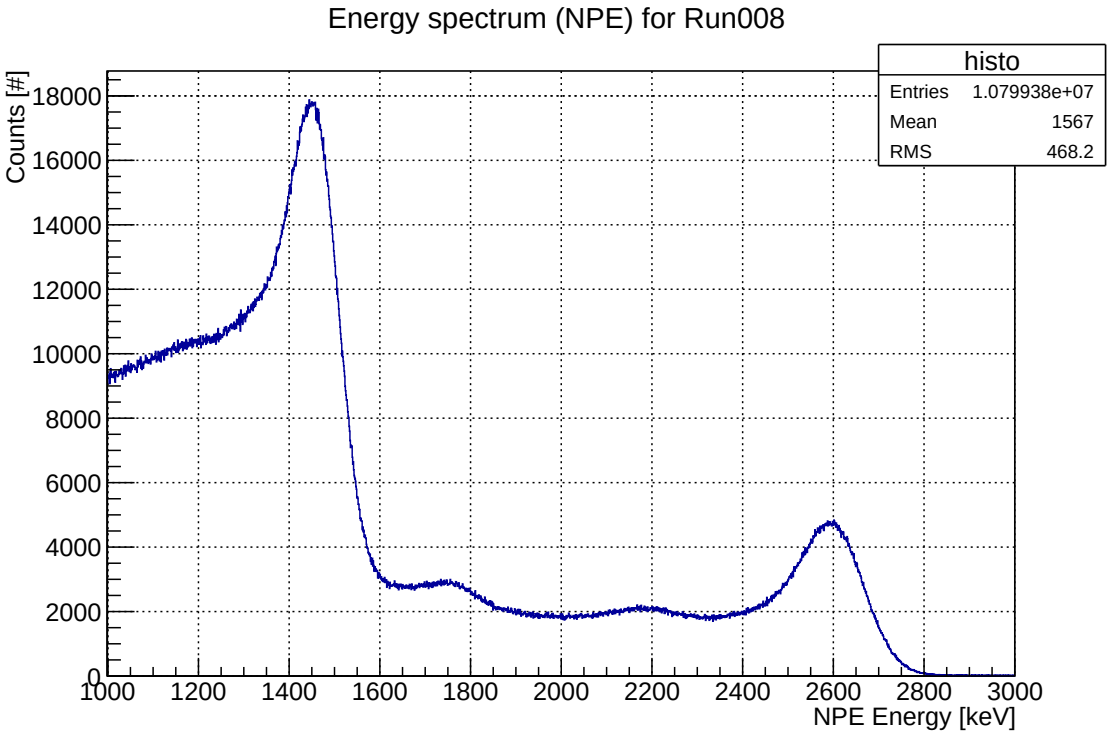

Figure 8.1.: Observed low-energy spectrum for Run008 (combined data of Subrun 3-41) after several cuts which will be introduced later on. The left peak at around 1460 keV is caused by ^{40}K, while the second peak around 2614 keV arises due to the γ-ray emission of ^{208}Tl.

Potassium-40 is a natural radioactive isotope that is contained in almost any material inside and outside of the detector to a certain degree. The same applies for Thallium-208, as it is part of the natural ^{232}Th decay chain. Now, one can fit both peaks in order to derive important

characteristics of the obtained spectrum (e.g. peak position, number of events, width). These properties can then be used further on to analyze the stability of the detector over time by fitting each Subrun individually. In this case, ^{208}Tl is seen as the more important peak in the analysis, as it can be fit more precisely compared to the ^{40}K peak.

In the past, the spectrum fit has been performed individually with a Gaussian function for each peak (cf. figure 8.2). The procedure for fitting consists of three steps. At first, a certain energy region that contains one of the peaks has to be chosen in order to generate a one dimensional histogram (i.e. 2.4 MeV − 3 MeV for the ^{208}Tl peak). Then, in the case for ^{208}Tl, the range for the fit is set as follows:

$$\text{Lower edge: Mean} - 0.6 * \text{RMS} \quad , \quad \text{Upper edge: Mean} + 1.2 * \text{RMS}$$

Here, the "RMS" is defined as the standard deviation along the X-axis. A graphical illustration of this method can be seen in figure 8.3.

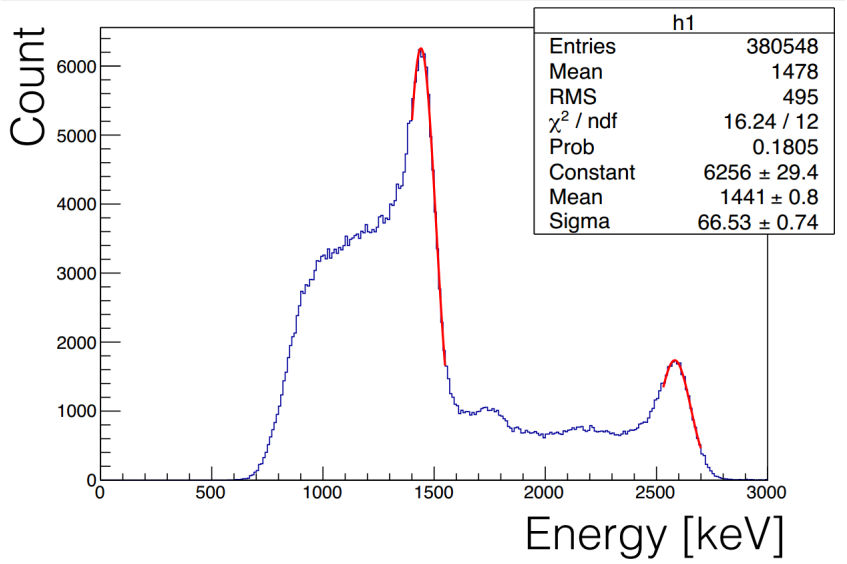

Figure 8.2.: Illustration of the fit peaks for a single Subrun in Run007. [42]

After this procedure, the peak can be fit with a Gaussian function based on the chosen fit range and important parameters like the peak position can be derived. The same fit method is used for ^{40}K, just with a different energy region in the first step. As a result, one can fit the ^{208}Tl and ^{40}K peak for every individual Subrun as well as for all the Subruns combined.

However, after executing this analysis, it can be seen that the fit Gaussian and the data peak clearly differ sometimes. This may also be based on the fact, that the peak regions are not only physically based on a single Gaussian peak. In the case of ^{208}Tl for example, it has to be expected that Thallium's Compton edge plays a significant part in the spectrum. Unfortunately, this contribution can not be seen in the spectrum due to the energy resolution and other backgrounds. Nevertheless, it can be modeled in the fit. The same applies for Potassium's energy region, because it actually contains a significant number of low energy events that can be seen at the left side of the peak. As such, a new fitting method had been suggested in the collaboration which can be seen in figure 8.4.

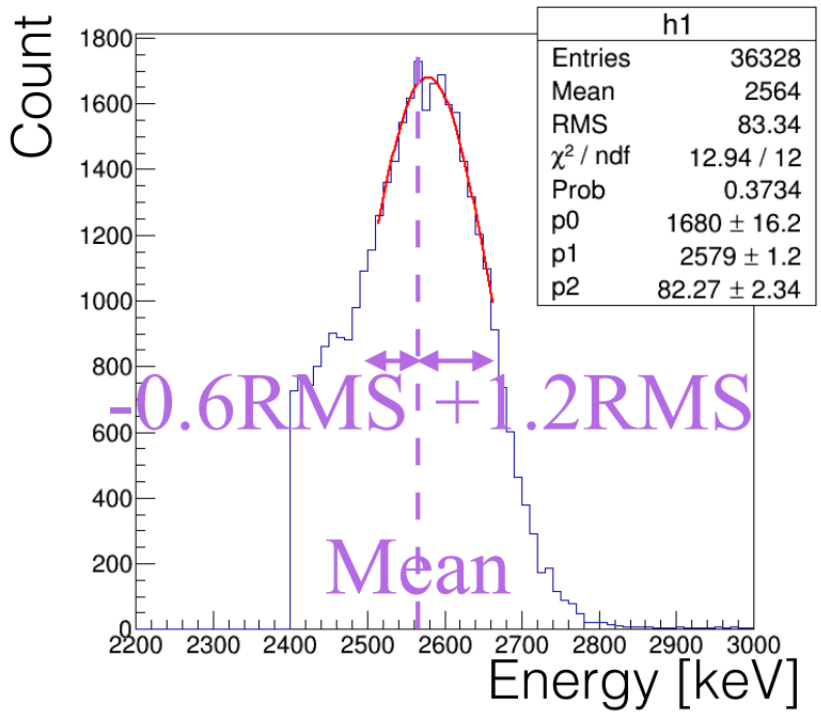

Figure 8.3.: Technique for fitting the ^{208}Tl region. The fit range is set from Mean $-$ 0.6 $*$ RMS to Mean + 1.2 $*$ RMS. [42]

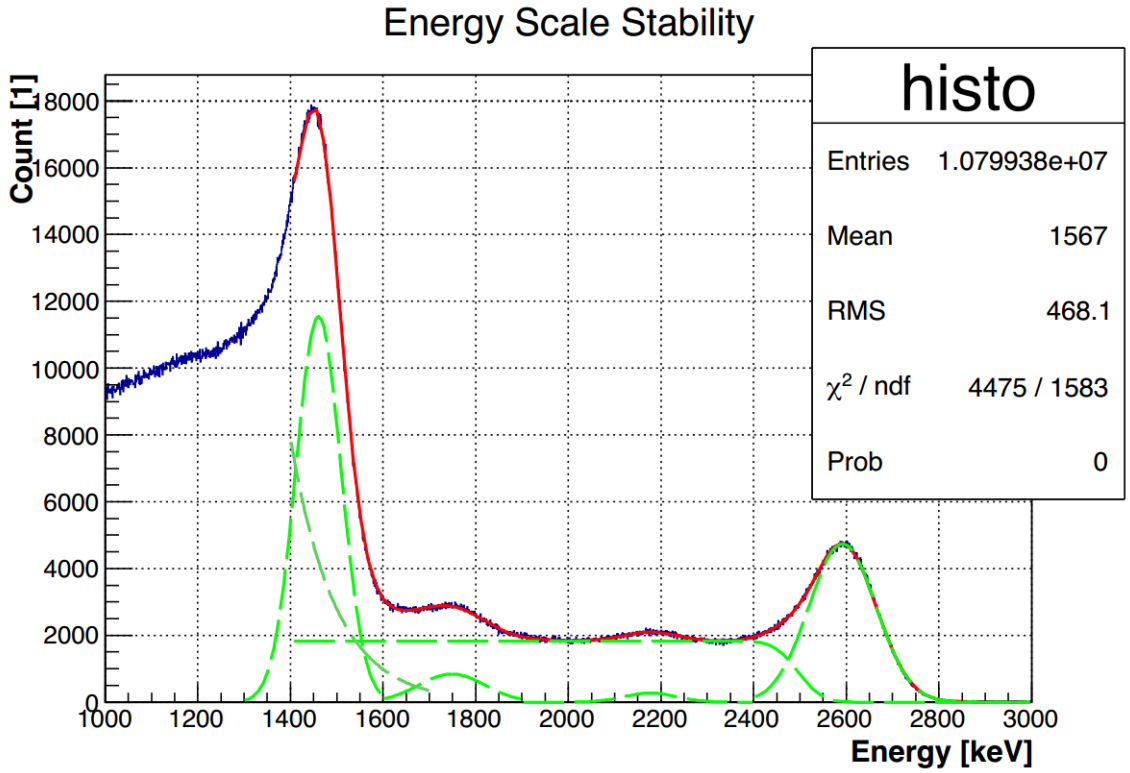

Figure 8.4.: New fitting method used for checking the energy scale and event rate stability of the detector. In this case, the fit consists of multiple functions (green) that are fit at the same time in a combined fit (red). The example shows the combined data of Run008. [42]

In this case, the whole energy region between the ^{40}K and ^{208}Tl region is modeled in a combined fit. The new technique contains the following fit functions:

- Gaussian: ^{40}K emission at 1.46 MeV
- Gaussian: H+n (neutron capture in hydrogen) emission at 2.2 MeV
- Gaussian: ^{214}Bi emission at 1.76 MeV
- Gaussian: ^{208}Tl emission at 2.6 MeV
- Error Function: ^{208}Tl's Compton edge and other unknown events that form the baseline
- Exponential: Low energy events below 1.4 MeV (e.g. Compton edge)

Up to this point in time, the method had only been tested on the combined spectrum of all Subruns for Run008. Now, the task of the following analysis in the next sections was to apply the new technique for the individual Subruns and to estimate the goodness compared to the old fit method. At the same time, the energy scale and event rate stability for the new Run009 had to be checked.

8.2. Data selection and cuts

In order to get the spectrum that can be seen in figure 8.4, several cuts have to be made. As CANDLES is looking for a beta signature inside the crystals, we want to study the energy scale of the detector with beta events that are reconstructed inside the CaF_2 crystals. Thus, the applied cuts are as follows:

- DataQuality[0,1,2,3]=0 in order to remove noise like events with saturated or overshot PMTs and also clock trigger events.
- (TriggerCounter33|TriggerCounter36)&0x4)! = 0. This rejects events that are only originating in the liquid scintillator (LS) based on the dual gate trigger system (DGT) with high efficiency.
- CrystalN[1] != 0. Based on the position reconstruction described in chapter 7, events within 2σ of the Gaussian distributions are selected. Previous analysis has shown that the weighted mean positions of reconstructed events (in the used energy region) with a 2σ selection are well contained inside the crystals. Thus, it also compliments the DGT cut.
- PSDPara4 < 2 ($\chi^2_\beta < 2$) for selecting beta events, which also includes γ-ray signals. The typical "tight" cut that is used in the search for $0\nu\beta\beta$ is based on a value of 1.5. In this analysis we employ a more loose cut of value 2 in order to get more events and thus better statistics for the Subrun fitting. This still means that most α events are rejected (cf. figure 7.4). However, because the pulse shape of β and $\beta + \text{LS}$ (e.g. $\beta + \gamma$) is a lot closer than α to β, $\beta + \text{LS}$ (primarily CaF_2 + LS) events are not efficiently rejected by this cut. Nevertheless, CaF_2 + LS events with a significant deposit in the liquid scintillator are already rejected by the position cut.

Over the course of this analysis we will study Run008 as well as Run009 data. The data for Run008 is used in order to compare the new fit method to the old method, while Run009 data is utilized for the ongoing investigation of the detector stability.

Before the energy for each of those Runs can be calibrated, it is necessary to keep all PMTs at the same gain. One possibility is to match the ADC (analog-to-digital converter) channel of a photopeak for all PMTs. However, due to the small number of photoelectrons (about 1000 per

MeV) in CANDLES, it is not possible to get the photopeak individually for each PMT. In this case, one has to assume that the gain for all PMTs is about the same. After this, the energy scale can be calibrated by using a ^{88}Y source (cf. [27] for further information). As a result, the so called "ADC-Energy" is derived. Another option is to employ one photoelectron measurements for each PMT and then adjust the high-voltage supply in order to obtain the same gain. Then, after the ^{88}Y calibration, one can derive a second energy called "NPE-energy".
Thus, we get the energy of an event based on two different gain matching techniques: ADC-Energy (no adjustment) and NPE-Energy (with adjustment). Both derived energies should be about the same if the gains of the PMTs are similar. Previous experience shows that the difference between both energies is small ($< 0.5\%$) and significantly less than the energy resolution of 2% at the Q-value of 4.27 MeV.

An important part of this analysis is to check, how well these two types of reconstructed energies agree or differ.

8.3. Analysis for Run008 and comparison to the old fitting

In order to get a clue about the performance of the new fitting technique, one can analyze old data from Run008. In this case, the old fitting method was already applied for the data such that we can compare them with the results of the new approach. Prior to this, the analyzing scheme for the new method has to be developed.

Workflow of the new fit approach

The first step in analyzing the data with the new technique is to fit the energy spectrum for the combined Subrun data of the Run. In this case, an energy spectrum from 1 MeV to 3 MeV is generated based on the chosen cuts. Although the previously selected bin size in the old method of 1 keV per bin is very small, it is not changed in order to keep the data basis of the analysis comparable to the old fitting technique. After this, the energy spectrum is fit individually in appropriate energy ranges with each of the fit functions specified in section 8.1. In this way, start parameters for the combined fit (all model functions combined into one total fit) can be derived. Then, the final, combined fit is executed and the whole method can be applied for the ADC-Energy as well as for the NPE-Energy. The result for the ADC energy spectrum can be found in figure 8.5.

After fitting the combined data of Run008, the next step is to fit each Subrun one by one. In this case, we can use the results of the fit parameters (e.g. peak position, width, etc.) as start parameters for the Subrun fits. Additionally, limits for the parameter regions are set as the start parameters $\pm 3\%$. This supports the fit algorithm, as the combined fit function has many parameters that have to be estimated. Other than that, it is suspected that the minimizer has more difficulties in the Subrun fit, because the statistics are a lot lower compared to the fitting for the whole data of a Run.
Previous analysis shows that the fluctuation on main parameters like peak position for ^{208}Tl and ^{40}K over time is less than 1%. As such, this parameter region is sufficient for the Subrun fits.
After executing all of the single fits, it can be seen in figure 8.6 that the fitting works well for both high (normal Subruns, about 24h of data) and low statistics (early stopped Subruns, e.g. due to work that is being done on the detector) Subruns in Run008.
At this point, all important parameters of the fit can be derived for both the combined Run008 fit as well as for the Subrun fits.

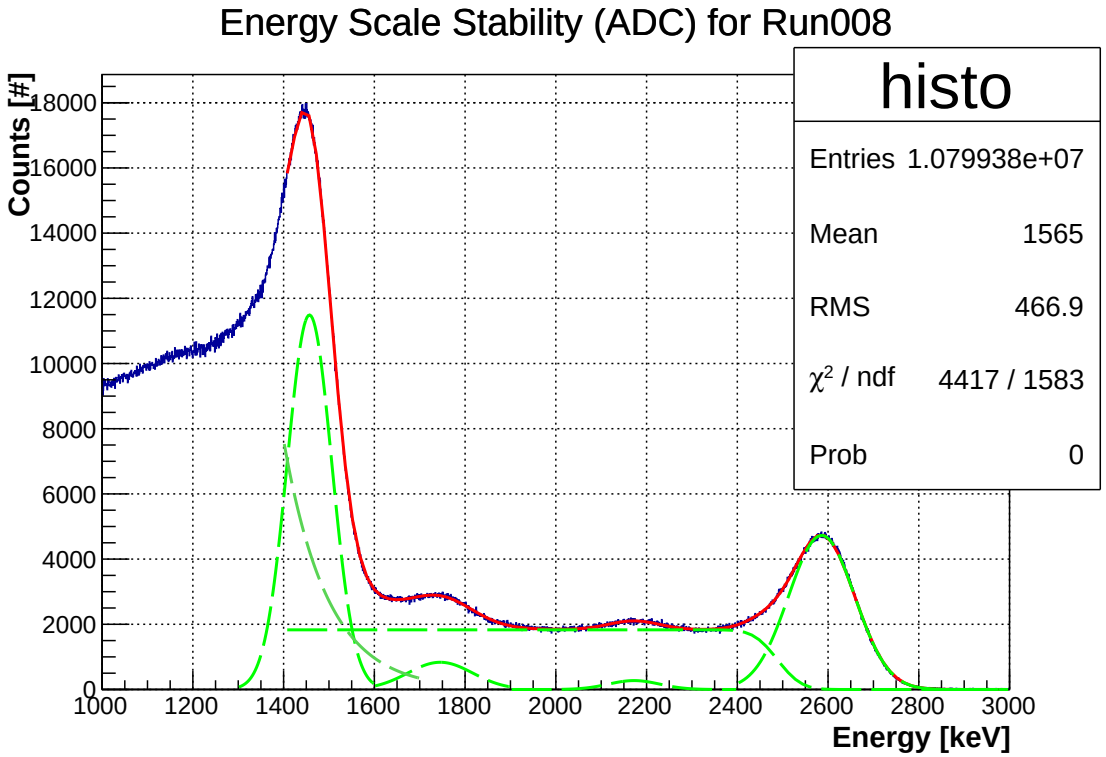

Figure 8.5.: Result of the new fit technique for the ADC energy spectrum of Run008. The combined fit result is shown in red, while the green curves illustrate the participation of each single function in the combined fit.

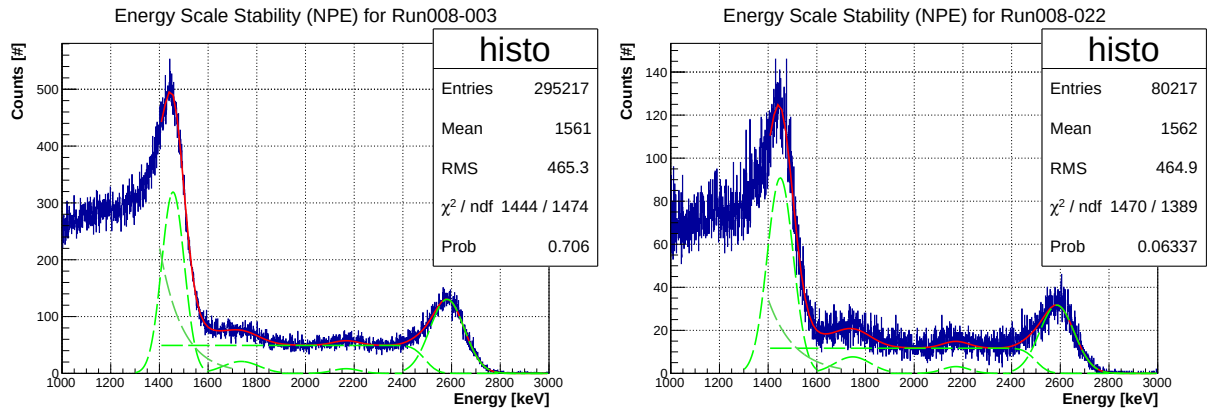

(a) A high statistics Run with about 24h of Data

(b) A low statistics Run

Figure 8.6.: Subrun fitting for the NPE-Energy spectrum of Run008. The fitting works well for both high and low statistics Subruns.

Another goal of this analysis that hasn't been presented in detail yet is checking the event rate stability. In particular, only the relative change in event rate over time is important and not the absolute scale. As such, the event rate for e.g. ^{208}Tl can be calculated by integrating the peak region in a certain interval. The particular energy regions for integration, which are the same as in the old fitting method, are defined as follows:

$$^{208}\text{Tl} : \text{PeakPos} - 3\sigma \text{ to PeakPos} + 3\sigma$$

$$^{40}\text{K} : \text{PeakPos to PeakPos} + 2\sigma$$

σ is the fit Gaussian width of each peak (^{208}Tl, ^{40}K) and it is derived by the combined Run data fit (the fit which is executed on the whole data of a Run)."PeakPos" is the energy peak position for every Subrun fit. Thus, the event rate for each Subrun is calculated with a fixed σ (based on the total Run data fit) and an individual "PeakPos" for every Subrun. After that, dividing the resulting number of events (N) by the livetime of a data set yields the event rate. As we are measuring integer values of counts in the energy spectrum, a poisson distribution of the data can be expected. In this case, we can calculate the error on the event rate by estimating the variance on the number of events with a factor of $\sqrt{N}$. This is only an approximation of the true variance. In our case however, the statistics is high enough ($\gg 100$ events) for both the Run008 and Run009 data such that the assumption is valid.

Analysis of Run008 data and comparison to the old fit method

At this point, the results of the fit can be investigated. Before analyzing new data from Run009, old Run008 data is investigated in order to reproduce the results that were based on the old fit method. For this purpose we present the analysis results for Run008 based on the new method and compare them to the results based on the old fit method (only done for ^{208}Tl).
Initially, the fit peak positions for ^{208}Tl and ^{40}K, based on the new fit method, can be reported:

	NPE-Energy	ADC-Energy
^{208}Tl	(2591.9 ± 0.3) keV	(2585.6 ± 0.3) keV
^{40}K	(1460.5 ± 0.4) keV	(1457.1 ± 0.4) keV

Table 8.1.: Energy peak positions for the combined Run008 data.

The related NPE/ADC energy spectra can be found in the appendix (subsection A.1.1). Based on the results from table 8.1, it can be seen that the difference between the NPE and ADC energy is small and thus acceptable: it is less than 0.5% compared to an energy resolution of about 4% at 1.836 MeV which is derived from CANDLES energy calibration measurements.

Other than that, it is important to analyze the peak stability of the detector over time. For this purpose, one can plot the peak position of e.g. ^{208}Tl for every Subrun, cf. figure 8.7. In order to validate the new analysis, the results can be compared to the old results based on the old fit method, shown in figure 8.8. It can be seen that the shape of the ADC and NPE curves agree for both methods. This also applies to the fluctuation of the peak positions which is about ± 10 keV.

The only significant difference between the new and the old fit method is a positive offset in the peak energy of about +5 keV. The principal difference in the fitting for both methods (^{208}Tl peak region) is the introduction of the Compton edge. As seen in figure 8.9, this can cause a positive shift in energy compared to a Gauss-only fit.
It's reasonable to assume that the difference is based on the addition of the Compton edge fit in the ^{208}Tl peak region. However, this fact shows that fitting the ^{208}Tl region proves to be difficult, due to the correlation of the Compton edge and the Gauss. Unfortunately, the Compton edge itself can't be seen in the energy spectrum. Thus, its existence and participation in the spectrum can only be assumed based on a physical point. This issue will be reviewed again later on.

Apart from the fluctuations of the energy peak positions over time, it is also important to derive how much the peaks fluctuate relative to their energy. For this purpose, one can create a one dimensional histogram that contains the peak position for every Subrun, like it was already done in the past. The NPE-Energy result is shown in figure 8.10 and a figure for the ADC-Energy can be found in subsection A.1.2.

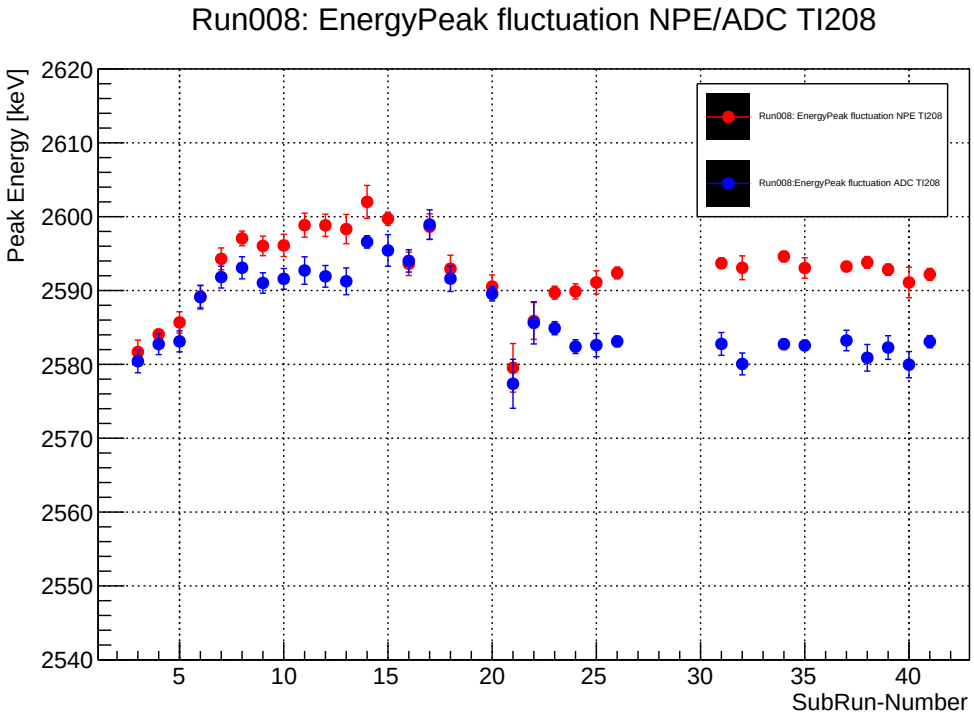

Figure 8.7.: NPE/ADC peak positions of ^{208}Tl for every Subrun. NPE results are shown in red, while ADC results are shown in blue.

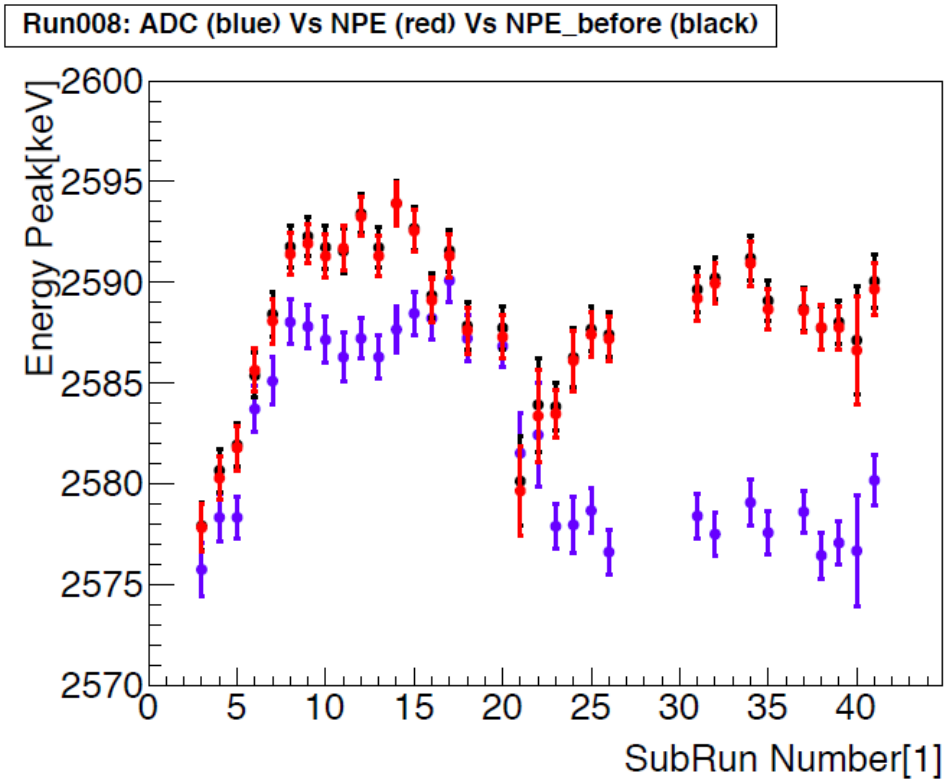

Figure 8.8.: NPE/ADC peak positions of ^{208}Tl for every Subrun based on the old fit method. NPE results are shown in red, while ADC results are shown in blue. The shapes of the curves agree with the new fitting method. [42]

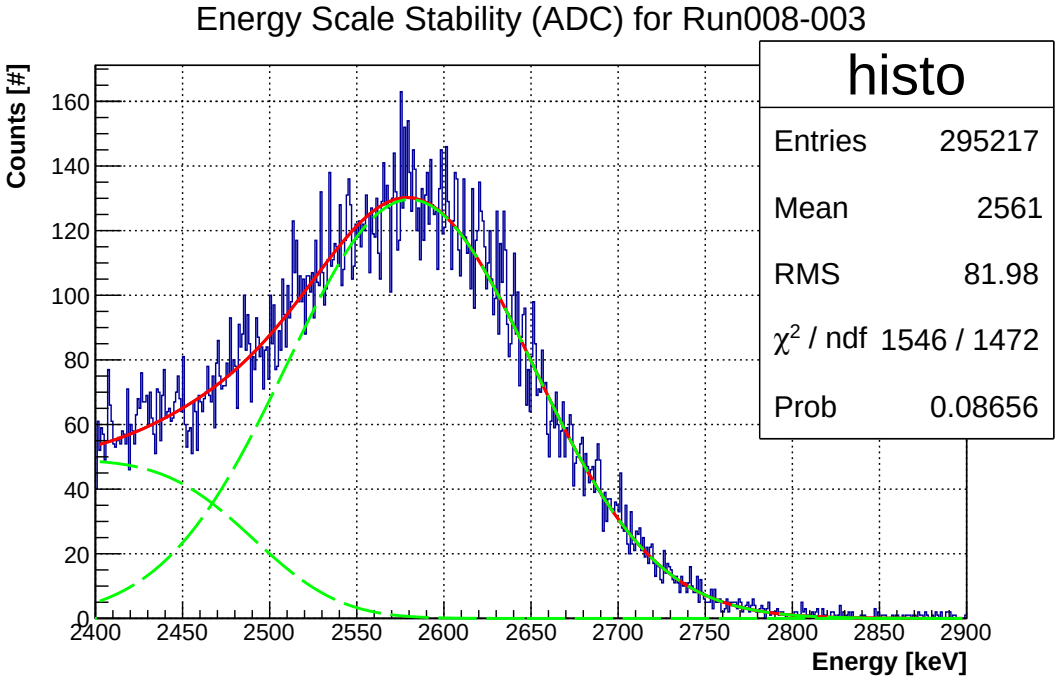

Figure 8.9.: Energy spectrum of Run008-003 in the ^{208}Tl region. It can be seen that the introduction of the Compton fit causes a small, positive shift in energy compared to a Gauss-only fit.

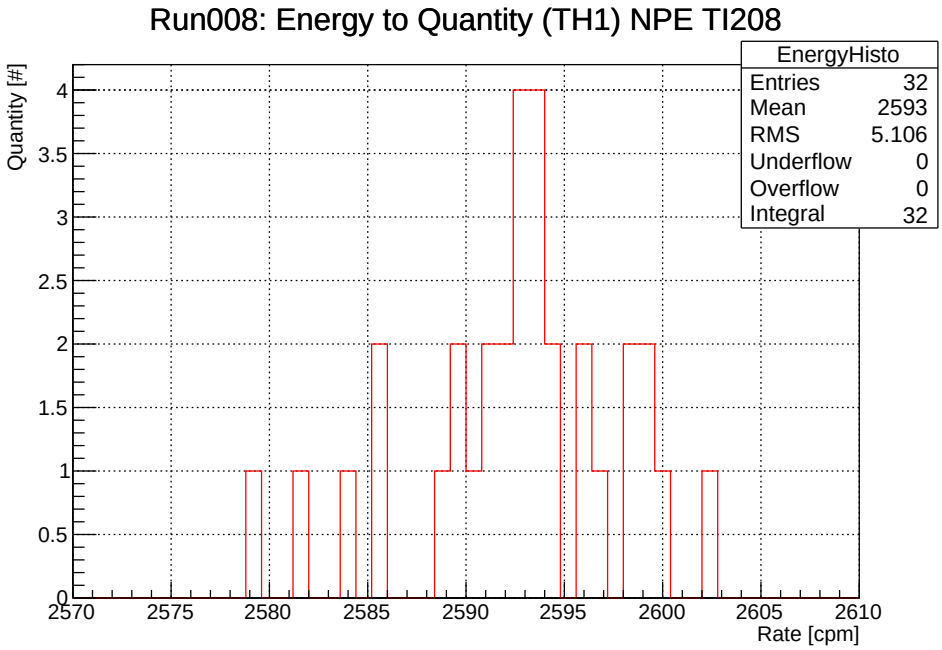

Figure 8.10.: ^{208}Tl NPE energy histogram that contains the peak position of all Subruns. The value of RMS/Mean has been used in the past to estimate the scale of the energy fluctuation. In this case, RMS/Mean = 0.19%.

Principally, this histogram is only used in order to calculate a value for the scale of the energy fluctuation based on the RMS/Mean. Calculating this value yields 0.19% with the new fit and 0.18% with the old fit. Thus, the energy peak variation based on the value of RMS/Mean is basically the same.

As already mentioned, not only the energy peak position but also the event rate for a peak shall be investigated. In this analysis, the event rate should be stable over time if no new background is introduced to the detector. As ^{208}Tl $\beta + \gamma$ events are a major background in the Q-region, it is important to monitor the event rate for the 2.6 MeV γ peak. In this case, additional background that can be caused by work being done on the detector would result in a sudden change of event rate. The fluctuation of the event rate for ^{208}Tl over time for both the new and the old method can be found in the figures 8.11 and 8.12.

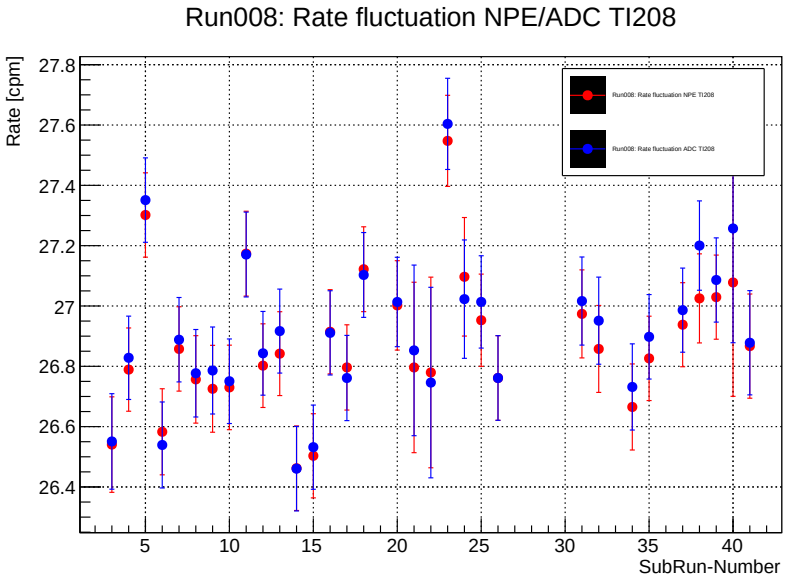

Figure 8.11.: Calculated event rates for the ^{208}Tl energy region based on the NPE/ADC energy spectra (red/blue) with the new fit method.

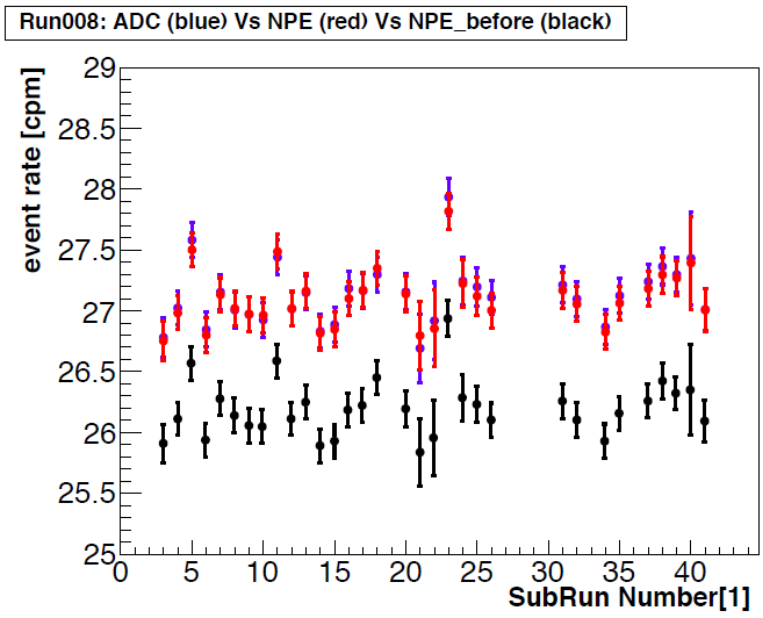

Figure 8.12.: Calculated event rates for the ^{208}Tl energy region based on the NPE/ADC energy spectra (red/blue) with the old fit method. NPE results are shown in red, while ADC results are shown in blue. The points marked in black should be neglected.

As expected, the event rates based on the NPE and ADC energy histograms agree very well for the new fit method. Additionally, the shape and the scale of the event rate curve is principally the same as with the old fit method. At this point, we can estimate the variance on the event rate with the same method that was used for the energy peaks. The value of RMS/Mean is 0.84% for the new and 0.85% for the old fit method (NPE), which is stable. Thus, the new result agrees very well with the old result. The related histograms can be found in subsection A.1.3.

As a conclusion, it can be said that the results of the new and old fit method generally agree. The only significant difference is a positive offset in energy for the ^{208}Tl peak which is based on the inclusion of the Compton edge to the fit function. Now, new data from Run009 can be investigated with the same methods.

8.4. Analysis for Run009 data

In this section, the results of the analysis for new data in Run009 will be reviewed. Usually, the energy scale and event rate stability is checked every three months when new data is available (Analyzed files, c.f. figure 6.4, are created in bunches and not on a daily basis). Run009 has been started in April and the Physics Subruns of number 0-60 were recorded in a non-stable environment (e.g. temperature), as work was still being done on the detector and DAQ. After this, data has been collected with stable conditions starting from Run009-069 till Run009-158. In this case, every Subrun is equivalent to about a day of measurement time. The analysis has been performed for all Subruns that were recorded. In this work however, we will only present the last analysis for Subruns 69 to 158 with stable conditions, in order to keep the scope of this chapter reasonable. Additionally, the major flaws of the new fit method and an outlook will be given. At first however, the major detector differences of Run009 compared to Run008 will be discussed.

Differences of Run009 compared to Run008

Between the end of Run008 and the start of Run009, there were two major changes concerning the detector. At first, the DAQ system was changed significantly. This subject will be further discussed in chapter 9, as it is not important for the analysis of the energy scale and event rate stability. Secondly, the lead and boron shield has been constructed. This has a significant effect on the analysis, as the expected statistics of Run009 per unit time is a lot lower. In example, both the ^{208}Tl and ^{40}K peak are based on γ-ray emissions. Due to the additional lead shield, γ-rays from the outside of the detector will be shielded significantly. Thus, the expected total event rate for e.g. the internal and external background of ^{208}Tl will be lower than in Run008. The experimental confirmation of this assumption can be seen in figure 8.13.
Based on the combined Run008 and Run009 data, it can be estimated that the reduction in the number of events (1 MeV to 3 MeV) for Run009 to Run008 is about 1/4. This also applies for the energy spectra of individual Subruns, as shown in figure 8.14.
As a result, the Subrun fitting in Run009 gets more difficult due to the lower number of events.

Analysis results for Run009 (Subrun 69-158)

At this point, the data of Run009 (Subrun 69-158) can be investigated in-depth. The first step is to fit the combined Run009 data, whose result is shown in figure 8.15.
The related NPE energy spectrum can be found in figure 8.13, or in subsection A.2.1.
Based on figure 8.15, it can be seen that the H + n Gauss peak at 2.2 MeV has nearly completely disappeared due to the new detector shield. At the same time, a new peak has emerged at about 1.95 MeV. It can only be seen in the combined Subrun spectrum and the origin of the peak is not known yet in the collaboration. There are two main possible options for the source of the bump.

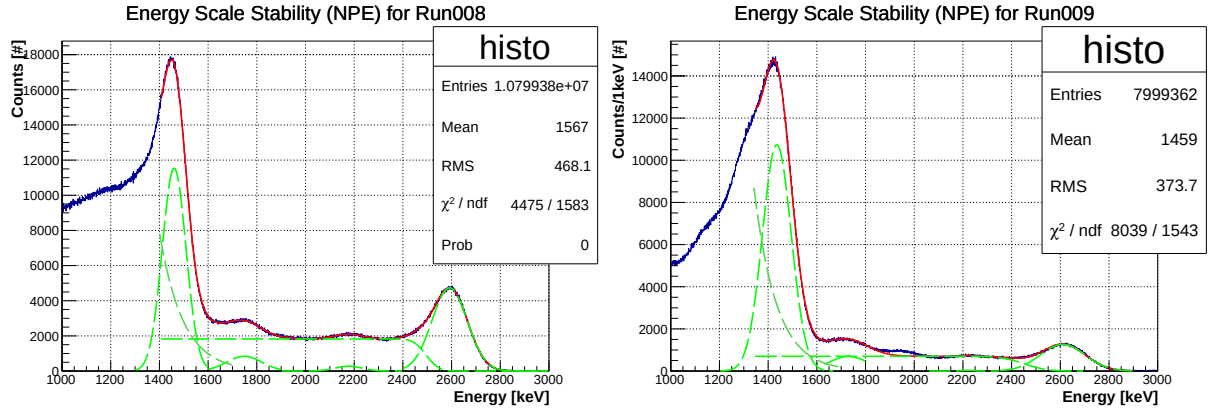

(a) Run008 (Subrun 3-42) (b) Run009 (Subrun 69-158)

Figure 8.13.: NPE energy spectra for combined Run009 and Run008 data. The statistics of Run009 per unit time is significantly lower. A reduction factor for the number of events can be derived after a correction for the different measurement times (livetime) of Run008 and Run009 has been applied. Based on the number of events in the range of 1 MeV to 3 MeV, the ratio of Run009 to Run008 events is about 1/4.

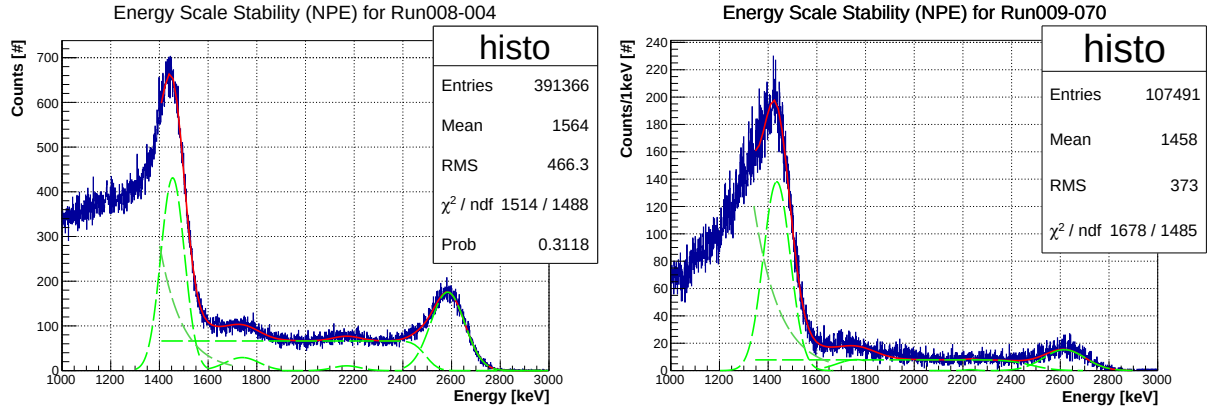

(a) Run008-004 (b) Run009-070

Figure 8.14.: NPE energy spectra for the individual Run008-004 and Run009-069 Subruns. Both Subruns have a measurement of about 24 hours. As expected, the observed ratio in the number of events of Run009 and Run008 is also about 1/4.

The first possibility is that the peak is based on background contained in the new detector shield. This is unlikely though, as the chemical composition of the lead blocks and the boron sheet is known. Nevertheless, the new small peak could also have been hidden in the higher (external) constant background before the shield construction. As this issue is not the subject of the analysis, it will not be further investigated.

Based on the fits for the combined Run009 data, the peak positions for both ^{208}Tl and ^{40}K can be derived. The result is shown in table 8.2.

	NPE-Energy	ADC-Energy
^{208}Tl	(2610.2 ± 0.2) keV	(2580.2 ± 0.2) keV
^{40}K	(1435.7 ± 0.2) keV	(1420.3 ± 0.2) keV

Table 8.2.: Peak positions for the combined Run009 data (Subrun 69-158).

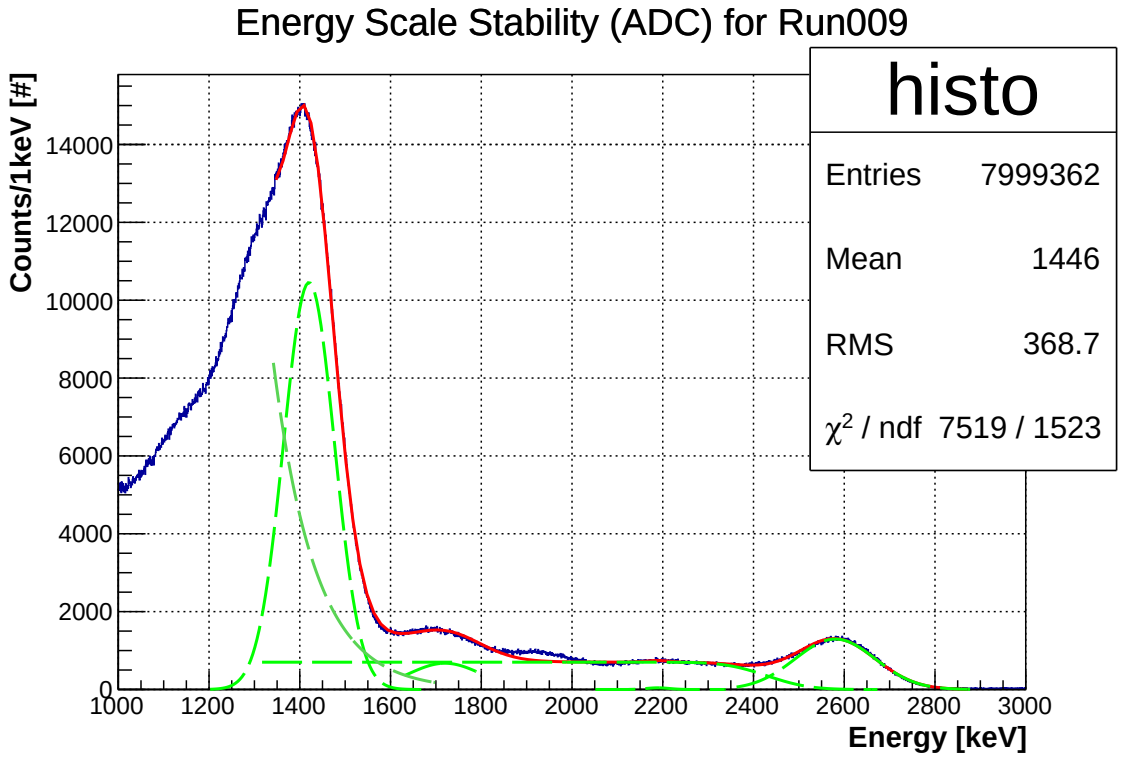

Figure 8.15.: ADC energy spectrum for the combined Run009 data (Subrun 69-158).

The peak positions for both the ADC and NPE spectra show that there is a significant energy difference. For the Potassium-40 energy peak, the discrepancy is about 15 keV. The same applies to the Thallium-208 peak that shows a gap of about 30 keV. This result for ^{208}Tl is what one would expect if a linear energy scale and error is assumed. The origin of the difference in ADC and NPE energy could be based on currently known problems with the PMT baselines.

However, it can be reported that both the NPE and ADC results have difficulties in reproducing the known literature values for ^{208}Tl (2614 keV) and ^{40}K (1460 keV). This time, especially the observed peak energy for ^{40}K is about -25 keV (NPE) to -40 keV (ADC) off. The difference for ^{208}Tl is smaller though with about -4 keV (NPE) to -34 keV (ADC). If the difference of the observed values to the literature value is based on a nearly constant error, we would expect a larger discrepancy in the peak values for Thallium-208. However, this issue could also be based on the fact that the ^{208}Tl peak is difficult to estimate due to the unknown contribution of the Compton edge.

This means that its participation in the Thallium-208 peak region can only be assumed based on a physical point of view. As a result, the contribution of the Compton edge is restricted by imposing a limit on the corresponding fit function (error function). For this purpose, we can set an upper limit for the parameter that defines the X-axis position when the error function has decreased to a Y-value of 1/2. Thereby, this parameter of the error function is always caught in an upper limit for the combined data fits as well as for the single Subrun fits. The difference between a free and a fixed Compton edge fit can be seen in figure 8.16.
Though this is not ideal, it prevents larger peak position fluctuations in the Subrun fits that are only based on the fit method. If no limit is set, the ratio of Compton edge events to peak events fluctuates between about 10-70% in the Thallium-208 region. On top of that, this analysis is mostly interested in the relative change of the peak position over time, in order to check the detector stability. Hence, a precise determination of the absolute peak position is desirable, but

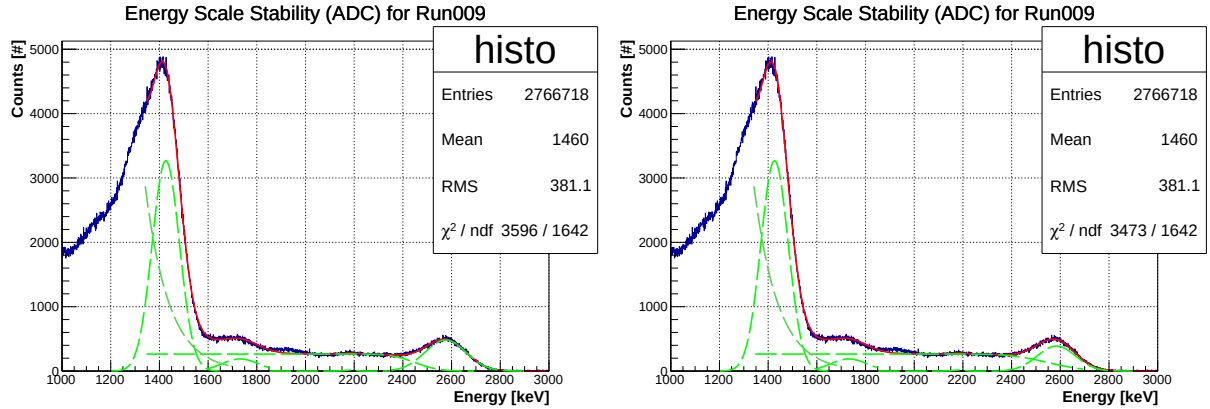

(a) Run009 with a limited Compton edge fit (b) Run009 with a practically free Compton edge fit

Figure 8.16.: Fit energy spectra for Run009 (Subrun 36-80). In the left case the contribution of the ^{208}Tl Compton edge is limited, while in the right case it is practically not limited. Practically not limited means that the fit is not caught in a parameter limit, while a larger upper limit still exists (in order to help the fitting algorithm). The difference between both fit results is about 9 keV.

not necessary. Thus, the ^{208}Tl errors that are shown in table 8.2 are realistically a lot larger. The same issue principally also applies to the ^{40}K energy region due to the exponential and Gaussian fit functions. In this case though, the ratio of exponential to peak events does not change significantly for the individual Subruns. Hence, no limit is set. However, the real ratio (and also the shape) of background events to peak events is not known. As a result, the errors on the ^{40}K peak position should be considered with caution.

Keeping these issues in mind, the peak positions for every Subrun can now be investigated. The result is shown in figure 8.17.

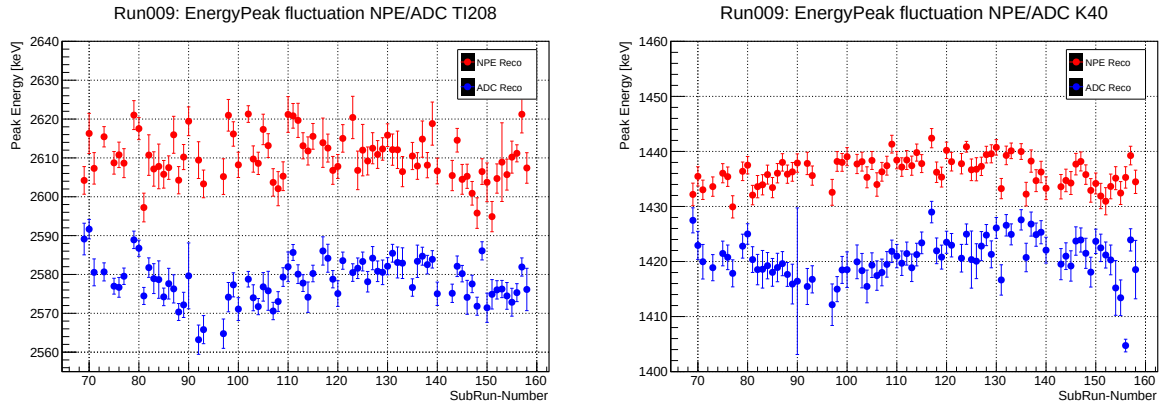

(a) ^{208}Tl peak positions (b) ^{40}K peak positions

Figure 8.17.: NPE and ADC peak positions of ^{208}Tl and ^{40}K for every Subrun. NPE values are shown in red, while ADC values are shown in blue. It can be seen, that there is a constant gap between the NPE and ADC values. The individual fluctuations for NPE or ADC however are stable.

Based on these figures it can be seen that there is a constant gap between the NPE and ADC energies for both peak types. On the other hand side, the individual fluctuations for each energy type can be considered as stable.

As previously introduced, an estimation on the scale of the fluctuations can be derived by calculating the RMS/Mean value:

	NPE: RMS/Mean	ADC: RMS/Mean
^{208}Tl	0.23%	0.21%
^{40}K	0.18%	0.26%

Table 8.3.: RMS/Mean for the fluctuations of the Run009 Subrun data (Subrun 69-158).

This fluctuation is similar to Run008 and can be considered as small enough, considering the energy resolution of the detector (about 4% at 1.836 MeV). At the same time, the curves for the same energy type (ADC/NPE) look similar if one compares the ^{208}Tl to the ^{40}K result. For the ADC spectrum of ^{208}Tl, a small dip can be seen from Subrun 92 to 97. However, it cannot be clearly derived based on the ^{40}K ADC spectrum. Work reports from Subrun 92 indicate that the position of the high voltage cable of PMT-52 has been changed during that time. On top of this, it is noted that the voltage of PMT-52 was mistakenly set to "1532" instead of "1500" after the cable was reattached. The issue had been fixed before the start of Subrun 98, whose ^{208}Tl ADC peak is not in the energy dip anymore. On the other hand side, the lower energy outliers cannot be seen in neither both NPE spectra nor the ADC ^{40}K spectrum. Thus, a direct connection between the error and the energy spectra cannot be established.
On the same account, it can be seen that the ADC peak energy for ^{40}K has a comparatively large error in Subrun 90. The corresponding energy spectrum is shown in figure 8.18.

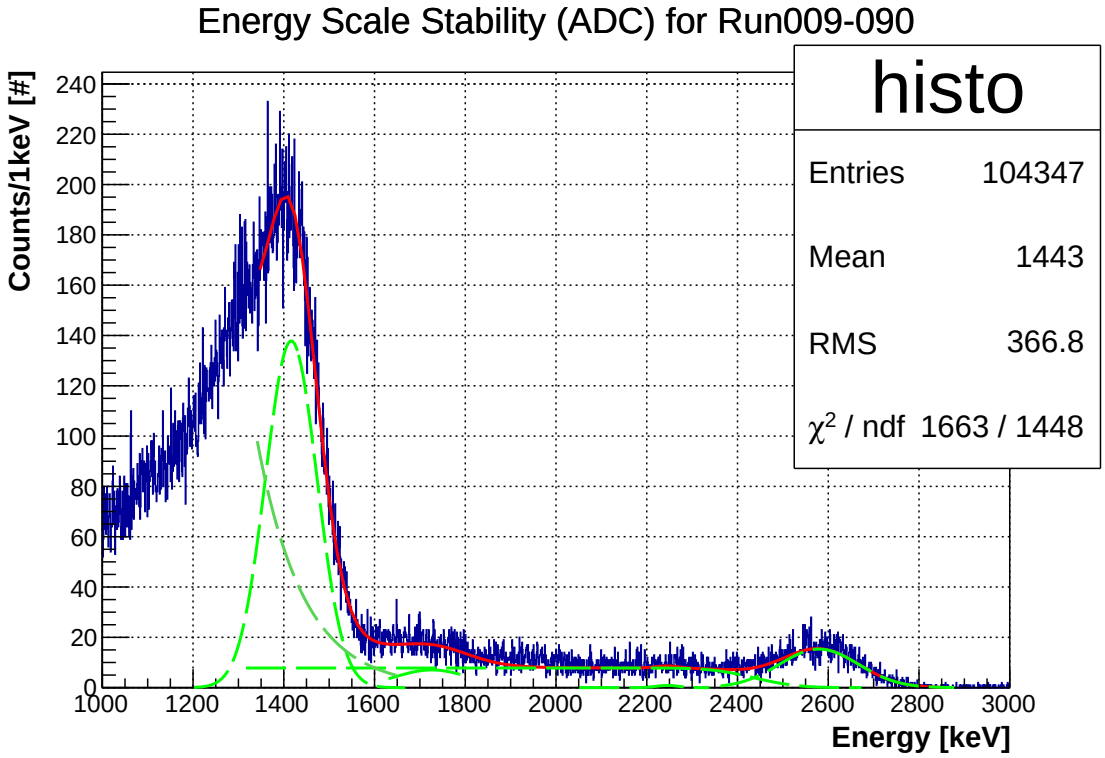

Figure 8.18.: ADC energy spectrum for Run009-090. The result of the fit looks normal, though the peak estimation of ^{40}K has a large error. The error could be based on statistical fluctuations in the ^{40}K peak region.

One can see that the fit and the energy spectrum itself looks normal. Furthermore, the used minimizer in the fit, "Hesse", gives accurate parameter errors on the peak position of Potassium-40. Details on the minimizer and the error derivation will be given in section 8.5. Thus, no conclusive

reason for the large error can be derived, though it looks like the statistical fluctuations in the ^{40}K peak region are larger than the ones for the other Subruns. In this case, the small binning (1 keV per bin) in the analysis may be part of the origin, considering the actual energy resolution of the detector.

Having said that, Run009-156 is a similar extraordinary Subrun, as its ADC peak energy for ^{40}K is significantly lower than the peak values of all other Subruns. This time however, the reason can be seen in the energy spectrum, cf. figure 8.19.

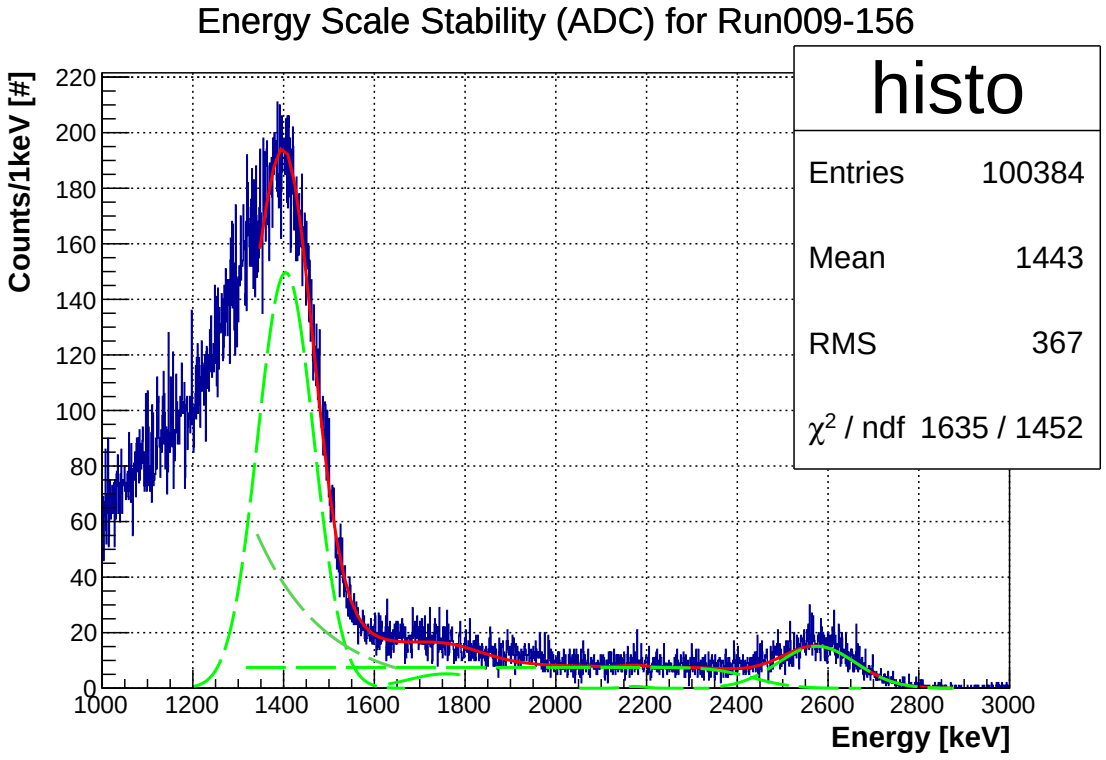

Figure 8.19.: ADC energy spectrum for Run009-156. The ratio of Gauss to exponential events is different to all other fit Subruns. It's reasonable to suppose that the Gauss moves more to the left due to its higher participation in the ^{40}K peak region.

This Subrun is the only instance, in which the ratio of ^{40}K Gauss to exponential events in the fit changes significantly. For all other Subruns (ADC/NPE), the ratio is stable. Thus, the coexistence of the Gauss and exponential fit in the same energy region poses a significant source of error for the derivation of the Potassium-40 peak position. This issue has to be kept in mind for a review later on.

Till now, the only estimation on the fluctuation of the peak positions has been done by calculating the "RMS/Mean" value. A second, newly developed method is to fit the peak positions with a horizontal fit function, shown in figure 8.20. The related figure for the ADC energies and also for the ^{40}K peak can be found in subsection A.2.2. Then, a relative error can be estimated by calculating the energy difference of the horizontal fit to the highest and lowest energy peak. Thus, it is defined as the energy region, that contains all peak energies. As a result, the errors should be interpreted as the utmost fluctuations in the data if one neglects the peak energy errors from the fit.

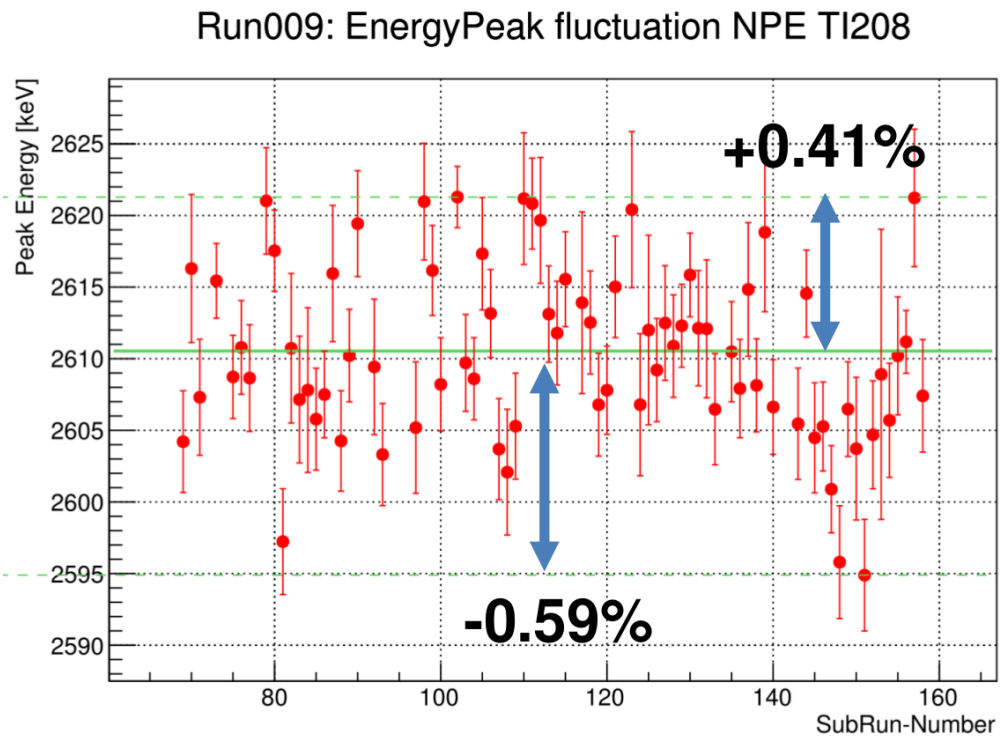

Figure 8.20.: ^{208}Tl peak energies (NPE) for each Subrun. The fluctuation of the peaks is estimated with a horizontal fit (green). Then, a relative error is given by calculating the difference to the highest and lowest energy peak.

The resulting energy fluctuation values are shown in table 8.4.

	NPE-Energy	ADC-Energy
^{208}Tl	2610.5 keV$(+0.41\%, -0.59\%)$	2578.9 keV$(+0.49\%, -0.60\%)$
^{40}K	1436.9 keV$(+0.38\%, -0.48\%)$	1420.7 keV$(+0.58\%, -1.12\%)$

Table 8.4.: Fit averaged peak energies for the Run009 Subrun data (Subrun 69-158). The braces show the relative error defined as the relative energy difference of the fit center to the highest and lowest peak energy.

The higher relative error for ^{40}K-ADC is caused by the low energy outlier that was already discussed. Neglecting this peak energy would give a similar lower error of about -0.5%, which is comparable to the upper error of $+0.58\%$. Even with this definition, the fluctuation is small compared to the energy resolution. Thus, it can be considered as stable enough.

At this point, the most important part of the analysis for Run009 has been presented. However, the event rate still needs to be checked in order to confirm the stability of the detector operation. The respective event rates for every Subrun are shown in figure 8.21.
In the case of ^{208}Tl, the NPE and ADC event rates that are calculated based on either energy spectrum agree very well. Furthermore, the shape of the event rate curve over time shows no significant change, except for a small one in the last few Subruns. This should be reviewed in the next analysis with new data. For ^{40}K, the NPE and ADC event rates still agree, but considerably worse. This is based on the fact that the calculation of the event rate for ^{40}K is problematic. As events are only integrated from the peak center to 2σ, a small change in the peak position, e.g. due to the fitting, can result in a significantly different event rate. Hence, the event rate of ^{208}Tl

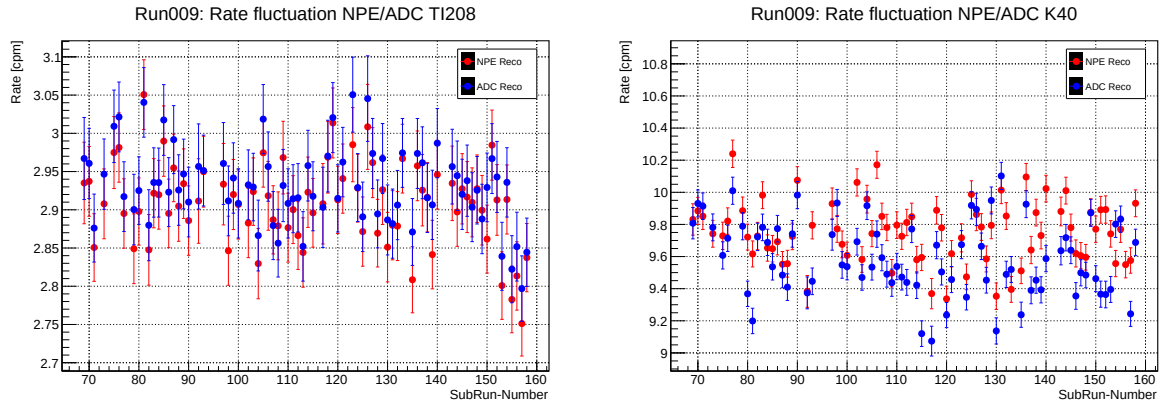

(a) ^{208}Tl event rates

(b) ^{40}K event rates

Figure 8.21.: NPE and ADC event rates of ^{208}Tl and ^{40}K for every Subrun. NPE values are shown in red, while ADC values are shown in blue. It can be seen, that there is a constant gap between the NPE and ADC values. The ^{208}Tl event rates based on ADC and NPE energy spectra agree very well. For ^{40}K, the agreement is worse due to a significantly more difficult calculation of the event rate.

should be taken as a more precise result, although the number of events per unit time for ^{40}K is higher. The fluctuations of the event rate can be derived with the same method as before and the results are listed in table 8.5.

	NPE-Energy	ADC-Energy
^{208}Tl	$(+4.9\%, -5.3\%), (\frac{\text{RMS}}{\text{Mean}} = \pm 1.9\%)$	$(+4.1\%, -4.5\%), (\frac{\text{RMS}}{\text{Mean}} = \pm 2.0\%)$
^{40}K	$(+5.1\%, -4.2\%), (\frac{\text{RMS}}{\text{Mean}} = \pm 1.9\%)$	$(+12.1\%, -5.4\%), (\frac{\text{RMS}}{\text{Mean}} = \pm 2.7\%)$

Table 8.5.: Fluctuation of the event rates for the Run009 Subrun data (Subrun 69-158). The first brace shows the relative error defined as the relative event rate difference of the fit center to the highest and lowest event rate. The second brace shows the "RMS/Mean" value.

The corresponding plots to the horizontal fits can be found in subsection A.2.3.

As with the energy peak fluctuation, the large higher error of ^{40}K-ADC is based on the low energy outlier. Without this Subrun, the higher error would be about 5%, which is comparable to the lower error of 5.4%. For ^{208}Tl, the event rate is stable within the errors that are calculated based on $\sqrt{N}$. As the ^{40}K region has more events per unit time, its errors should be smaller if the ^{40}K event rate has the same stability. However, due to the problematic event rate calculation, the errors are comparable to the case of ^{208}Tl.
Nevertheless, the event rate of ^{40}K and ^{208}Tl events in the detector can be seen as stable and no sharp change in rate is observed.

8.5. Discussion and conclusion

Based on the analysis of Run008 and Run009, it could be seen that the new fit method faces several problems in estimating the correct energy peak positions and event rates. In this section, the major issues of the used fit method are discussed and a final conclusion is given.

Review of the new fit method

The main problem of the new fit method is that it is a lot more complicated to fit. In order that the fit converges, a lot of parameter limits have to be set for the combined Run fit and also for the single Subrun fits. For an accurate description of the technical difficulties, some technical details in the fitting will be presented at first.

The primary minimizer that is used for all of the fitting is the "MINUIT" tool. With its aid, the fit function is fit by using a binned maximum likelihood approach (minimizing function). The maximum likelihood technique will be presented in detail in chapter 9. MINUIT contains multiple minimizing algorithms and two of them are "Migrad" and "Hesse". Typically, Migrad is called first, in order to minimize the negative log-likelihood and find the minimum and associated errors. However, in the case of highly non-linear fit functions or a convergence that is too fast, the parameter errors can be faulty [43]. The first issue of non-linear fit functions applies to this analysis. For this purpose, Hesse can be called in order to improve on the parameter errors. It calculates the full inverted second-derivative matrix of the minimizing function (the negative log-likelihood) in order to the derive the error matrix. In general, even Hesse is not totally precise, as it assumes a parabolic shape of the log-likelihood which results in symmetric errors. However, depending on the case, the log-likelihood can be non-parabolic due to a non-linear fit function and correlated parameters. In this case, a third function called "Minos" can be called that yields asymmetric errors. It turns out that in practice, the Minos errors are comparable to the Hesse results. However, with bad conditions (e.g. small statistics, ill-posed model), the differences can be significantly larger [43].
In our case though, Minos is not used, because it makes the analysis afterwards more difficult and first tries showed no major differences to the Hesse results. Additionally, the required extra time for the implementation would be better spent on improving the combined fit function or the analysis methods instead of improving the error estimations only marginally.

With this knowledge, we can now move on to discuss the difficulties which occur during the fitting. First of all, the fit method is considerably unstable. This means that the fit sometimes does not converge with minor changes in the fitting. In example, it has been tried to improve the fit method by changing the binning to a larger one and adding the unknown new Gauss peak at 1950 keV. The result for one of the Subruns is shown in figure 8.22.
Though the larger binning and the inclusion of the new Gauss peak would be desirable, it breaks the fitting for some Subruns. In this case, either Migrad reports a failed minimization, or Hesse finds a non-positive definite error matrix (which should not happen in the case of a minimum). Thus, the whole fit method is very unstable. The reason may very well be that the fit function contains some highly correlated parameters (i.e. the exponential and the ^{40}K Gauss, as well as the Compton edge and the ^{208}Tl Gauss). This can be directly seen by evaluating the covariance matrix of the parameters that is given by Minuit. If parameters are correlated, the minimum in the parameter space is not a point anymore, as it can become a line or a hyperplane. As a result, the fit gets a lot more difficult for the Minuit minimizer. Furthermore, parameters that are caught in the limits, like the error function (Compton edge fit), may complicate the fitting even more. As a consequence, the next iteration of the fit method should focus on easing the fitting for the minimizer.

Conclusion

As demonstrated, the current fit method has a few major weak points that should be solved in the future.
At first, the Compton edge fit should be removed from the combined fit function. As the Compton edge is hidden in the spectrum, it is not possible to estimate how it contributes to the ^{208}Tl

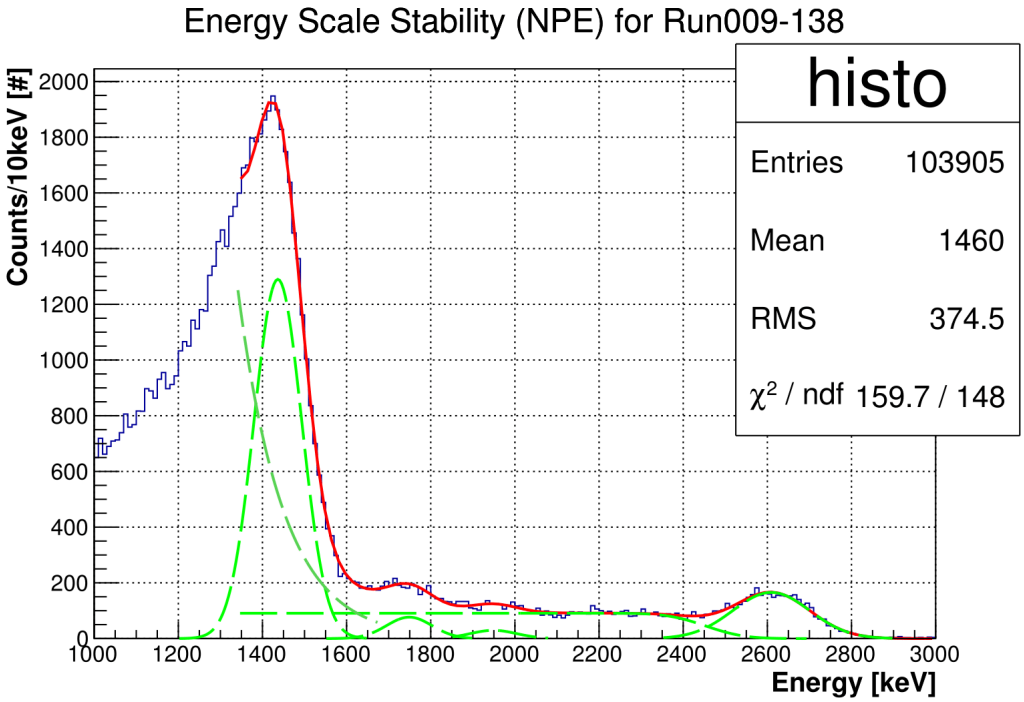

Figure 8.22.: Fit NPE energy spectrum with a larger binning for Run009-138. Additionally, the new Gauss peak at around 1950 keV is included in the fit. With these changes, the fitting breaks for some Subruns.

energy region. As such, a changing ratio of Compton to peak events in the fit may induce an artificial fluctuation on the ^{208}Tl peak position. Naturally, getting rid of the Compton edge fit does not give a better clue about the real absolute ^{208}Tl peak energy. This analysis however, focuses on the relative peak position change over time, such that removing the Compton edge fit would be the best option. Another possibility is to simulate the ^{208}Tl energy region in order to derive the correct ratio and shape of the Compton edge compared to the peak. Then, the energy spectrum could be fit based on an accurate simulation.
The second point is related to the ^{40}K energy region. In the current case, the exponential function is used to model the low energy ^{40}K Compton edge events, because the height of an error function would be difficult to estimate [44]. In practice though, previous analysis shows that the shape of the low energy region left of the ^{40}K peak is mainly caused by triggering. As a consequence, an investigation about the effect of the trigger on the low energy spectrum could make it possible to derive a better fit function than the exponential.
At last, the binning of the energy spectra should be changed to a larger one. In theory, this should help the fitting algorithm, as the number of events in one bin would rise significantly. And at the same time, the estimations on the error of each bin in the fit would be more accurate.

9. (n,γ) background study in CANDLES

As already discussed, the study of the (n,γ) background is the main topic of this thesis. Along these lines, one would like to estimate the effect of the new CANDLES detector shield on the high-energy (n,γ) background. The final goal of this analysis is to derive a (n,γ) reduction factor for rock and tank events due to the shield in the high-energy region (5.5 MeV to 10 MeV).

The energy region of 5.5 MeV to 10 MeV for the final analysis has been chosen for multiple reasons. At first, it is known that the only significant and non-trivial background in the high-energy region consists of γ-rays by (n,γ) neutron capture in the rock or in the tank. The Q-value region, on the contrary, has a lot of other background events (e.g. ^{208}Tl $\beta + \gamma$ decays). Nevertheless, this background can be reduced to a few events per year (in the energy range of 4.2 MeV to 4.5 MeV) by delayed coincidence methods. But even then, the expected (n,γ) background after the shield construction is more than ten times less compared to the leftover ^{208}Tl background. This makes an estimation of the (n,γ) background reduction based on the Q-region data very difficult. Additionally, different rejection efficiencies for the ^{208}Tl background events in the different data sets (before and after the shield construction) could distort the final result. Furthermore, the Q-value region data for Run009 is currently blinded, such that it cannot be properly used anyways. As a result, the 5.5 MeV to 10 MeV energy region is the appropriate energy range in order to study the (n,γ) background in CANDLES. Since the principal (n,γ) background mechanism in the high-energy region is the same as in the Q-region, the (n,γ) background reduction in the Q-region can be inferred by studying the reduction in the high-energy region.

For the purpose of studying the effect of the new detector shield on the (n,γ) background, one could principally just compare the Physics run energy spectrum of Run008 (before the shield) and Run009 (after the shield). However, the statistics of the remaining (n,γ) background after the shield construction is so small that the result of the analysis would have large errors. Alternatively, it is possible to use a neutron source like ^{252}Cf in order to record (n,γ) data in a short amount of time. For this work, both ^{252}Cf and Physics run data will be investigated in order to derive a (n,γ) reduction factor. In both cases, rock and tank (n,γ) events are hidden in the energy spectrum. Thus, simulation methods will be developed as well in order to estimate the individual reduction for rock and tank events.

9.1. Analysis based on neutron source ^{252}Cf data

After the construction of the shield, new Physics run data had to be recorded for a few months before it could be analyzed. Thus, a ^{252}Cf neutron source has been used in order to generate artificial (n,γ) rock and tank events.

^{252}Cf data taking

Californium-252 is a radioactive isotope that undergoes spontaneous fission with a branching ratio of about 3% [21]. During this process, several γ-rays and neutrons with energies ranging from 0 MeV to 13 MeV are emitted [45]. In one fission, 3.8 neutrons are emitted on average [21]. The energy spectrum of the resulting neutrons can be found in figure 9.1.
Thus, ^{252}Cf emits thermal ($E_n = 0.025\,\text{eV}$) as well as fast ($0.5\,\text{MeV} < E_n < 10\,\text{MeV}$) neutrons. Unfortunately, the energy spectrum of the neutrons in the experimental cave that are caused by the natural background is different. Thus, the (n,γ) reduction based on ^{252}Cf data cannot be compared directly to the reduction based on natural Physics data. This fact is most important for tank events, as the γ-rays are generated by neutron capture in the tank (which is already past the shield). In this case, the stopping power of the boron shield depends on the neutron energy. For the rock events it is not important, as the γ-rays are generated by neutron capture in the

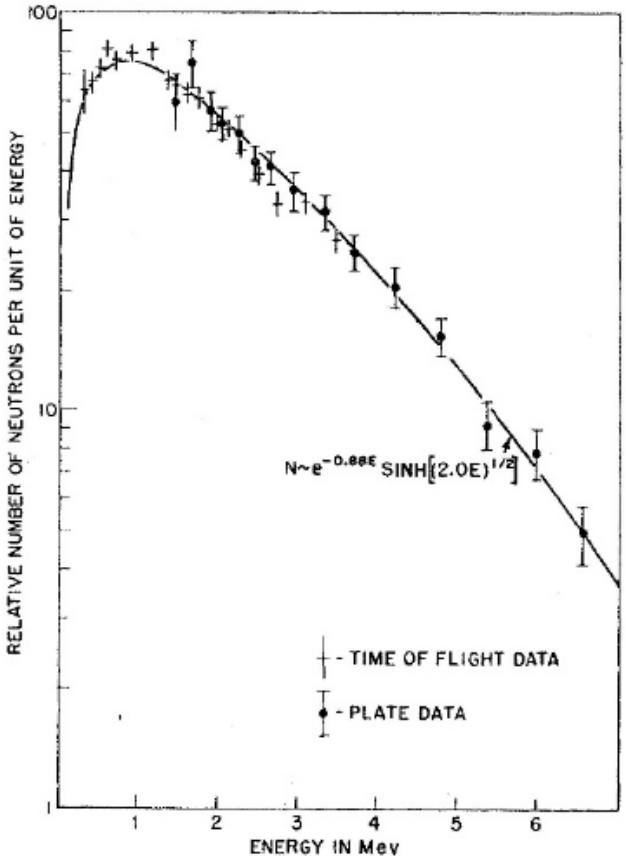

Figure 9.1.: Energy spectrum of neutrons that are emitted by Californium-252. The average of the emitted neutron energy is 2.1 MeV. [46]

rock and thus outside of the detector and shield. Hence, this can be seen as the first weak point in an analysis based on Californium-252 data.

Nevertheless, the ^{252}Cf source can be used in order to generate "Rock" and "Tank" data. This data already exists for Run008 ("Tank") and Run007 ("Rock" and "Tank") with no detector shield. The source runs for Run009 however still had to be executed. For the time of the measurements in Run009, the remaining activity of the Californium source was about 0.2 MBq. A scheme of the experimental setup in Run009 for both cases can be found in figure 9.2.

The experimental setup of the Run009 "Rock" and "Tank" runs is kept as close as possible to the setup of the ^{252}Cf runs in Run008 and Run007 (no shield), as both data will be compared later on. The particular setup for the "Tank" run in Run009 is shown in figure 9.3.

The measurement time of the "Tank" run is about four hours, though it will be seen later on that more statistics would be desirable. In this case, the ^{252}Cf source is directly attached to the surface of the shield at a height of 2 m. In Run008 and Run007, the source was put at the same height, but about 30 cm away from the tank. However, the absolute source position of Run009 to Run008/Run007 should be comparable, as the additional shield made the detector significantly thicker (e.g. 12 cm only due to the lead shield, which does not include the boron shield, additional metal struts, air gaps etc.). Additionally, for Run007 and Run008 a 5 cm thick lead block was put in between the neutron source and the tank in order to shield unnecessary low-energy γ-rays. In this analysis, we are only interested in high-energy (above 5 MeV) neutron capture events. Thus, the abundance of lower-energy γ-rays in Run009 due to the missing lead block is not a

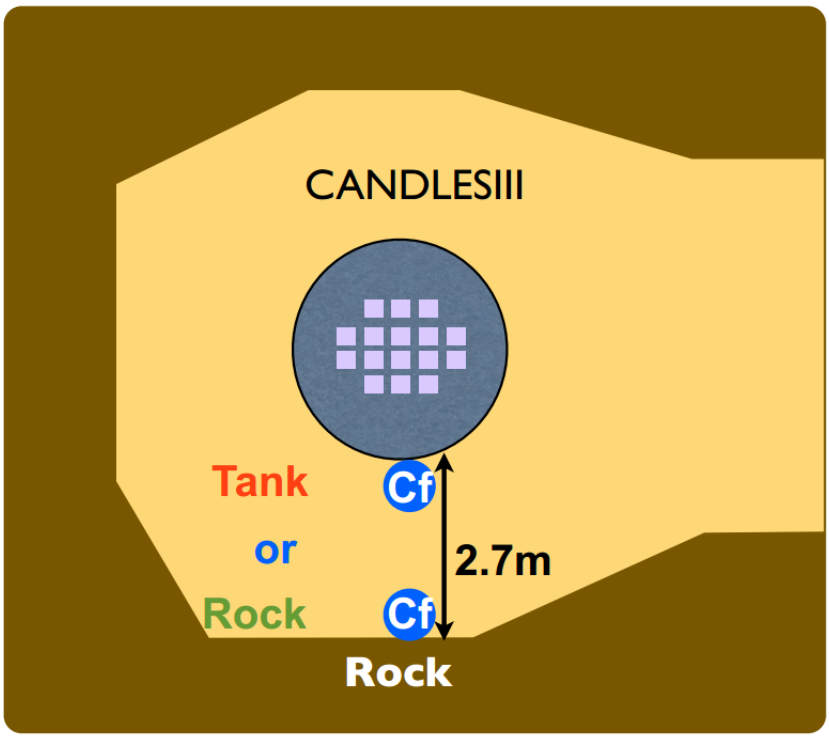

Figure 9.2.: Experimental setup of the ^{252}Cf source runs for the "Tank" and "Rock" runs. In the first case, the source is attached to the surface of the stainless steel tank and in the latter case it is put close to the southern rock of the cave. [21]

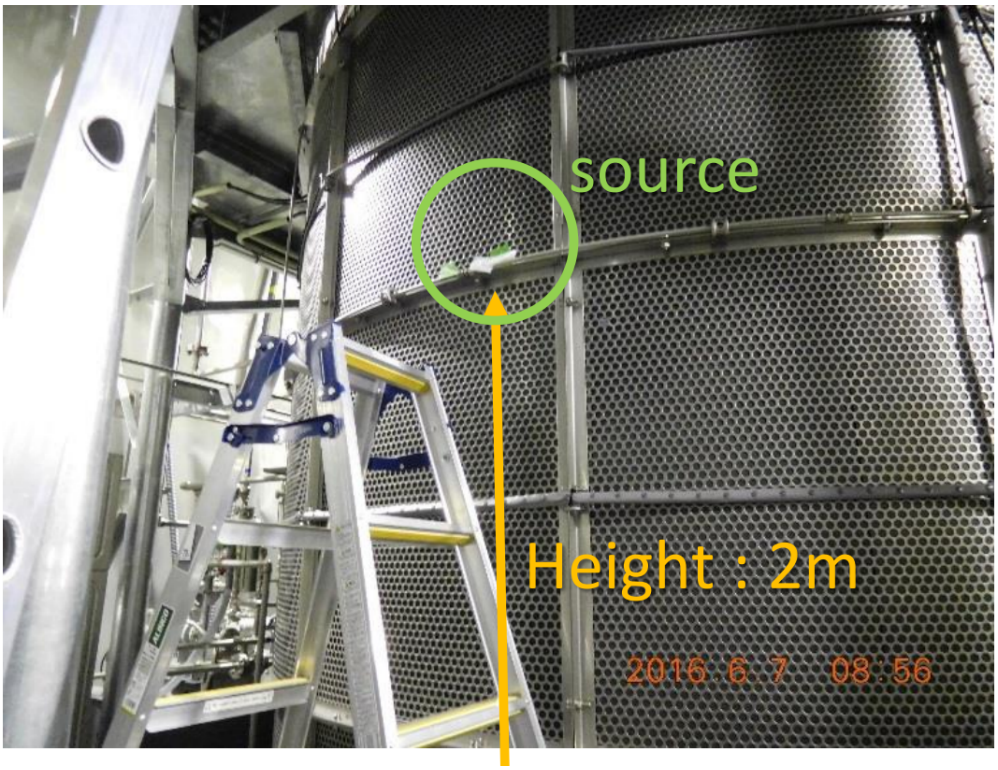

Figure 9.3.: Experimental setup for the "Tank" run in Run009. Like in Run008 and Run007, the source is directly attached to the shield at a height of 2 m in the south of the detector.

problem. However, 5 cm of lead can also shield neutrons. The effect of the 5 cm lead on neutrons is expected to be minor though. As the spatial distribution of emitted neutrons is assumed to be uniformly, it can already be guessed that the "Tank" runs contain a significant amount of rock (n,γ) events. This has to be taken into account in any analysis.

For the Run009 "Rock" run, the setup is more sophisticated, as shown in figure 9.4.

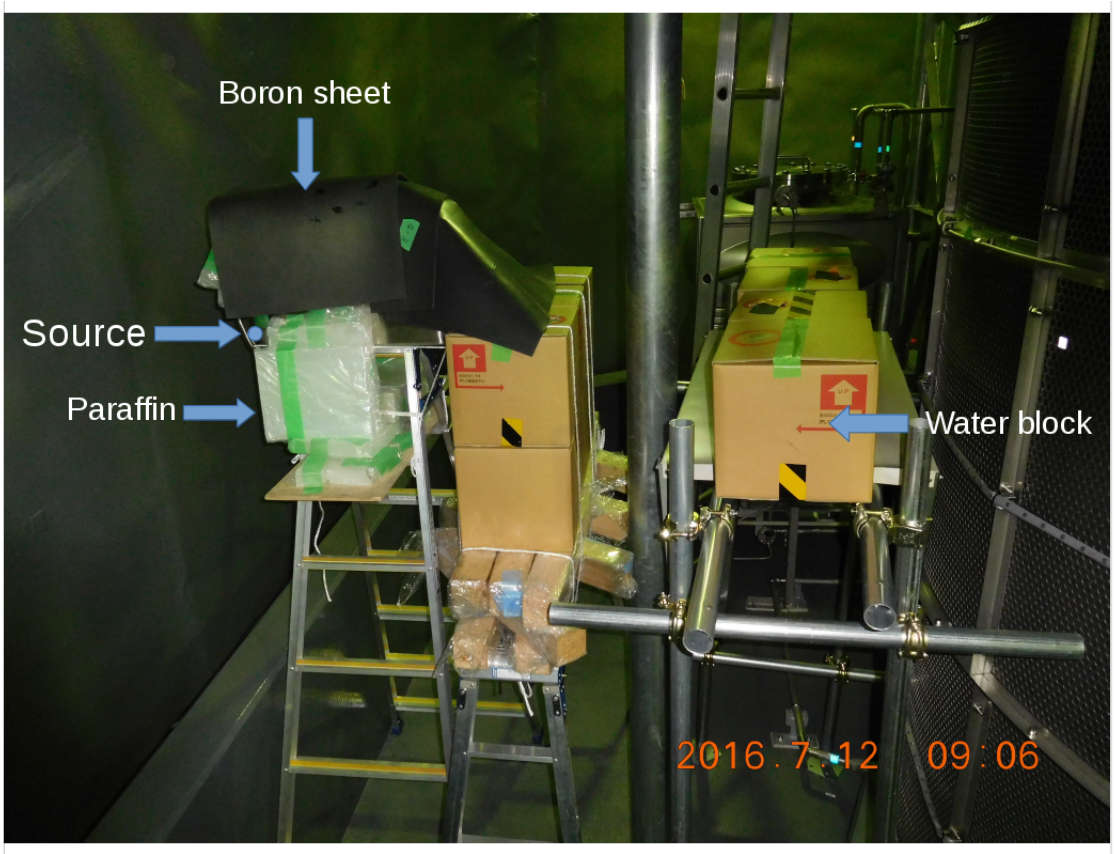

Figure 9.4.: Experimental setup for the "Rock" run in Run009. Like in Run008 and Run007, the source is put in front of the southern rock at a height of 2 m. An additional neutron shield is required due to the adjacent XMASS experiment.

In this case, the ^{252}Cf source was put at the same position as in Run007 and Run008 for about 45 hours. This time however (Run009), additional neutron shielding was required due to the new XMASS experiment which is being operated next to the CANDLES experimental cave. XMASS is a dark matter experiment in which free neutrons pose a serious background. Thus, the ^{252}Cf neutron emissions have to be limited in order to not disturb the XMASS experiment too much. For this purpose, multiple layers of neutron shielding (paraffin wax, boron sheet, water boxes) were put around the neutron source, except for the line of sight from the source to the rock (cf. figure 9.4). In Run007, only a 5 cm lead block was again placed in between the neutron source and the detector.

This poses a serious problem, as the measurements for Run007 employ no additional, improvised neutron shield. Due to this fact, the number of neutrons per fission that are captured in the rock will differ for Run009 and Run007 and the magnitude of this effect is hard to estimate. The same applies to the number of accidental tank (n,γ) events in "Rock" runs, as for Run009 significant neutron shielding is located in between the Californium source and the tank (on top of the 5 cm lead block). This issue will be reviewed later on.

9.1.1. Data selection and cuts

Similar to the investigations on the energy scale and event rate stability in chapter 8, data cuts have to be made. In this analysis, we want to estimate the reduction of (n,γ) events in the context of the search for neutrinoless double beta decay. Thus, the cuts for this analysis should be similar to those used in the actual search for 0νββ, which is looking for β signatures (electrons) that are contained in the crystals. The cuts that were used for the ^{252}Cf data analysis is as follows:

- DataQuality[0,1,2,3] = 0 in order to remove noise events
- (TriggerCounter33|TriggerCounter36)&0x4)! = 0. This rejects liquid scintillator events (LS) based on the dual gate trigger system (DGT) with high efficiency. CaF_2 + LS events with small deposit in the LS are not rejected though.
- CrystalN[0] != 0. Events within 3σ of the Gaussian distributions are selected. The positions of reconstructed events (in the used energy region) with a 3σ selection are well contained inside the CaF_2 crystals. The reconstructed position though is only the weighted mean of the spatial distribution of light. As a result, CaF_2 + LS events with a small LS deposit are not rejected, because their weighted mean is still inside the crystal.
- PSDPara4 (χ^2_β) cut for selecting beta (and accidentally $\beta + \gamma$) events. This means that most α events are rejected. On top of this, CaF_2 events can be discriminated from most CaF_2 + LS events. The actual cut values will be discussed in the appropriate section.

Unfortunately, the PSDPara4 parameter has not been available in the beginning of this study. Thus, another cut has been used in order to reject most CaF_2 + LS (e.g. $\beta + \gamma$) events with small LS deposit that survived the other cuts:

- 0.1 < Ratio4us < 0.2. The Ratio4us value for an event is calculated as the integrated 200ns ADC-charge divided by the total 4µs ADC-charge (Ratio4us = ADCTotal200ns/ADCTotal4µs). The purpose of this cut is to reject CaF_2 + LS events with small LS deposit, that would have normally been cut by the χ^2_β cut.

As such, we will present a ^{252}Cf analysis individually for both cuts (Ratio4us and χ^2_β). The primary goal of this analysis is to estimate the reduction on the number of events in the high-energy region based on data with a shield (Run009) and without a shield (Run007, Run008). The data that has been used in the following analysis can be found in table 9.1.

Run (Date)	SubRun	Type of ^{252}Cf run	Livetime
009 (11. & 12.07.2016)	62 to 66	**Rock** run	44h 35m 58s
009 (11.07.2016)	28	**Tank** run	3h 59m 28s
008 (04.12.2014)	61	**Tank** run	8h 17m 17s
007 (31.08.2014)	56	**Rock** run	11h 16m 07s
007 (31.08.2014)	54	**Tank** run	5h 48m 40s

Table 9.1.: Used data for the ^{252}Cf (n,γ) analysis. Run009 data has been taken after the shield construction while Run007 and Run008 data has been taken without a shield.

9.1.2. Study with Ratio cut

In this chapter, the results of the (n,γ) analysis with the Ratio4us cut will be presented. For this purpose, the Ratio4us cut values have to be chosen first. For Run007, other analysis shows that

$0.1 <$ Ratio4us < 0.2 is a reasonable Ratio4us range if one wants to reject CaF_2 + LS events efficiently. The same cut range is used in the search for $0\nu\beta\beta$, when the χ^2_β cut for a new Run is either not available or error-prone. The Ratio4us cut is based on the different decay constant of CaF_2 and LS, which is also exploited in the dual gate trigger. Thus, if the background and the experimental conditions don't change, the Ratio4us distribution should also not change. Based on the Ratio4us distributions for both "Rock" and "Tank" runs that are shown in figure 9.5, one can see that the distributions for each run changed significantly.

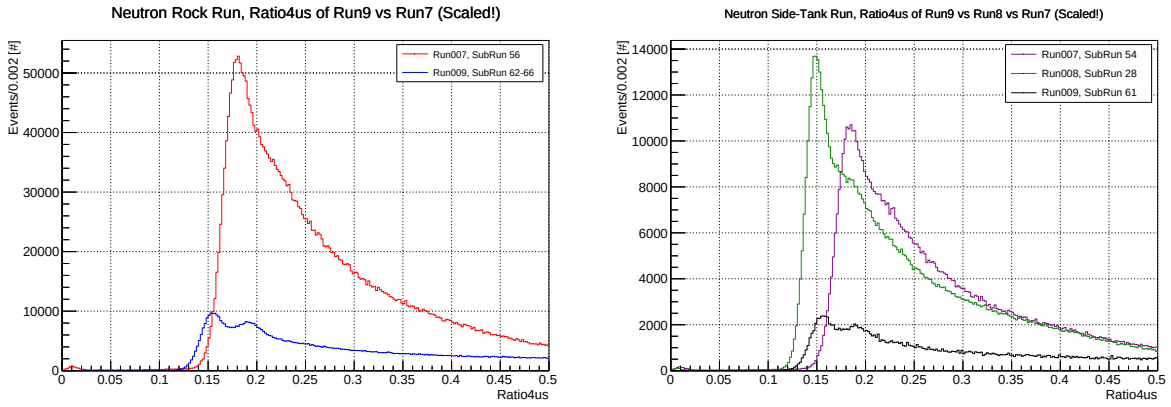

(a) Rock (b) Tank

Figure 9.5.: Ratio4us distributions for the ^{252}Cf "Rock" and "Tank" runs after the DataQuality, DGT and CrystalN cut. The distributions have been scaled in order to account for the different measurement times. For the "Rock" runs, Run007 is displayed in red, while Run009 is displayed in blue. For the "Tank" runs, Run007 is displayed in purple, Run008 in green and Run009 in black. It can be seen that the distributions for each Run are shifted in the X-axis. For the chosen Ratio4us range, only CaF_2 (peak) and CaF_2 + LS (tail) events are included. If one disables all previous cuts like the DGT, a second (LS only) peak would arise with a Ratio4us value larger than 1.

The shift in the X-axis is based on a different environmental temperature during the data taking. In Run007, the temperature was about 20 °C, as the cooling system had not been installed yet. On the other hand side, Run008 was performed with an active cooling system such that 4.2 °C could be reached. It is known that the decay constant of CaF2 crystals varies dependent on the temperature. For the LS however, it has not been studied yet. Nevertheless, this can still explain the shift in the Ratio4us distribution of Run007 compared to Run008. In Run009, only temperatures of 5 °C in CaF_2 can be reached, due to the new detector shield. Thus, a similar shift exists, though its magnitude to Run007 is smaller. In order to cut with the same efficiency for each Run, the Ratio4us distributions of Run007, Run008 and Run009 have to be aligned. For this purpose, the peaks are fit with a Gauss function and then the Run008 and Run009 spectra are shifted to the Run007 peak. Then, one can apply the same cut for all runs, based on the cut values of Run007. The result of this procedure is shown in figure 9.6.

However, it can also be seen that the Ratio4us distribution for Run009 has a second small peak. To date, it is not known in the collaboration why the shape of the Ratio4us distribution has changed for the new run. The basic difference of Run008 and Run009 is a small temperature change, the new detector shield and a completely new DAQ system. Unfortunately, the Ratio4us cut is directly related to the remaining number of events that will be used for the later estimation of the reduction factor. Thus, a Ratio4us cut with different Ratio4us shapes for data with (Run009) and without (Run007, Run008) a detector shield will induce a significant error on the final reduction factors for "Rock" and "Tank". For the χ^2_β cut, no difference in the shape of the

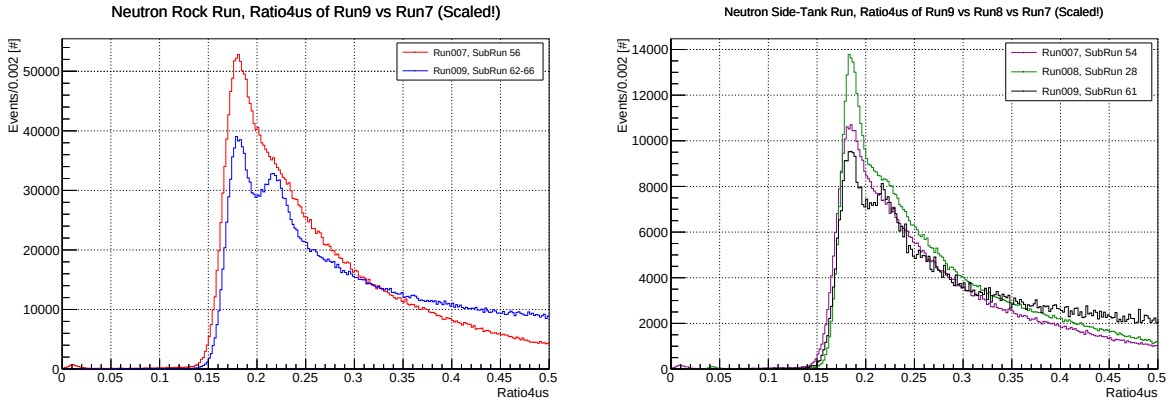

(a) Rock (b) Tank

Figure 9.6.: Ratio4us distributions for the ^{252}Cf "Rock" and "Tank" runs with adjusted peak positions. The distributions have been scaled in order to account for the different measurement times. Additionally, the spectra for Run009 have been scaled x4 for better visibility. For the "Rock" runs, Run007 is displayed in red, while Run009 is displayed in blue. For the "Tank" runs, Run007 is displayed in purple, Run008 in green and Run009 in black. One can see that the spectra of Run009 have a second peak that cannot be seen in the Run007 or Run008 spectra.

distributions of Run007, Run008 and Run009 can be seen. As a result, one can expect that it is more reasonable to use the χ^2_β cut.

After finalizing all of the data cuts, one would like to compare the energy histograms of the data with and without the detector shield for both "Rock" and "Tank" runs. Before this can be done, it needs to be kept in mind that the Californium-252 source has a half-life of 2.645 years. Data for Run007 and Run008 was taken in 2014, while the data for Run009 was taken in 2016. Thus, the different activity for each run needs to be taken into account. Now, one could simply scale the energy histograms of all runs in order to generate same-activity data. However, not all measured high-energy events are caused by the ^{252}Cf neutron source, as the natural (n,γ) background still exists. In this case, only a fraction of the data should be scaled.

For this purpose, the Physics energy spectra of Run007, Run008 and Run009 with the same cuts can be used. They can be seen in figure 9.7.

The first step is to scale each physics spectrum with respect to the measurement time of the related ^{252}Cf source runs. Then, the downscaled physics spectrum can be subtracted from the ^{252}Cf source spectrum. Subsequently, one can scale the remaining spectrum in order to extrapolate same-activity data for the different runs (7,8,9). Afterwards, the physics energy spectrum is added again. As a result, the diminishing activity of the ^{252}Cf source can be incorporated precisely.

Other than that, the Physics run energy spectra can also be used to verify the validity of the used cuts and to estimate differences of the runs in general. In example, it can be seen that the spectra for Run007 and Run008 agree very well in the Potassium-40 and Thallium-208 region. This is what one expects, due to similar experimental conditions. Additionally, it suggests that the cut efficiencies (e.g. the Ratio4us cut efficiency) for Run007 and Run008 are comparable. The same applies to the energy region of about 4 MeV to 5 MeV, which is nearly the same for all runs. This can be explained by the fact that the events in this energy region are mostly based on internal ^{208}Tl $\beta + \gamma$ background events. Thus, the event rate should not change significantly between Run007, Run008 and Run009. As such, the difference in the cut efficiencies for Run007 and Run008 compared to Run009 may not be that large, even though the Ratio4us distribution of

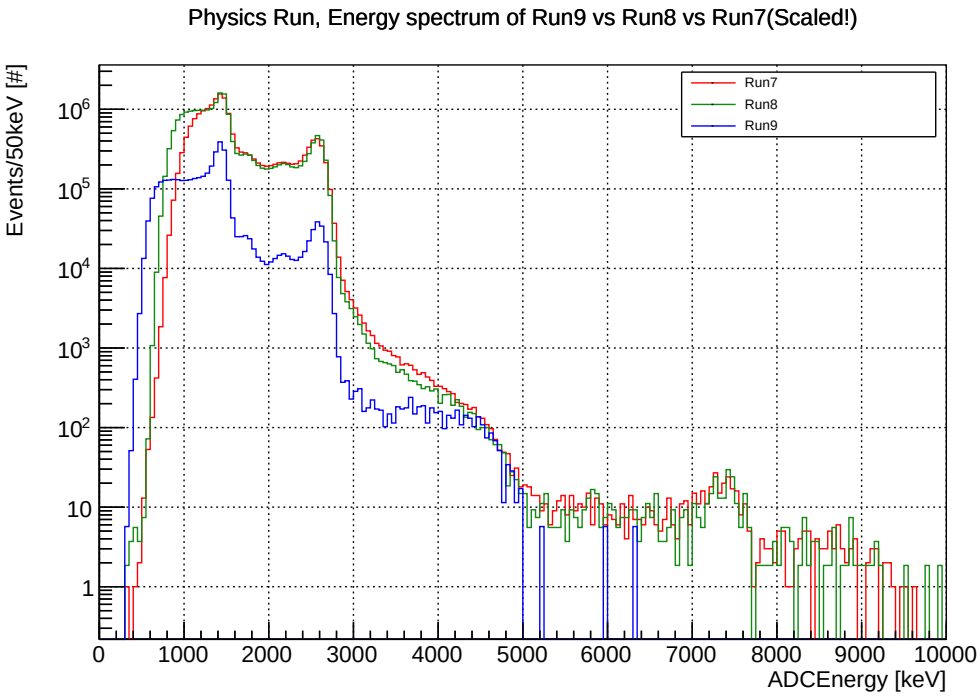

Figure 9.7.: Total Physics run energy spectrum of Run007 (red), Run008 (green) and Run009 (blue). For a better comparison, the spectra are scaled according to their livetimes. It can be figured that the spectra for Run007 and Run008 agree well, due to the similar experimental conditions. Additionally, the reduction of (n,γ) events in Run009 can be seen directly based on the high energy region ($E > 5\,\mathrm{MeV}$).

Run009 has a second (cut) peak. Apart from that, the number of events in the 3 MeV to 4 MeV region for Run009 is significantly lower than the ones for Run007 and Run008. This is based on the change of Al sleeves and O-rings in the detector to more radiopure ones before the start of Run009.

At this point, the ^{252}Cf source run data of the different runs can be compared. The only step that is still left is to account for the different measurement times of each run. As such, the related energy spectra are scaled accordingly. Then, the energy spectra can be investigated separately for both "Rock" and "Tank". The energy spectra for the "Rock" runs are shown in figure 9.8.

Now, it is possible to roughly estimate the reduction on the number of events due to the additional detector shield in Run009. For this purpose, one needs to integrate both spectra in a certain energy region in order to derive a reduction factor. In this analysis, two separate energy regions are chosen: 5 MeV to 10 MeV and $Q_{\beta\beta} \pm 5\%$ (4055 keV to 4481 keV). In the first case, the only significant process that contributes events is (n,γ) background by neutron capture in the rock or (accidentally) the tank. Thus, this region can be used to accurately estimate the remaining amount of (n,γ) background. In the second case, the energy region is dominated by ^{208}Tl $\beta + \gamma$ events during Physics runs. This means that only the tails of the high-energy neutron capture peaks contribute events in this region in addition to the other lower-energy (n,γ) peaks (e.g. silicon). And even though a strong ^{252}Cf source is used in the "Rock" run, a small, non-negligible amount of ^{208}Tl background is still present in the $Q_{\beta\beta}$ region. Thus, the 5 MeV to 10 MeV energy region should be taken as more accurate. Nevertheless, the reduction in the Q-region may also be interesting for other analysis.

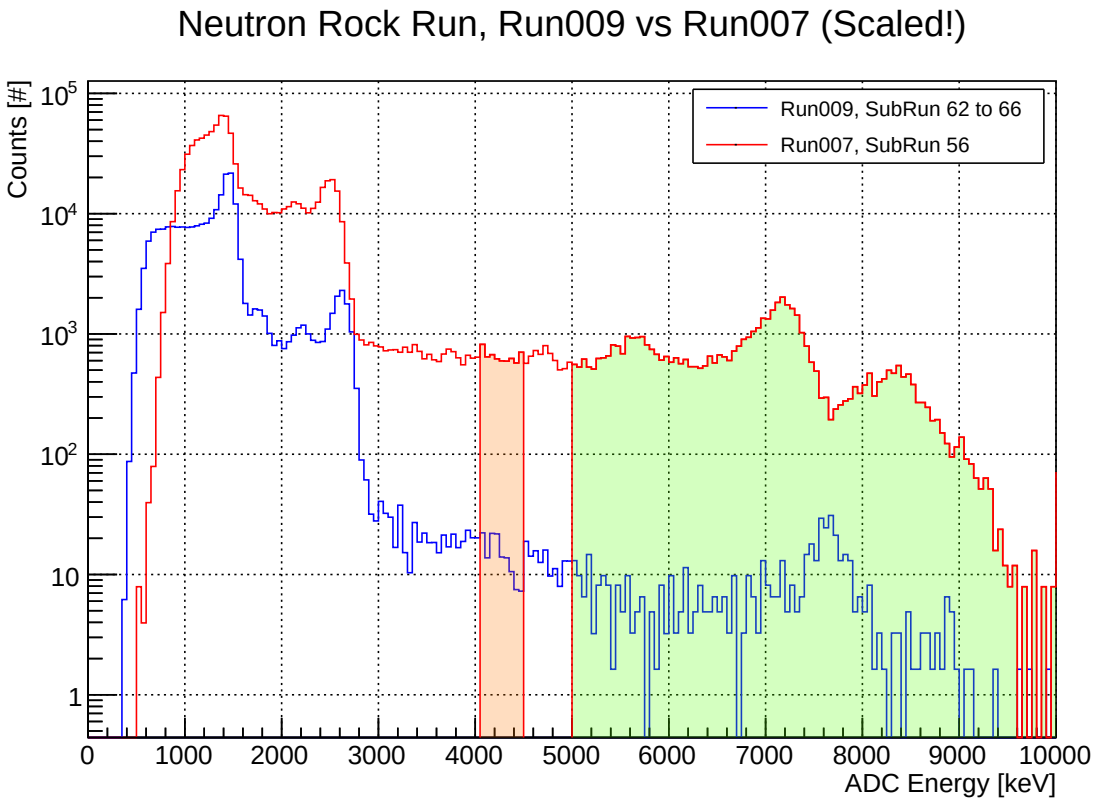

Figure 9.8.: ^{252}Cf "Rock" run spectra of Run007 (without shield, red) and Run009 (with shield, blue). These final spectra account for the Ratio4us shift, the different livetimes and the different ^{252}Cf activities. The reduction on the number of events (EventN-Run009/EventN-Run007) is about 1/90 in the region of 5 MeV to 10 MeV (shaded in green) and about 1/50 in the region of $Q_{\beta\beta} \pm 5\%$ (4055 keV to 4481 keV, shaded in orange). These values are directly calculated from data and not from the binned histograms.

At this point, the energy spectra are integrated individually based on the chosen energy regions. Then, one can derive a rough reduction factor as follows:

$$\text{Reduction}_{\text{Q/5to10}}(\text{"Rock"}) = \frac{\text{EventN}_{\text{R9, Q/5to10}}}{\text{EventN}_{\text{R8, Q/5to10}}}$$

The "Rock" reduction factor for the 5 MeV to 10 MeV region is about 1/90 and for the Q-region it is about 1/50. As we will show in the next section, the expected total reduction of rock (n,γ) events (5 MeV to 10 MeV) is about 1/350 based on simulations. However, the simulated reduction of rock (n,γ) events can not be compared directly to the reduction in the "Rock" ^{252}Cf runs. First and foremost, the ^{252}Cf "Rock" runs contain accidental tank (n,γ) events, whose reduction is expected to be worse ($\approx$ 1/40). Additionally, due to the different experimental conditions in the "Rock" runs of Run009 and Run007, an error is introduced. Principally, one could fit the recorded "Rock" energy spectra with simulated rock and tank (n,γ) spectra, in order to derive the ratio of both background types for the "Rock" run. This will be discussed later on again.
Secondly, it can be seen in figure 9.8, that the energy scales of Run007 and Run009 do not agree. In example, the 7.6 MeV iron neutron capture peak is shifted by about 400 keV. Based on figure 9.8, it seems that the shift scales linearly with energy. Thus, aligning the iron peaks would just be a rough solution. Third of all, the statistics of Run009 is low compared to Run007 and errors have not been estimated yet.

As a conclusion, this analysis result should be seen as a first guess in order to derive which analysis method should be pursued in the end: a ^{252}Cf data analysis with Ratio4us/Beta cut or an analysis based on the Physics run data.

Another error source is the choice of the Ratio4us cut region. As the shape of the Ratio4us distribution is significantly different for Run009 compared to the other two runs, choosing a different cut region could result in disparate reduction factors. Especially concerning is the second peak that can be seen in the Ratio4us distribution of Run009 at a value of about 0.22 (cf. figure 9.6). This source of error can be estimated by varying the upper cut limit of the Ratio4us cut (original upper cut value: 0.2) and calculating the reduction value each time. The result is shown in figure 9.9.

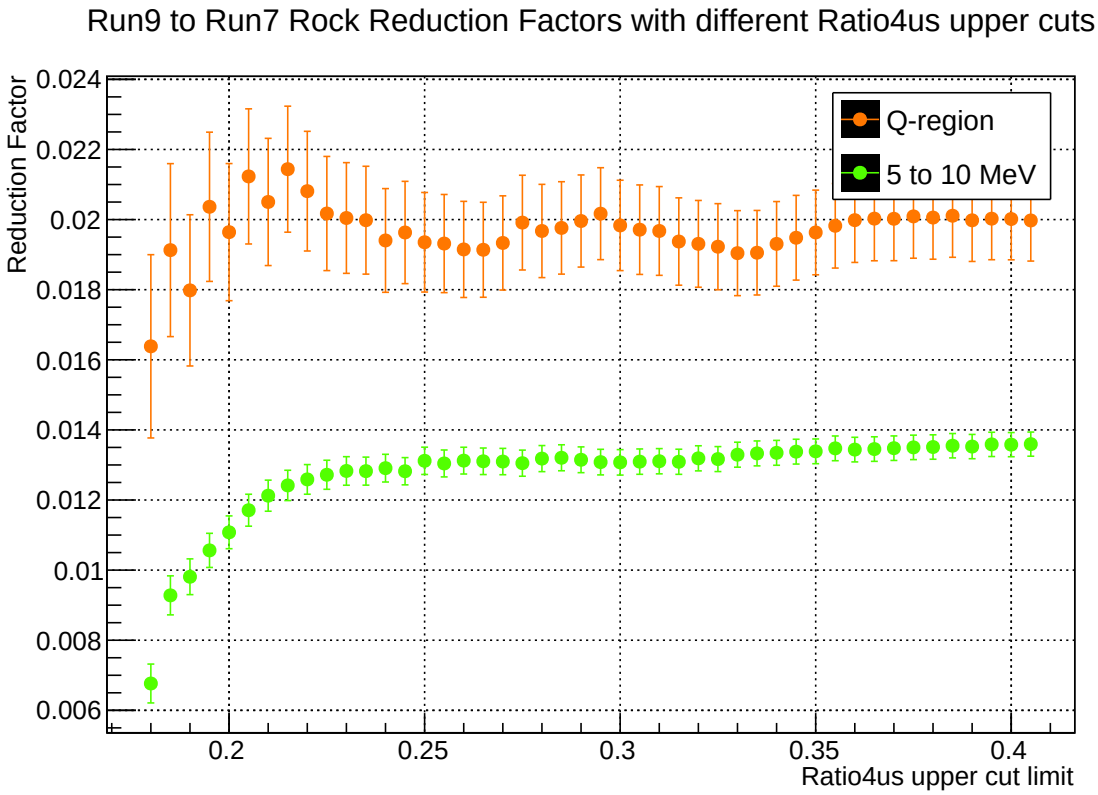

Figure 9.9.: ^{252}Cf "Rock" run reduction factors (EventN-Run009/EventN-Run007) based on different Ratio4us upper cuts. The reduction factors for the Q-region are shown in orange, while the reduction factors for the 5 MeV to 10 MeV region are shown in green. The error bars are calculated and propagated based on the assumed poisson statistics ($\sqrt{N}$). The errors for the 5 MeV to 10 MeV reduction factors are significantly smaller than the ones for the Q-region. This only indicates that in the latter case, the statistics are a lot lower.

It can be seen that the distribution of reduction factors is comparably stable after a Ratio4us upper cut limit of about 0.25. Yet, based on the high-energy region, it seems like the reduction get slightly worse with upper cuts larger than 0.3. The reason for this circumstance may very well be the different shape of the Ratio4us tail after a value of about 0.3, cf. figure 9.6. In particular, the tail of the Ratio4us distribution for Run009 does not diminish as fast as the tail for Run007. Especially for upper cuts below 0.2, a tendency to better reductions can be seen. The reason for this behavior is difficult to estimate, though it has to be noticed that the statistics in the reduction factor calculation gets low with these upper cuts.

If one sets the upper Ratio4us cut as 0.18, the remaining number of events for Run009 in the Q-region is 42 and in the high-energy region it is 94.
Consequently, the choice of the Ratio4us cut region has a significant effect on the derived reduction. Principally, the varying reduction could be explained by a different shield efficiency of CaF_2 only and CaF_2 + LS events. This is unlikely though, based on a physical standpoint. The alternative is an unequal Ratio4us cut efficiency for Run007 and Run009. A strong support for this argument lies in the appearance of a Ratio4us peak for Run009. This second peak has no physical justification, such that systematics have to be considered as the error source (e.g. due to the completely changed DAQ system).

All of these difficulties indicate that one should rather use the χ^2_β cut instead of the Ratio4us cut. Consequently, the analysis will be carried out again in the next section, but this time with a χ^2_β cut.

At last, the ^{252}Cf "Tank" runs can be investigated, cf. figure 9.10.

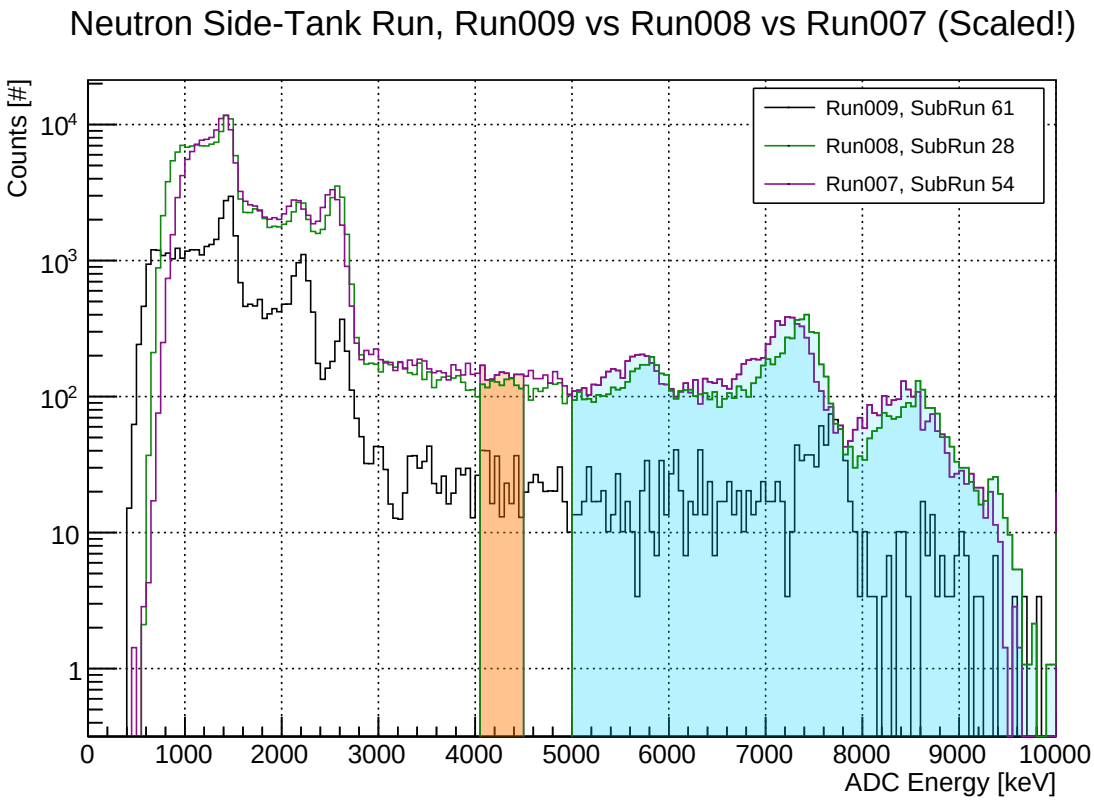

Figure 9.10.: ^{252}Cf "Tank" run spectra of Run007, Run008 (without shield, purple and green) and Run009 (with shield, black). These final spectra account for the Ratio4us shift, the different livetimes and the different ^{252}Cf activities. The reduction on the number of events for Run007 (Run008) to Run009 is about 1/7.5 (1/6.7) in the region of 5 MeV to 10 MeV and about 1/5.3 (1/4.7) in the region of $Q_{\beta\beta} \pm 5\%$.

It can be seen that there is a slight energy shift of Run007 and Run008 data, which would have to be accounted for in a more precise study. The "Tank" reduction factor in the high-energy region is about 1/7 and in the Q-region it is about 1/5. Simulated ^{252}Cf "Tank" spectra show a high-energy reduction of about 1/7 as well, which is in accordance with the rough experimental results. More insight on the simulation will be given in the next chapter.
Aside from all of the problems that were already discussed for the "Rock" run, an additional issue exists: the event rate in the ^{40}K and ^{208}Tl region of Run007 and Run008 does not agree very well.

As there were no fundamental changes between Run007 and Run008, the rate for both peaks should be the same in Run007 and Run008. Additionally, this discrepancy cannot be seen in the energy spectra of the Physics runs (cf. figure 9.7). Thus, this poses a serious problem, that has to be investigated further. In order to simplify the problem and eliminate possible bugs in the analysis code, the ^{252}Cf activity correction will not be applied for the next plots. This can be done without a problem, as the ^{252}Cf intensity in a source run does not effect the ^{40}K and ^{208}Tl intensity significantly anyways.

Keeping this in mind, a close-up of the low energy region from figure 9.10 can be found in figure 9.11. The energy shift in X-axis is not a huge concern, as this is only based on difficulties

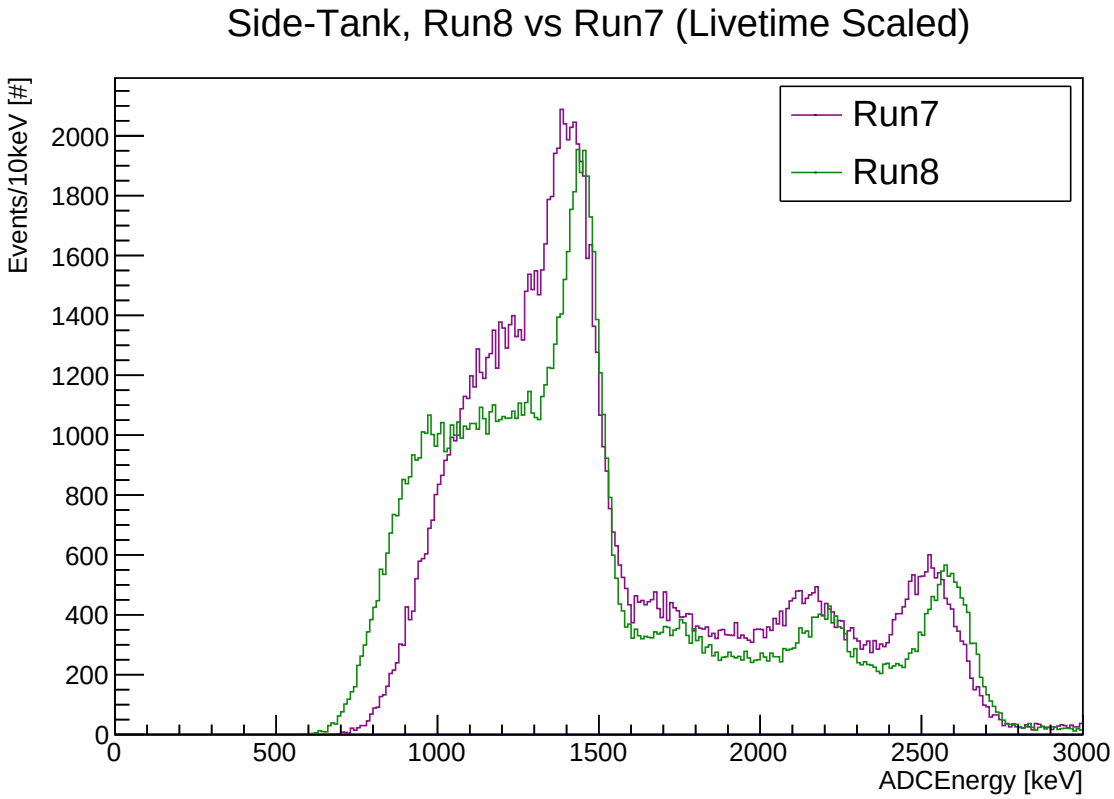

Figure 9.11.: ^{252}Cf "Tank" run spectra of Run007 and Run008 (without shield, purple and green). It can be seen that the spectra are shifted in energy. Additionally, it looks like Run008 has less events than Run007.

with the calibrations. However, if one adjusts the peaks for ^{40}K or ^{208}Tl (by Gauss fits), it can be seen that the number of events for both runs is not the same (cf. figure 9.12). For both the ^{40}K and the ^{208}Tl peak region, Run008 has about 20% less events than Run007. Now, one could think that this difference may be based on one of the other cuts. However, even after removing all of the other used cuts one-by-one, the difference can still be seen. Additionally, the Physics run spectra with the same used cuts don't show this discrepancy. Thus, it has to be assumed that the error is based on data and not on the analysis. Unfortunately, the measurements in Run007 and Run008 were done over two years ago and documentations about the source run of Run008 (e.g. photos of the experimental setup) could not be found. As a result, the issue cannot be resolved. This is one of the major reasons, why we will rather use the Physics run spectra for the final analysis later on.

At last and like in the analysis for the "Rock" run, the dependence of the reduction factors on the Ratio4us upper cut has been checked. The results can be found in subsection B.1.1.

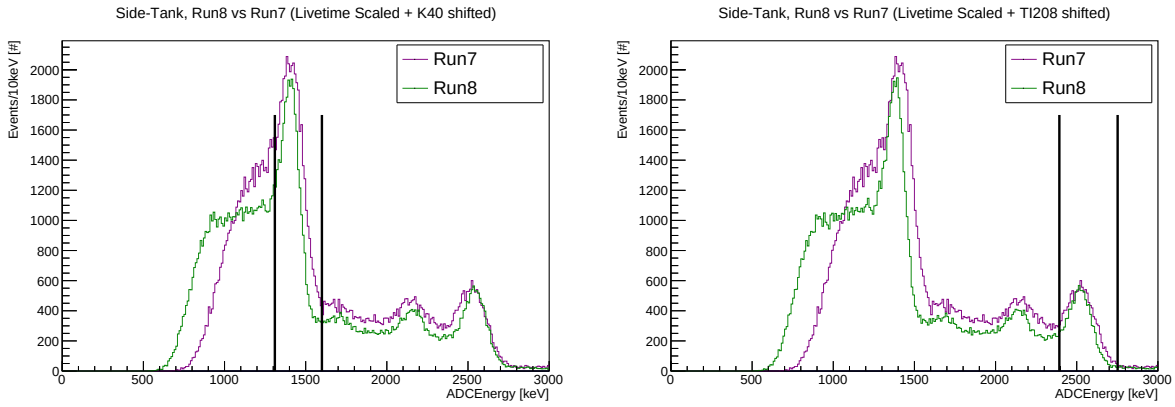

(a) ^{40}K peaks adjusted (b) ^{208}Tl peaks adjusted

Figure 9.12.: Low-energy ^{252}Cf "Tank" run spectra of Run007 and Run008. The spectrum of Run008 is shifted in order to adjust either the Potassium or the Thallium peak. Then, the spectra can be integrated within the energy region that is highlighted by the black bars. Run008 has about 20% events less than Run007 for both the ^{40}K and the ^{208}Tl peak region.

9.1.3. Study with Beta Cut

In this chapter, the results of the ^{252}Cf (n,γ) analysis based on a χ^2_β cut will be introduced. As such, the fundamental procedures will be the same as in subsection 9.1.2.
At first though, it has to be checked if the χ^2_β distribution changed for the different runs. For this purpose, one can investigate the χ^2_β values based on the reference pulse 2.6 MeV ^{208}Tl events (cf. section 7.3), that are known to be γ-rays. The related χ^2_β distributions are shown in figure 9.13.

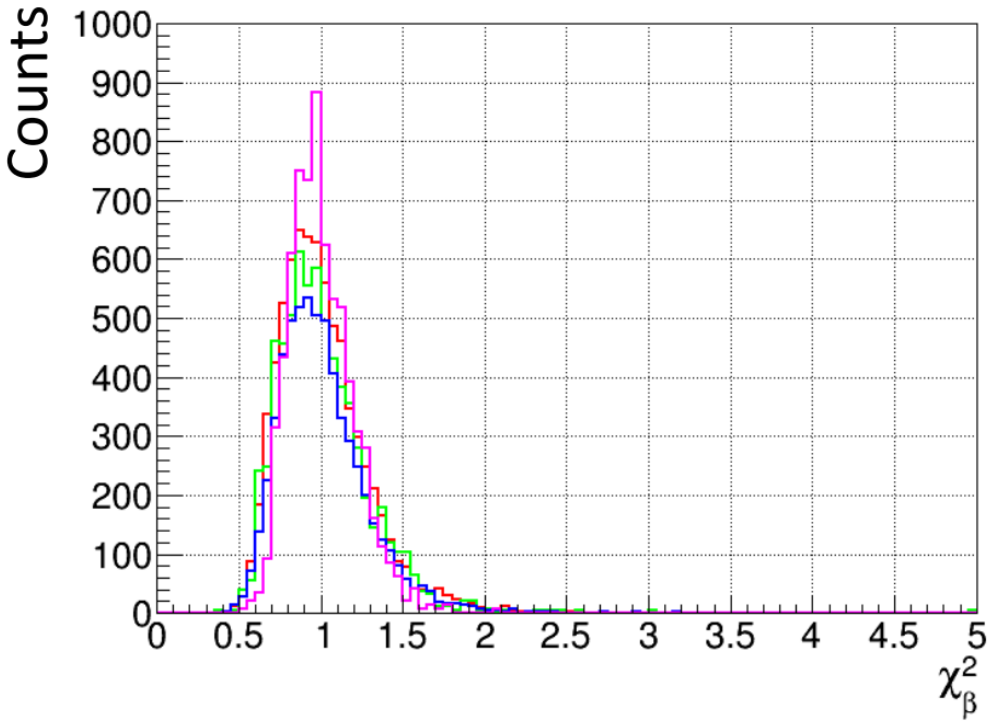

Figure 9.13.: χ^2_β distribution for Run007 (red, green), Run008 (blue) and Run009 (purple) based on ^{208}Tl reference pulses. The χ^2_β curves agree very well for the different runs. [47]

Hence, the χ^2_β distributions of β events (which includes electron and γ-ray signals) only show slight changes. Now, one can still try to account for these small differences. Principally, one would like to make a χ^2_β cut with the same **rejection** efficiency for all runs. Unfortunately, this is very difficult, as one would need to incorporate all other event types (e.g. β + LS(γ) or α) in such an analysis. A derivation of the rejection efficiency has not been done yet and would certainly be out of the scope of this thesis. Thus, it has been decided to try a same **detection** efficiency cut of β events. The detection efficiency can be easily calculated with aid of the distributions from figure 9.13 and the result can be found in figure 9.14.

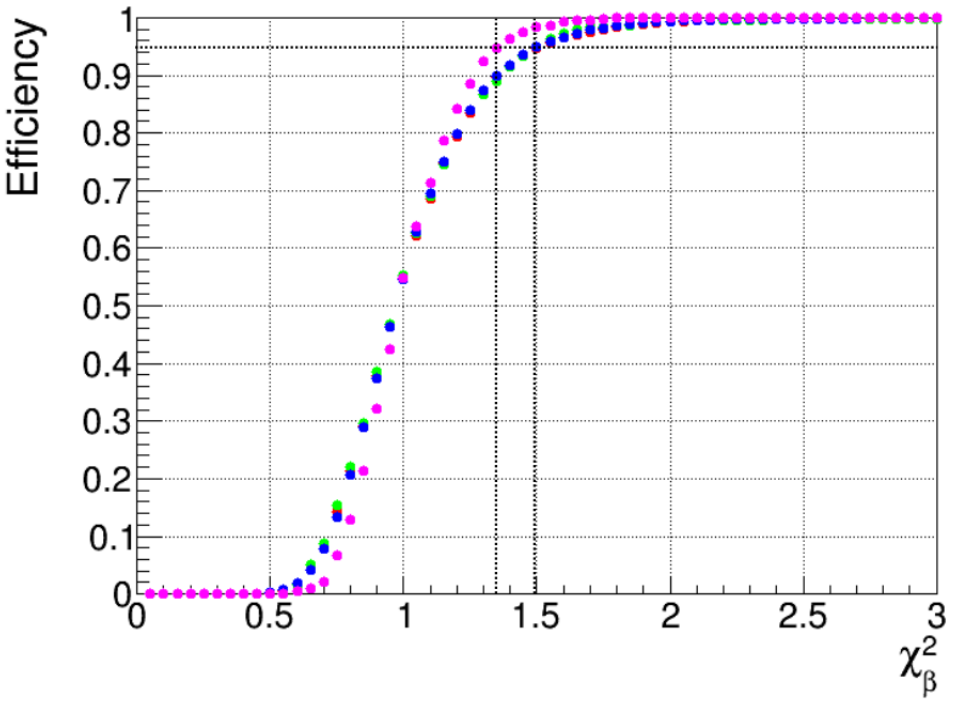

Figure 9.14.: Detection efficiency of β events for Run007(red, green), Run008 (blue) and Run009 (purple) based on ^{208}Tl reference pulses. The dotted lines mark the typically used χ^2_β cut value for Run007 and Run008 (1.5) and the corresponding cut for Run009 (1.35). The efficiency of these cuts is about 95%. [47]

Thus, the χ^2_β cut values have been chosen to be about 1.5 for Run007/Run008 and 1.35 for Run009. The validity of this cut technique can be estimated again by looking at the Physics run spectra, cf. figure 9.15. It can be seen that the spectra do not agree in the ^{208}Tl $\beta + LS$ (γ) energy region. Thus, it has to be assumed that at least the rejection efficiency for β + LS has changed over the runs. This poses a significant error source, as in the end, counts of one run are divided by counts of another one. Another solution to solve this problem will be shown in section 9.3.

At this point, the ^{252}Cf "Rock" and "Tank" source runs can be investigated again. The spectra for the "Rock" run with the χ^2_β cut are shown in figure 9.16. As expected, the problems that were already discussed in the Ratio4us analysis still exist (e.g. iron peak shift). Based on the high-energy region, the reduction for the χ^2_β and the Ratio4us analysis is the same (1/88 versus 1/90). For the Q-region though, the difference is significant (1/29 versus 1/50). This could be based on the different χ^2_β rejection efficiency of CaF_2 + LS events in this energy region (^{208}Tl). It is interesting though that the reductions for the high-energy region agree while the reductions for the Q-region don't agree. This could be a hint that the events in the high-energy region do not contain many CaF_2 + LS events. However, it has to be emphasized that the current stage of the analysis is only a rough one, such that a conclusion cannot be drawn.

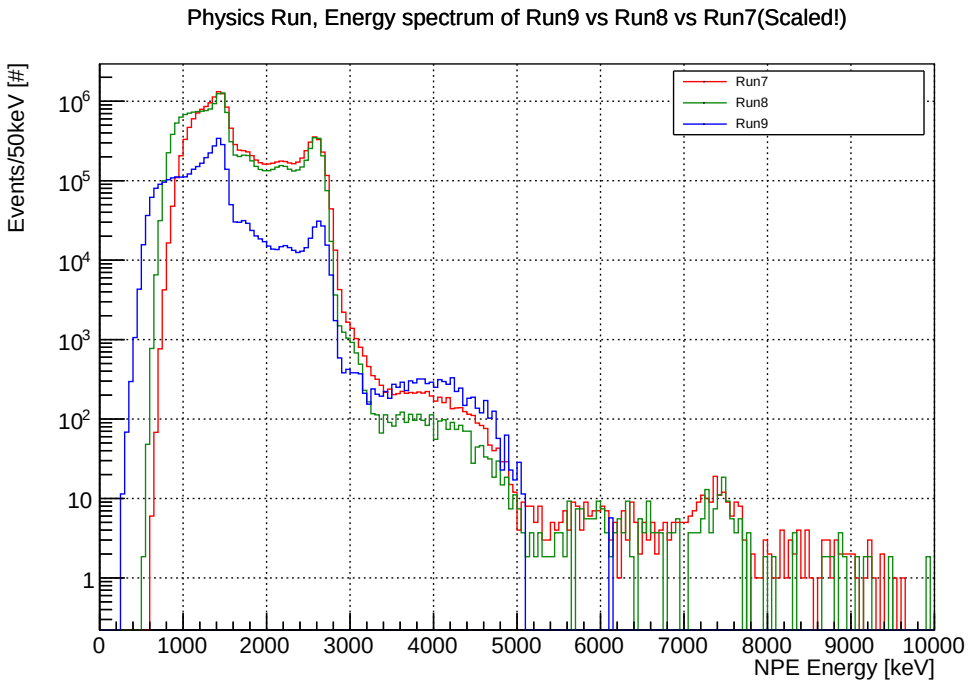

Figure 9.15.: Total Physics run energy spectrum of Run007 (red), Run008 (green) and Run009 (blue). The spectra are scaled according to their livetimes. The ^{208}Tl $\beta + \gamma$ energy region (about 3.4 MeV to 5 MeV) of the Runs shows a significant discrepancy.

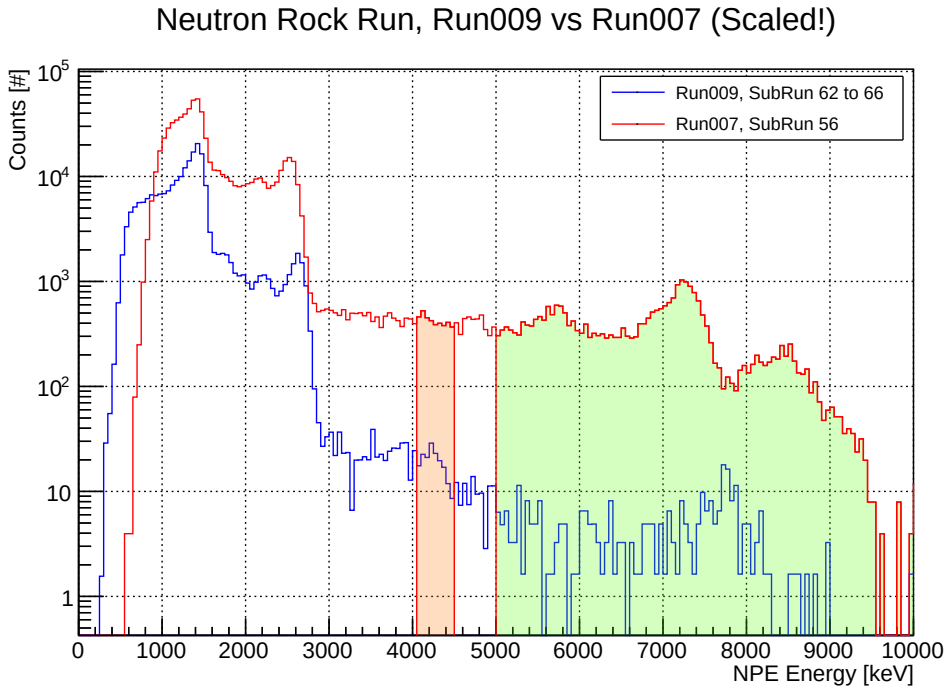

Figure 9.16.: ^{252}Cf "Rock" run spectra of Run007 (without shield, red) and Run009 (with shield, blue) with χ^2_β cut (same detection efficiency). These final spectra account for the Ratio4us shift, the different livetimes and the different ^{252}Cf activities. The reduction on the number of events is about 1/88 in the region of 5 MeV to 10 MeV and about 1/29 in the region of $Q_{\beta\beta} \pm 5\%$.

For more credibility, the "Tank" spectra can be investigated (cf. figure 9.17).

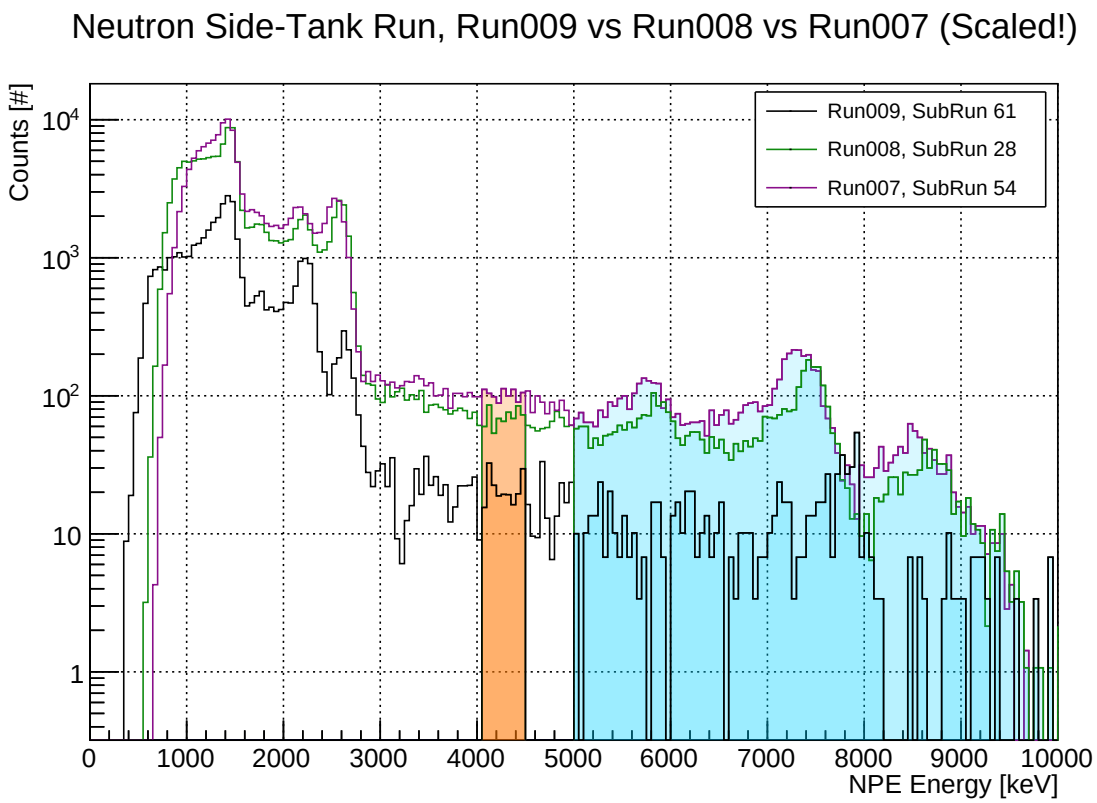

Figure 9.17.: ^{252}Cf "Tank" run spectra of Run007 and Run008 (without shield, purple and green) and Run009 (with shield, black) with χ^2_β cut (same detection efficiency). These final spectra account for the Ratio4us shift, the different livetimes and the different ^{252}Cf activities. The reduction on the number of events for Run007 (Run008) to Run009 is about 1/7.2 (1/5.1) in the region of 5 MeV to 10 MeV and about 1/4.8 (1/3.3) in the region of $Q_{\beta\beta} \pm 5\%$.

In this case though, both energy regions disagree a little bit compared to the Ratio4us analysis. For the high energy region, the χ^2_β reduction of Run007 (Run008) to Run009 is 1/7.2 (1/5.1) while it is 1/7.5 (1/6.7) for the Ratio4us analysis. The same applies to the Q-value region (1/4.8 and 1/3.3 versus 1/5.3 and 1/4.7). As such, the previous hypothesis is not supported. However, it has to be clearly mentioned that this is only a rough analysis so far (e.g. without errors). Thus, no well reasoned conclusions can be made.
As in the Ratio4us analysis, the dependence of the reduction factors on the choice of χ^2_β cut region can be checked. The results are shown in subsection B.1.2.

9.1.4. Conclusion

In this section, it has been demonstrated that the ^{252}Cf data analysis has several disadvantages. First and foremost, the issue of different event rates in Run007 and Run008 "Tank" spectra could not be resolved. This is a fundamental problem, as it has been demonstrated that the source of error is based on the data itself. Thus, at least one of the two spectra must be flawed. The impact of this problem on the final reduction factors cannot be estimated precisely. Secondly, one would need to remove the accidental tank (n,γ) events from the "Rock" runs and vice versa. Principally, the "Rock" and "Tank" data could be fit with simulated rock and tank (n,γ) spectra. The only problem is that the statistics for the Run009 ^{252}Cf source run data is very low, especially in the energy region where the tank and rock spectra are significantly different (> 8 MeV). At the same

time, longer measurement times are not feasible. The required statistics would result in a about ten times longer measurement, which translates to more than three weeks of 24/7 detector shift. This scenario is not realistic. Other than that, a new ^{252}Cf source with ten times the activity could be bought. Unfortunately though, we cannot use such a highly active source in the next time due to the adjacent XMASS experiment. As a result, the ratio of tank to rock events for both the "Rock" and "Tank" runs can't be estimated.
And even if all of these issues could be solved, the reductions would only be valid for one side of the detector, as a point-like source has been used. Since the detector shield is weaker at the top, the reduction factors in a 4π (e.g. Physics runs) source analysis would be different.
The final problem is due to the energy distribution of the neutrons. In example, the expected reduction of tank (n,γ) events is different for thermal and fast neutrons. This poses a problem, because the neutron energy distribution of the natural background can be very different. Thus, ^{252}Cf tank reductions are only valid for neutrons with an energy distribution of the Californium source.

Based on all of these issues, the Physics run spectra and thus the natural background spectrum will be used in order to derive the final reduction factors for both the rock and tank background. Its statistics may be even worse right now (126 days of livetime), but in principal one could just repeat the analysis in one or two years with more data.

9.2. Simulation of (n,γ) background

Before the (n,γ) Physics data analysis can be started, sensible rock and tank (n,γ) energy spectra need to be simulated. This is based on the issue that the high-energy (n,γ) background is caused by both types. Thus, the ratio of the rock to the tank background has to be derived in order to calculate reduction factors for both backgrounds.

9.2.1. Introduction to the CANDLES simulation and validity check

For this purpose, the already established CANDLES detector simulation (candles3_v03) can be used. The Monte Carlo simulation (MC) is based on the Geant4 toolkit (version 4.10.02.p02) and it already incorporates the new detector shield. The used geometry is shown in figure 9.18.

Principally, the whole (n,γ) neutron capture process for "Rock" and "Tank" can be simulated in Geant4. For this purpose though, one needs to validate the simulation. This is especially important for the γ-ray emission spectrum of the (n,γ) rock and tank reactions. Previous study shows that the γ-ray emission spectra for Fe and Pb neutron capture are totally off. In example, the Geant4 simulation overestimates the 7.6 MeV peak by almost 100% [48]. Thus, the γ-rays in the (n,γ) reaction are randomly generated based on database spectra and the physical Geant4 simulation of the γ-ray spectrum will not be used. Additionally, it has been found that the thermal neutron capture cross section is off for some elements. Except for H and Pb, Geant4 overestimates the cross section of each element that can be found in either the rock or the tank (C, Na, Mg, Al, Si, P, K, Ca, Ti, Cr, Mn, Fe, Ni). The cross section difference of the simulation compared to the data is about 30% for the rock and 20% for the tank [48].
At last, the effect of neutron thermalization (e.g. for polyethylene in the Boron shield) and thus the shielding effect is underestimated in Geant4. The resulting uncertainty is about 40%.

Fortunately, we are mostly interested in the simulation of an accurate (n,γ) spectrum in this analysis. And as the γ-ray spectrum of (n,γ) reactions does not depend on the neutron energy, the second and third issue can be neglected. Nevertheless, those errors have to be kept in mind, since the expected (n,γ) reduction (based on the simulations) will be calculated later on.

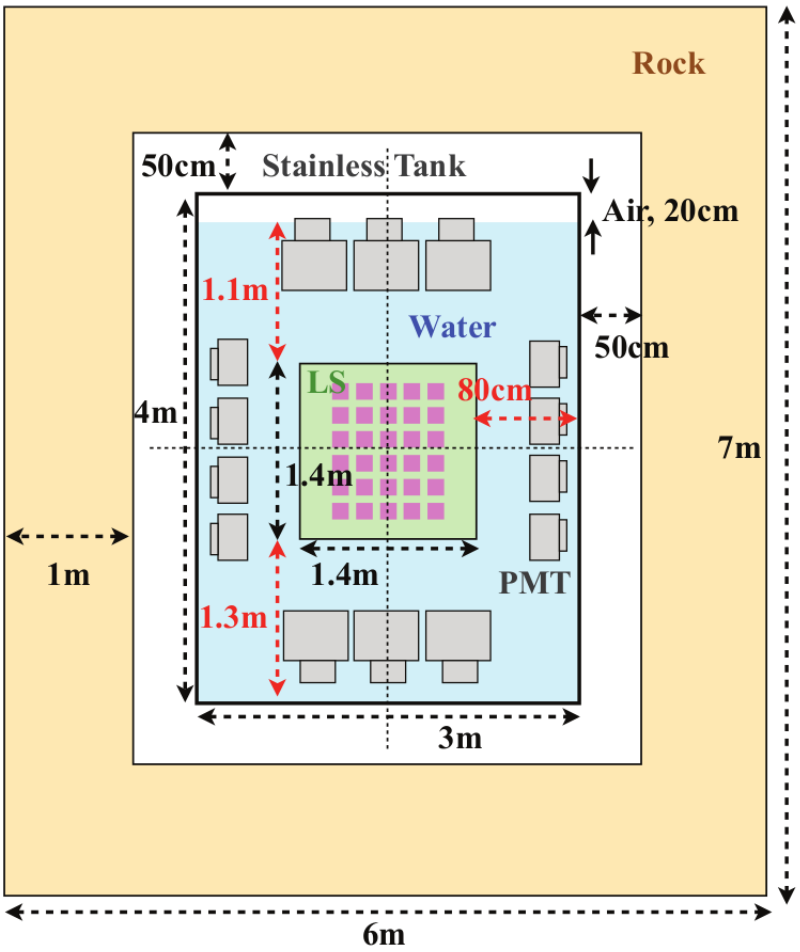

Figure 9.18.: Side view of the deployed simulation geometry. Though the detector shield is not shown, it is used in the Monte Carlo simulation. The rock, shield, tank and the LS are of cylindrical shape. [48]

9.2.2. Rock and Tank (n,γ) simulations

At this point, the rock and tank (n,γ) energy spectra can be simulated. For the later study, four different (n,γ) spectra are needed: one for each (n,γ) background type (rock, tank) with either enabled or disabled detector shield.
For the rock (n,γ) events, both cases (with/without the shield) can be simulated by generating (rock) γ-rays uniformly in the 1 m thick rock. Simulating the γ-rays only on the inner rock surface, in order to reduce the loss of photons and thus achieving less computation time, would result in an erroneous detected energy spectrum. Previous study shows that 1 m of rock is enough for the simulation of the γ-rays that pass through the rock.
The only issue is that one does not know the exact chemical composition of the rock around of the detector. Samples of the Kamioka mine have been analyzed, but they were not from the experimental cave (Lab C). However, two major types of rocks come into question: PRD74 [49] and RG45 [50]. Earlier analysis based on (n,γ) data from the experimental cave shows that RG45 should be used. Thus, the γ-rays will be generated based on this chemical rock composition.

For the tank γ-ray spectra, things are different because the tank is already inside of the detector shield. Additionally, it's desirable to derive a tank reduction factor only based on the simulation. Thus, neutrons are uniformly generated around the detector with aid of a simulated ^{252}Cf source.

Then, when neutrons are captured in the tank, the (n,γ) tank γ-rays are randomly generated based on a data spectrum for the stainless steel tank (SUS304). Additionally, the rock around the detector is removed from the geometry, in order to not create any rock γ-rays.

After the (n,γ) γ-rays have been generated, the deposited energy in CaF_2 + LS is calculated for each event. This may induce small errors later on when the reduction is calculated only based on the simulations. The reason is that the data cuts LS events, while the simulated data does not. However, the shield effect on γ-rays by the LS can be assumed as negligible due to its chemical composition and thickness. Additionally, it should be noticed that the readout of the PMTs and the creation of scintillating photons due to the γ-rays is not possible in the current CANDLES simulation. Hence, only the deposited energy in the CaF_2 + LS for the single events can be used in order to generate the rock and tank simulation (n,γ) energy spectra.

As a summary, the following simulations were performed:

Source (particle)	position	Shield?	N
Rock (γ)	rock	no	$1 \cdot 10^{10}$
Rock (γ)	rock	yes	$3 \cdot 10^{11}$
^{252}Cf (n)	outside	no	$1 \cdot 10^{8}$
^{252}Cf (n)	outside	yes	$1 \cdot 10^{9}$

Table 9.2.: List of performed simulations. N is the number of simulated events.

The total computation time needed for these simulations is about four weeks with 50 cores of Intel X5680 CPUs.

9.2.3. Expected background reduction based on simulations

Now, one can calculate the (n,γ) background reduction based on the simulations.
Both spectra for the (n,γ) rock background are shown in figure 9.19.

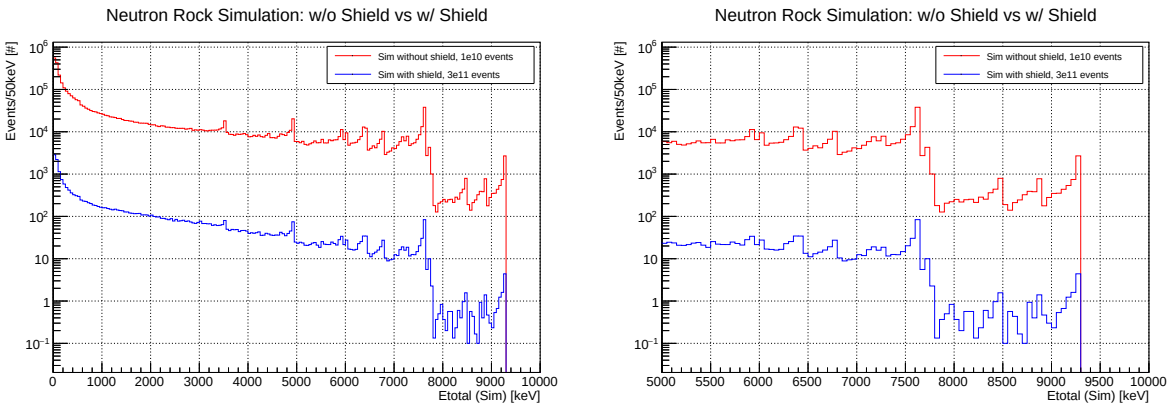

(a) Whole spectrum

(b) High-energy region

Figure 9.19.: Comparison of the simulated rock (n,γ) energy spectra with (blue) and without a shield (red). The spectrum with enabled shield has been scaled down in order to account for the different number of simulated events.

Then, the reduction factor can be calculated by integrating the number of events for each spectrum from 5.5 MeV to 10 MeV. Compared to the ^{252}Cf analysis, the lower edge was refined from 5 MeV

to 5.5 MeV. The reason is that the background for Run009 increases dramatically at around 5.5 MeV (and not 5 MeV) due to ^{208}Tl events.
As a result, the simulated reduction factor for (n,γ) rock events is about 1/350. This is roughly what one would expect from about 10 cm of lead (a few hundreds).

The same method can be applied for the simulated tank spectra, cf. figure 9.20.

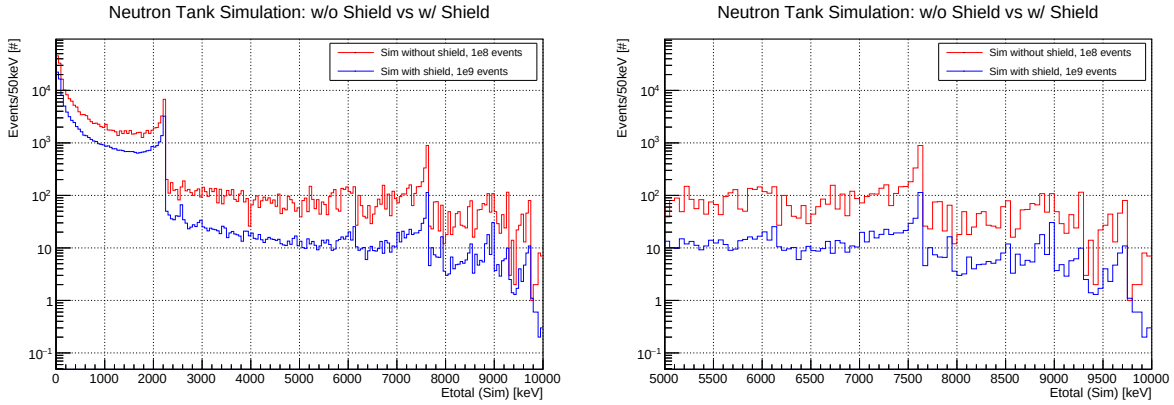

(a) Whole spectrum

(b) High-energy region

Figure 9.20.: Comparison of the simulated tank (n,γ) energy spectra with (blue) and without a shield (red). The spectrum with enabled shield has been scaled down in order to account for the different number of simulated events. The reduction that can be seen is only valid for the neutron energy distribution of a ^{252}Cf source.

This time however, the result is only valid for neutrons with a ^{252}Cf energy distribution, since the shield effectiveness depends on the neutron energies. The calculated reduction for (n,γ) tank events is about 1/7. For the natural (n,γ) background, previous studies show that the expected tank reduction is about 1/40.

9.2.4. Comparison of ^{252}Cf data to simulation

At last, the validity of the simulation can be checked by a comparison to the ^{252}Cf Run009 source run data. For this purpose, the position of the initially generated rock (γ) or tank (n) events needs to be changed to a point like source. For the tank events, the simulation source was set on the side surface of the detector shield at 2 m height, like in the experimental runs. In case of the rock events, the rock γ-rays cannot be simply generated at the same position as in the data. This is due to the fact, that the γ-ray spectrum can change while passing through the rock. In example, the γ-ray spectrum at the inner surface of the rock is different from the original one. As such, one would have to simulate the (n,γ) rock spectrum with a ^{252}Cf neutron source. This would require a large amount of computation time: $3 \cdot 10^{11}$ rock γ-rays had to be generated inside the rock for the previously simulated rock spectrum in order to achieve decent statistics (nearly three weeks of computation time). At the same time, the modeling of the experimental setup of the Run009 "Rock" run requires a larger effort due to the additional neutron shield that had to be employed (XMASS). On top of that, simulating neutrons takes more than 100 times the time compared to simulating γ-rays. Principally, methods could be developed to decrease the simulation time. However, it was not worth the time, since this comparison is only an additional verification. Thus, the comparison of ^{252}Cf data to the simulation has only been executed for the tank spectrum (cf. figure9.21).
It can be seen that the simulation and the data roughly agree. Unfortunately, the statistics of the data is too low for a precise comparison. This is especially true for the very high energy region above 8 MeV.

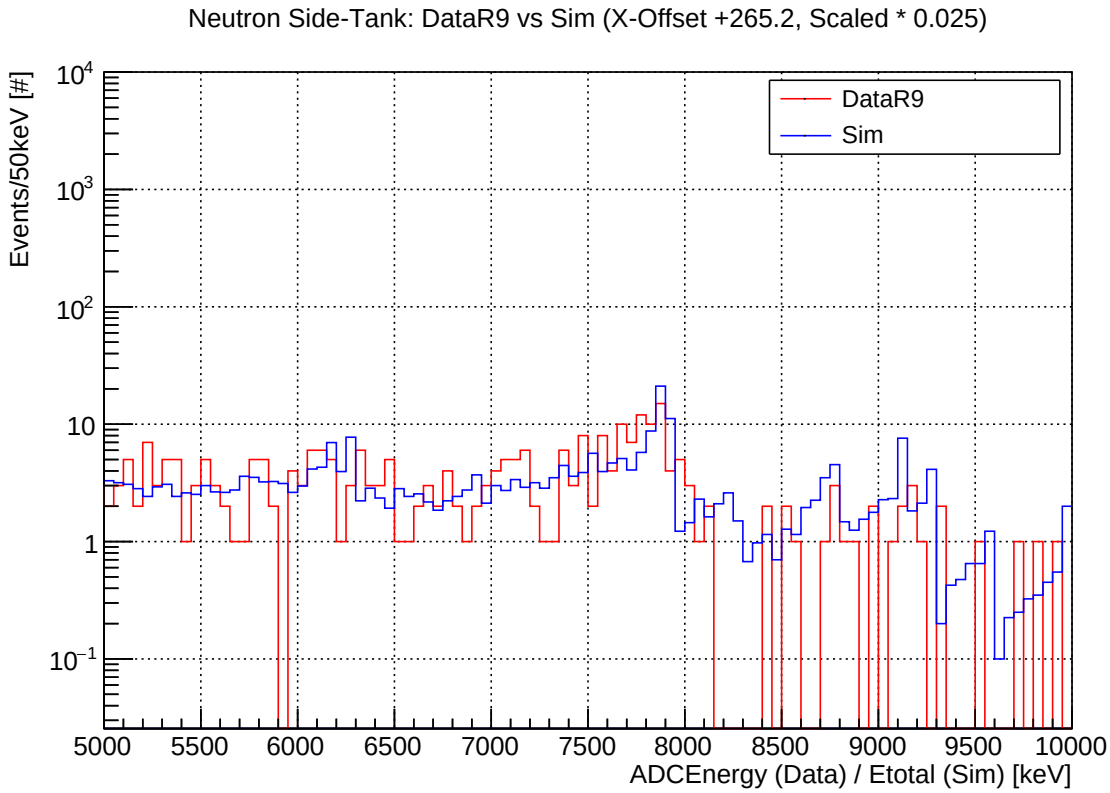

Figure 9.21.: Comparison of the ^{252}Cf "Tank" source run data (red) to the simulation (blue). The simulation is scaled down for a better comparison.

9.3. Analysis based on Physics Run data

Now that the simulated (n,γ) rock and tank energy spectra have been generated, the analysis based on the Physics run data can be started. The goal of this final analysis is to derive a reduction factor for both the rock and the tank (n,γ) background in the high-energy region.

9.3.1. Used data and cuts

For this purpose, the Physics run data of the current Run009 and the old Run008 can be used:

	Subruns	Livetime	Shield?
Run008	3 - 41	26.4 d	no
Run009	69 - 230	132.6 d	yes

Table 9.3.: Used data in the Physics run analysis. Both runs are cooled down to about 4 °C (Run008) and 5 °C (Run009). Thus, the decay constant of the CaF_2 crystals should not change much between both runs.

The cuts that are applied on these data are exactly the same as in the χ^2_β Californium-252 source run analysis (DGT, DataQuality, CrystalN-3σ). The only exception is a different beta cut which will be introduced now. This time, a more loose cut will be used ($\chi^2_\beta < 3$ for Run009), in order to get better statistics.

At first, one can investigate the χ^2_β distributions for Run008 and Run009, as shown in figure 9.22. Thus, the shape of both distributions is similar.

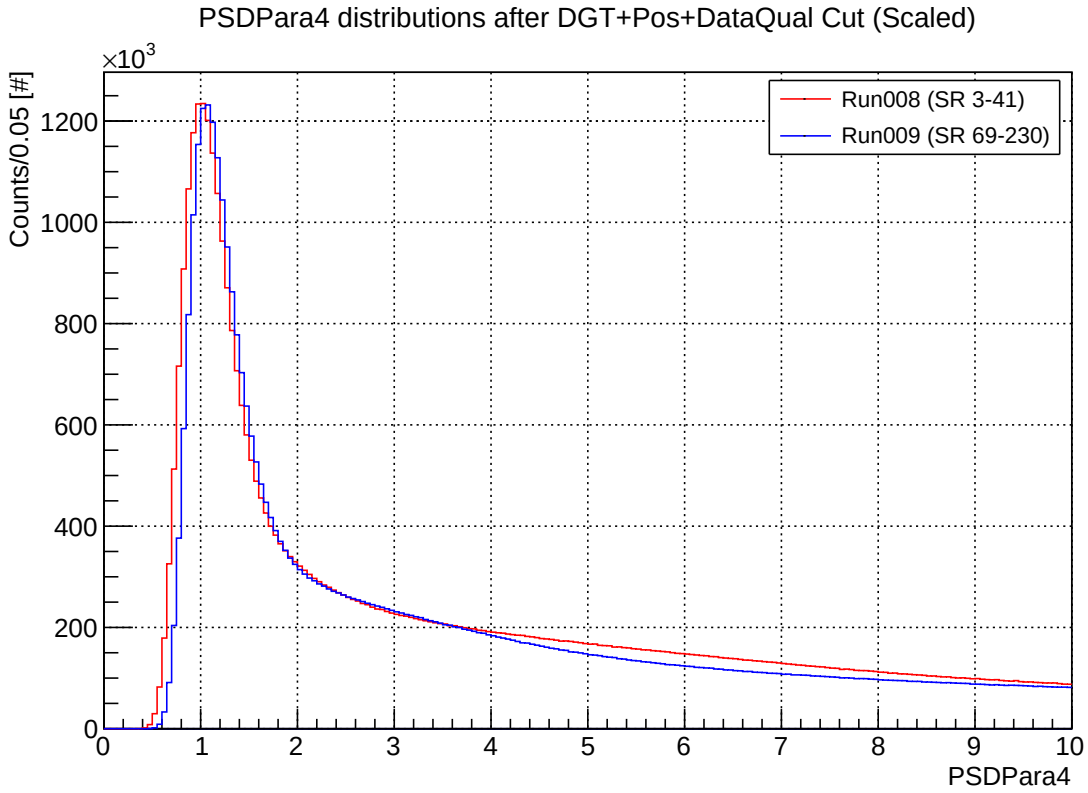

Figure 9.22.: χ^2_β distribution of Run008 and Run009 after the DGT, DataQual and CrystalN cuts. The curve of Run009 is scaled to the same peak height of Run008 for better comparability. The shape of both distributions agrees well, except for a minor difference after a value of about 4.

In the ^{252}Cf analysis, it could be seen that a same efficiency χ^2_β cut leads to a disagreement in the ^{208}Tl region if one compares Run008 and Run009 Physics run data. This time, more data from Run009 is available and a looser cut is applied. Accordingly, it is interesting to evaluate if this discrepancy still exists. The corresponding Physics run histograms of Run008 and Run009 can be found in figure 9.23. It shows that the ^{208}Tl $\beta + \gamma$ region still does not agree. This circumstance is based on the beta cut, since the spectra agree well with no χ^2_β cut (cf. figure 9.24). In this case, Run009 has practically the same ^{208}Tl $\beta + \gamma$ event rate as Run008. One would expect the same, as the ^{208}Tl $\beta + \gamma$ events are internal background that will not be reduced by the new detector shield. Consequently, the ^{208}Tl (β+γ) rate of Run009 should at least not be higher than in Run008.

It has already been discussed that this can be based on a different rejection efficiency for Run008 and Run009. Since α events can be cut very efficiently with the χ^2_β cut, it is reasonable to assume that the discrepancy is based on a different rejection efficiency for $\beta + \gamma$ ($CaF_2 + LS$) events. Consequently, one can collect known $\beta + \gamma$ events (internal background) for both Run008 and Run009 in order to derive a same rejection efficiency χ^2_β cut.
For this purpose, a sequential decay from the Uranium decay chain can be used:

$$^{214}\text{Bi} \xrightarrow{Q_{\beta+\gamma}=3.3\,\text{MeV}} {}^{214}\text{Po}\ (\text{T}_{1/2} = 164\,\mu\text{s}) \xrightarrow{Q_\alpha=7.8\,\text{MeV}} {}^{210}\text{Pb}$$

However, it should be noticed that not every ^{214}Bi $\beta + \gamma$ event deposits energy in the LS, even

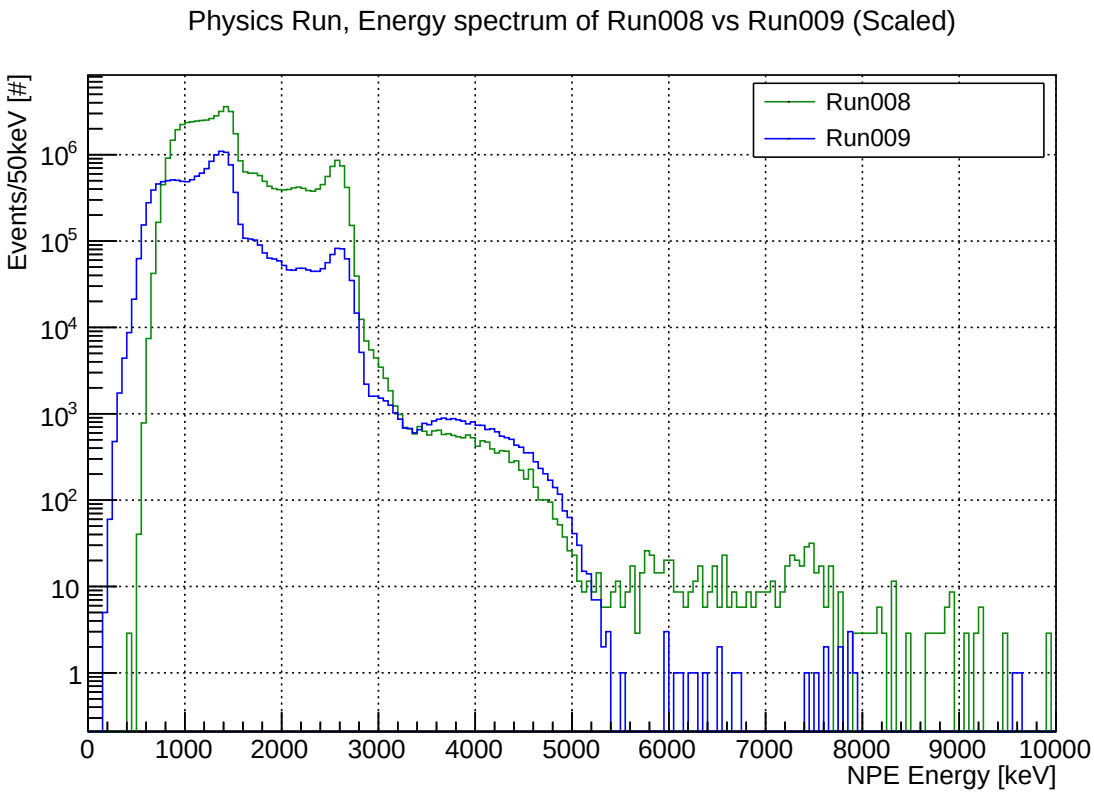

Figure 9.23.: Total Physics run energy spectra of Run008 (green) and Run009 (blue). The spectra are scaled according to their livetimes. For Run009 data, a $\chi^2_\beta < 3$ cut is applied. The cut for Run008 is made at the same detection efficiency (about $\chi^2_\beta < 4$). The gap in the ^{208}Tl $\beta + \gamma$ region (about 3.4 MeV to 5 MeV) can still be seen.

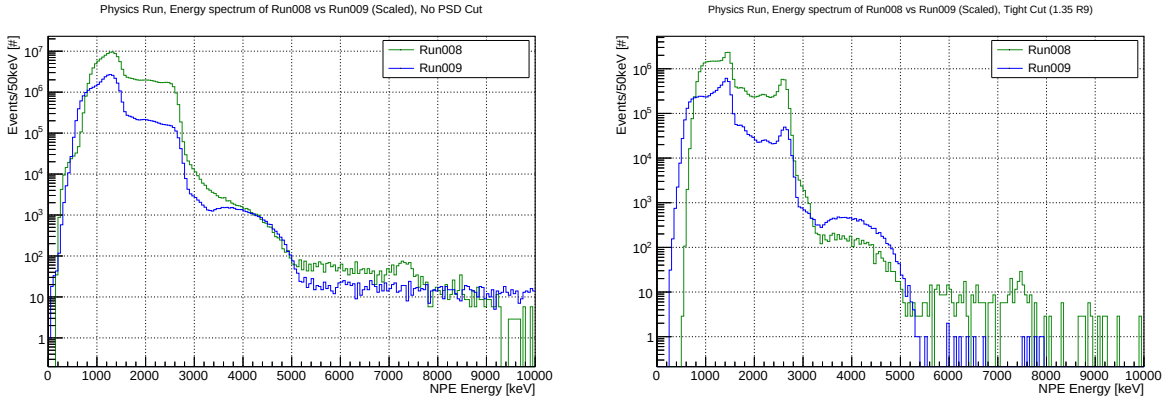

(a) No χ^2_β cut

(b) Tight χ^2_β cut ($\chi^2_\beta < 1.5$ for Run009)

Figure 9.24.: Total Physics run energy spectra of Run008 (green) and Run009 (blue). The spectra are livetime corrected. In the left figure, no χ^2_β cut is applied and the spectra agree well above 4 MeV. This demonstrates that the discrepancy in the ^{208}Tl $\beta + \gamma$ region is caused by the beta cut. In the right figure, a tighter beta cut is applied and the issue persists.

though it is likely. As a result, some collected ^{214}Bi events may only have deposited their energy in the crystals, which means that they are not $CaF_2 + LS$ events. Keeping this in mind, the prompt ^{214}Bi $\beta + \gamma$ events can be collected by applying a delayed coincidence method to the data

of Run008 and Run009. Due to the short half-life of Polonium-214, the accidental coincidence of this technique is very low. Thus, $\beta + \gamma$ events can be identified very efficiently. Figure 9.25 shows the time difference between the ^{214}Bi and ^{214}Po decay for each collected event.

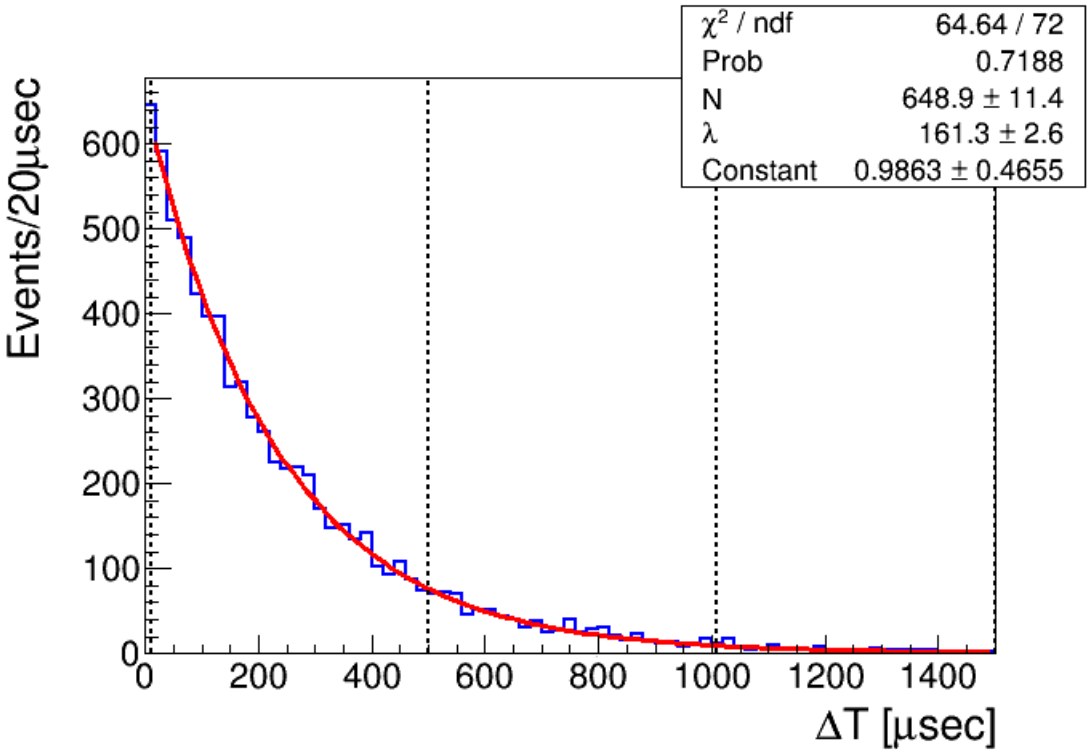

Figure 9.25.: Time differences (ΔT) between the prompt (^{214}Bi) and delayed (^{214}Po) events of ^{214}Bi candidates in Run009. The histogram is fit with an exponential function and the expected half-life is within the uncertainties of the derived half-life (λ). In the following analysis, events with $1\,\mu s < \Delta T < 500\,\mu s$ will be used.

After these ^{214}Bi $\beta + \gamma$ events have been collected for each run, a $\chi^2_\beta < 3$ cut can be applied on the data ^{214}Bi of Run009. Subsequently, the rejection efficiency of $\beta + \gamma$ events for Run009 can be calculated by investigating the remaining number of events compared to the total number of events. Then, the same method is applied to the Run008 ^{214}Bi data. This time though, various χ^2_β cuts are made in order to derive the χ^2_β cut value which yields the same rejection efficiency as in Run009. As a result, one gets the χ^2_β cut values of Run008 and Run009 for a same $(\beta+\gamma)$ rejection efficiency χ^2_β cut. At last, these cuts are applied on the Run008 and Run009 data, which is shown in figure 9.26. It can be seen that the same rejection efficiency cut reduces the discrepancy only by a little bit. However, the different energy scale of Run008 and Run009 has been neglected till now. If one aligns the Fe peaks of both histograms, the deviation gets considerably smaller (cf. figure 9.27). Nevertheless, aligning the iron peaks is only a rough solution, since the energy scale of Run008 is nonlinear by about $2\% - 3\%$. This fact can be seen in the figure (9.27) based on the peak positions of ^{40}K and ^{208}Tl for each run.

For the remaining discrepancy, it is known that the ^{208}Tl $(\beta + \gamma)$ event rate cannot have increased from Run008 to Run009. Consequently, the disagreement should be considered as a systematic error. One possible reason for the remaining discrepancy could be that the collected ^{214}Bi $\beta + \gamma$ data sample could possibly contain a significant amount of events that only deposit their energy in the CaF_2 crystal and not also in the LS. However, this is only a rough guess and thus, further analysis will be performed in the future.

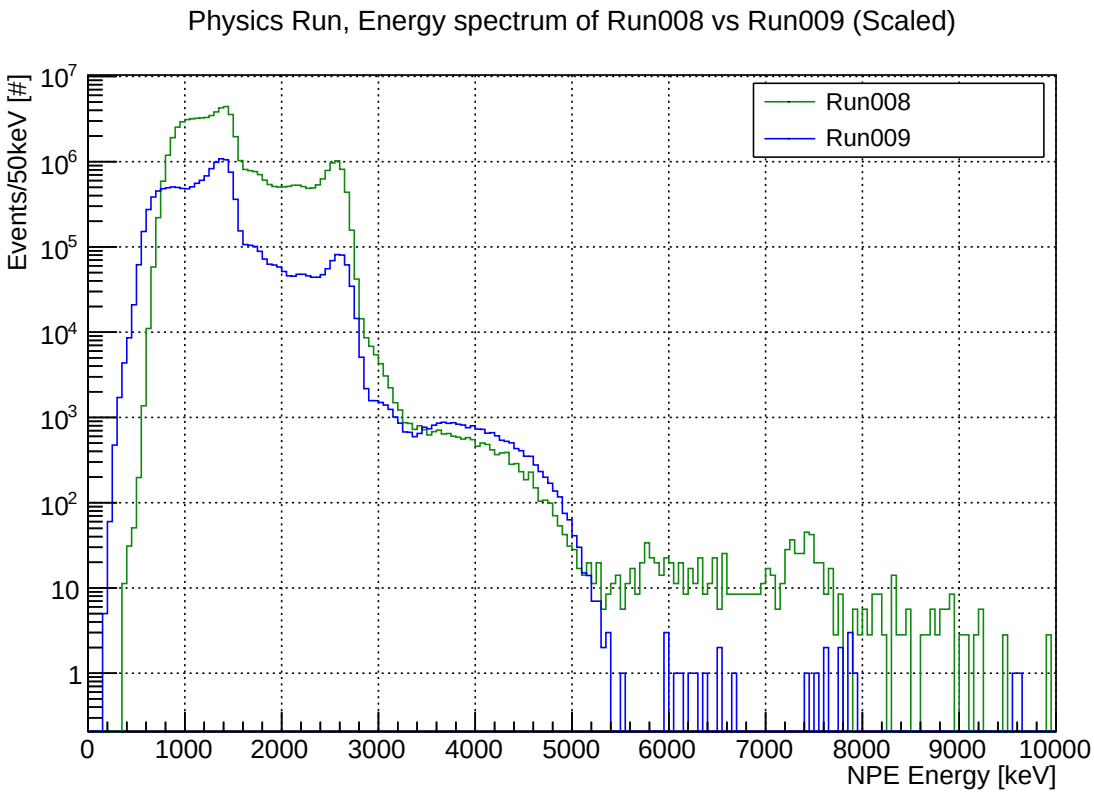

Figure 9.26.: Total Physics run energy spectra of Run008 (green) and Run009 (blue) with the same rejection efficiency cut. The spectra are scaled according to their livetimes. For Run009 data, a $\chi^2_\beta < 3$ cut is applied. The cut for Run008 is made at the same ^{214}Bi ($\beta + \gamma$) rejection efficiency (about $\chi^2_\beta < 5$). The gap in the ^{208}Tl $\beta + \gamma$ region (about 3.4 MeV to 5 MeV) has decreased by a small margin.

In order to quantify the resulting systematic error, the ratio of Run009 to Run008 ^{208}Tl $\beta + \gamma$ events has to be calculated. The only question left is which energy region should be used for this purpose. One possibility is to vary the lower and upper edge of the investigated energy region in order to derive an averaged systematic error. The result of this approach is shown in figure 9.28. A 3D version of the plot can be found in subsection B.2.1.

Based on this analysis, the averaged systematic error caused by the χ^2_β cut is about 28%. Thus, more events from Run009 would have been cut with an ideal beta cut compared to the actually used χ^2_β cut. Unfortunately, the origin of the flawed χ^2_β cut is not known. Hence, it can only be assumed that this circumstance also applies to the high-energy region.

Keeping this in mind, the later on derived reduction factors for rock and tank (n,γ) background should be considered as conservative estimates due to the 28% systematic error.

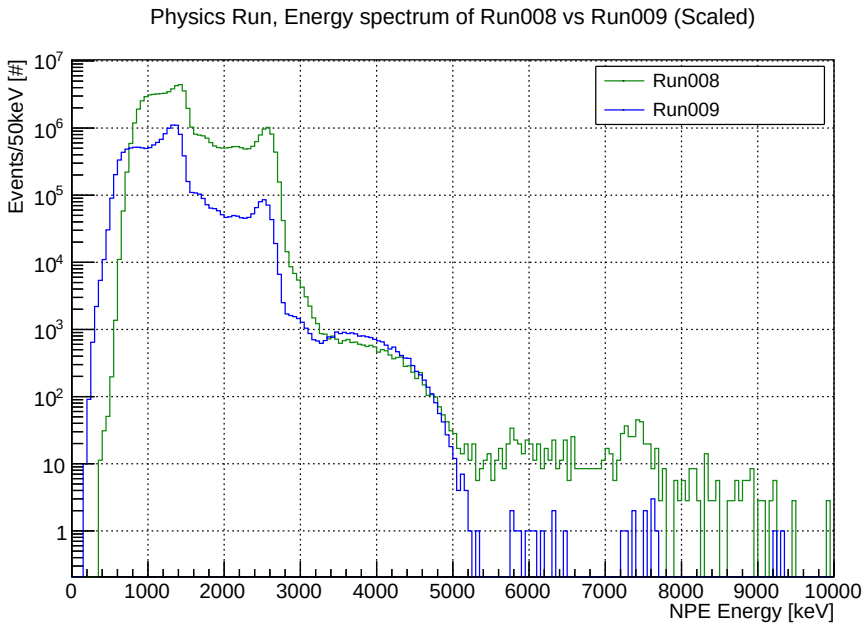

Figure 9.27.: Total Physics run energy spectra of Run008 (green) and Run009 (blue) with the same rejection efficiency cut. The spectra are scaled according to their livetimes. Additionally, the Fe peaks of both spectra are aligned. For Run008, the 7.6 MeV iron peak position can be derived based on the Physics run data. For Run009 though, the statistics is too low. Hence, ^{252}Cf source run data has been used in order estimate the peak position for Run009. The disagreement of both spectra decreases significantly.

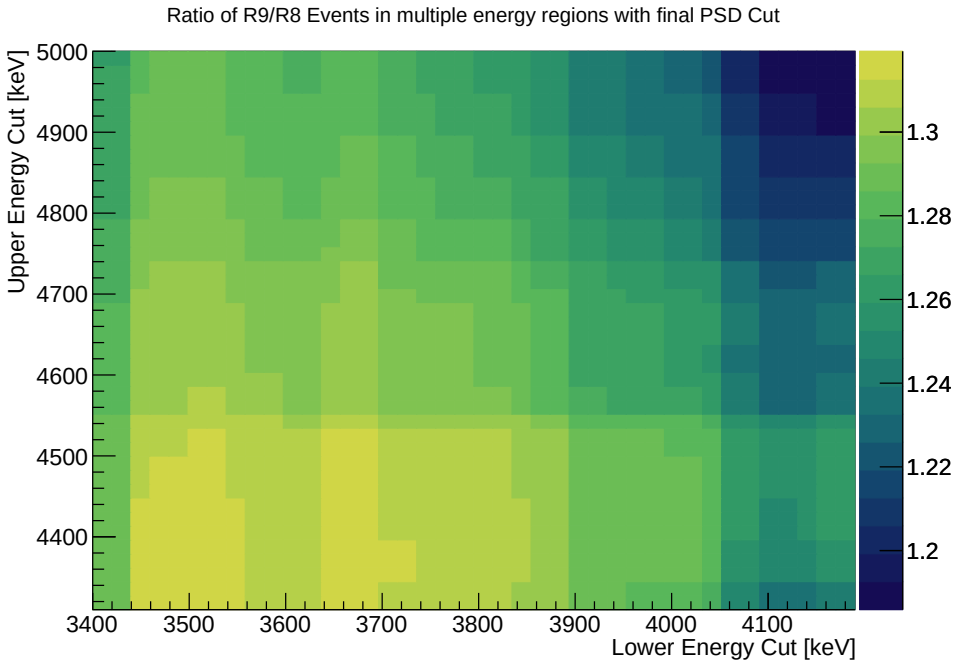

Figure 9.28.: Ratio of Run009 to Run008 events in multiple energy regions with the final same χ^2_β rejection efficiency cut (iron peaks aligned). The averaged ratio, derived by a fit, is 1.28.

9.3.2. Fitting of Physics run data

At this point, the data for Run008 and Run009 has been reduced and the final (n,γ) reduction factor analysis can be started. As already mentioned, the effectiveness of the detector shield will be estimated by analyzing the high-energy region from 5.5 MeV to 10 MeV. In this case, the data needs to be fitted with the simulated rock and tank (n,γ) spectra, since both background types are contained in it. For this purpose, the simulated spectra are smeared in order to account for the energy resolution of the detector. Then, the data is divided into 45 bins with 100 keV width each.

Usually, one can employ a least squares fit method for the fitting:

$$\chi^2 = \sum_{i=1}^{45} \frac{(N_{\text{Data}}(i) - N_{\text{Spec}}(i))^2}{\sigma^2} \tag{9.1}$$

$$N_{\text{spec}}(i) = \alpha \cdot N_{\text{rock-MC, NoSh/Sh}}(i) + \beta \cdot N_{\text{tank-MC, NoSh/Sh}}(i) \tag{9.2}$$

With:

- N_{Data} : The energy spectrum of the reduced data sample (Run008 or Run009).
- N_{Spec} : The energy spectrum of the simulated Monte Carlo model.
- $N_{\text{rock-MC, NoSh/Sh}}$: The energy spectrum of the simulated rock (n,γ) MC with (Run009) or without (Run008) a detector shield.
- $N_{\text{tank-MC, NoSh/Sh}}$: The energy spectrum of the simulated tank (n,γ) MC with (Run009) or without (Run008) a detector shield.
- α, β: The fit parameters for the rock (α) and tank (β) (n,γ) contribution. These parameters should not be compared to each other, as the simulations are not based on an expected flux. After the fit is finished, the parameters (α, β) are used to scale the simulated spectra according to the parameter fit values. Then, the simulated spectra can be integrated in the 5.5 MeV to 10 MeV energy region in order to derive the fit result for the number of rock and tank events.

Equation 9.1 estimates the variance with a Gaussian standard deviation $\sigma^2 = \sigma^2_{\text{Data}} + \sigma^2_{\text{MC}}$. However, the statistics of the data in Run008 and especially in Run009 is not large enough to make this approximation, cf. figure 9.27. The reason is that the data actually follows a Poisson distribution which only transforms into a Gaussian one for $N \to \infty$.
Thus, the chi-square has to be based on a Poisson assumption.

Keeping this in mind, the χ^2 can be transformed [51]:

$$\chi^2 = \sum \frac{(N_{\text{obs}} - N_{\text{spec}})^2}{\sigma^2} = -2 \sum \ln \frac{G(N_{\text{obs}}, N_{\text{spec}})}{G(N_{\text{obs}}, N_{\text{obs}})} \tag{9.3}$$

$$G(N_{\text{obs}}, N_{\text{spec}}) = \frac{\exp(-(N_{\text{obs}} - N_{\text{spec}})^2/2\sigma^2)}{\sqrt{2\pi}\sigma}$$

with $G(N_{\text{obs}}, N_{\text{spec}})$ as a Gaussian distribution.

After that, the Gaussian distribution can be replaced by a Poisson distribution:

$$\begin{aligned}\chi^2_{\mathrm{P}} = -2\ln\mathcal{L} &= -2\sum \ln\frac{P(N_{\mathrm{obs}}, N_{\mathrm{spec}})}{P(N_{\mathrm{obs}}, N_{\mathrm{obs}})} \\ &= -2\sum\left(\frac{N_{\mathrm{spec}}}{N_{\mathrm{obs}}}\right)^{N_{\mathrm{obs}}}\exp(N_{\mathrm{obs}} - N_{\mathrm{spec}}) \\ &= \quad 2\sum\left(N_{\mathrm{spec}} - N_{\mathrm{obs}} + N_{\mathrm{obs}}\ln\left(\frac{N_{\mathrm{obs}}}{N_{\mathrm{spec}}}\right)\right)\end{aligned} \tag{9.4}$$

with

$$P(N_{\mathrm{obs}}, N_{\mathrm{spec}}) = \frac{(N_{\mathrm{spec}})^{N_{\mathrm{obs}}}\exp(-N_{\mathrm{spec}})}{N_{\mathrm{obs}}!}$$

and $\mathcal{L}$ as the Likelihood function.
Now, the data for Run008 and Run009 can be fit with aid of the simulated spectra by using the Minuit minimizer in a binned Maximum Likelihood (χ^2_{P}) fit approach. Previously though, the energy scale of the smeared MC spectra and the Physics run data has to be aligned. This can be done with aid of the 7.6 MeV Fe peak.

The final fit result for Run008 is shown in figure 9.29.

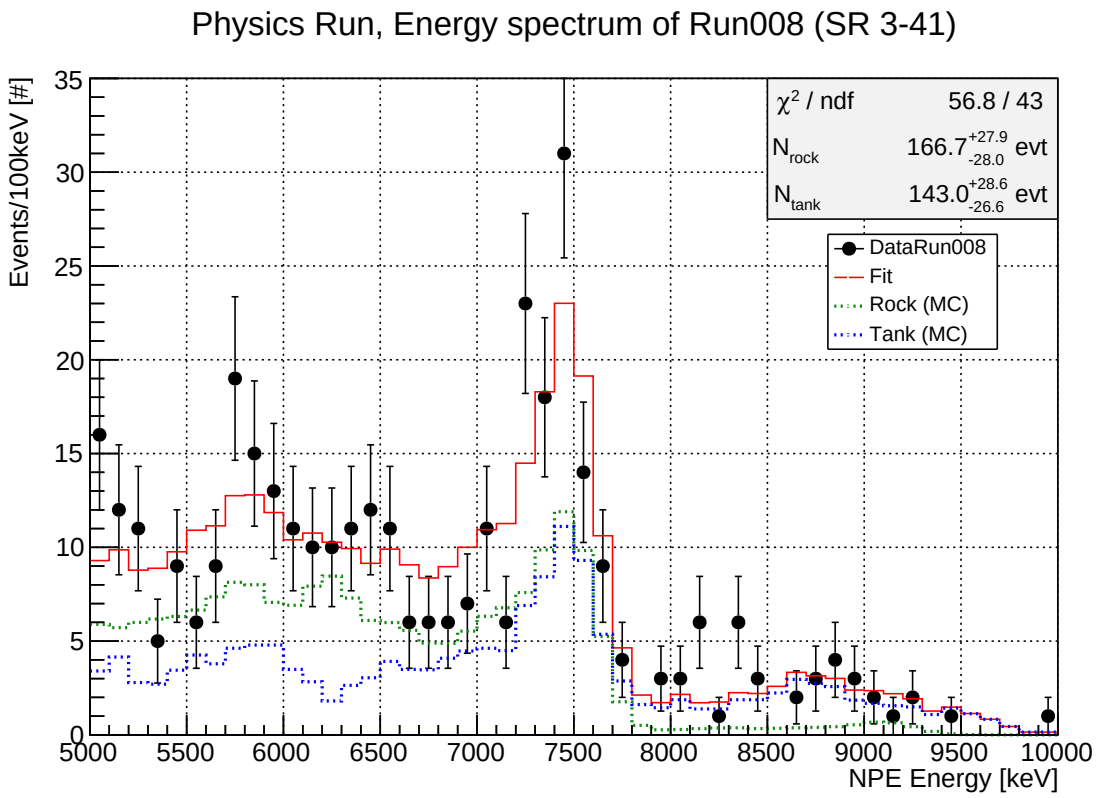

Figure 9.29.: Fitted Physics run data spectrum for Run008. The data points are indicated in black with $\sqrt{N}$ error bars. The individual contributions of the rock and tank (n,γ) spectra are displayed in green and blue. Additionally, the total summed (n,γ) spectrum is shown in red. The fit is executed from 5.5 MeV to 10 MeV and the MC spectra were aligned to the data spectrum based on the 7.6 MeV iron peaks before the fit.

Considering the statistics of Run008, the data is fit well with a χ^2_{red} of 1.3.

The number of (n,γ) background events is estimated as follows:

$$N_{\text{R8, Rock}} = 166.7^{+27.9}_{-28.0} \text{ evt / 26.4 d}$$

$$N_{\text{R8, Tank}} = 143.0^{+28.6}_{-26.6} \text{ evt / 26.4 d}$$

Thus, it can already be seen that the statistical errors on the parameters are relatively large ($> \pm 15\%$) due to the low statistics. Additionally, it can be figured that the errors are slightly asymmetric for the tank. The reason is that the 1σ confidence interval is defined as the parameter region which satisfies

$$\Delta \ln(\mathcal{L}) = \ln(\mathcal{L}_{\max}) - \ln(\mathcal{L}) < 0.5$$

Accordingly, the region can also be defined as the area in which the χ^2_{P} rises by 1. This is only an approximation for non-normally distributed data, and with low N it might not give exactly the correct 68% coverage. Thus, the asymmetric errors indicate, that the χ^2_{P} distribution is not a parabola anymore in the region of the minimum. This circumstance will be further discussed later on, when the reduction factors are derived.

At last, the fit for Run009 can be executed. The result is shown in figure 9.30.

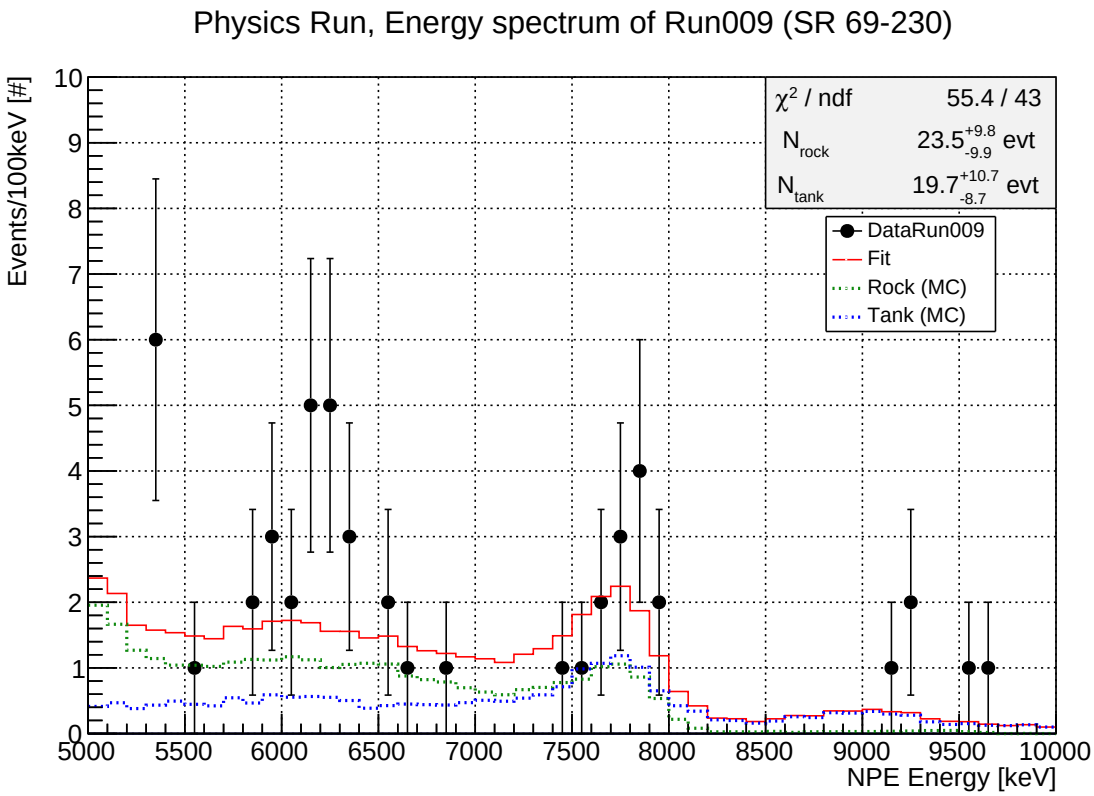

Figure 9.30.: Fitted Physics run data spectrum for Run009. The data points are indicated in black and the individual contributions of the rock and tank (n,γ) spectra are displayed in green and blue. Additionally, the total summed (n,γ) spectrum is shown in red. The fit is executed from 5.5 MeV to 10 MeV and the MC spectra were aligned to the data spectrum based on the 7.6 MeV iron peaks before the fit. This time however, the peaks are aligned based on the Calibration data of Run009 due to the low statistics in the Physics run data. It can be seen that Run009 has significantly less statistics than Run008.

As expected, the Physics data of Run009 has significantly less statistics than Run008.

Unfortunately, this makes the estimation of the rock and tank (n,γ) contributions even more difficult:

$$N_{\text{R9, Rock}} = 23.5^{+9.8}_{-9.9} \text{ evt / } 132.6\,\text{d}$$

$$N_{\text{R9, Tank}} = 19.7^{+10.7}_{-8.7} \text{ evt / } 132.6\,\text{d}$$

The errors on the (n,γ) background estimations are about $\pm 50\%$. One reason for this is based on the small statistics of Run009. Furthermore, the shapes of the rock and tank spectra differ the most in the 8 MeV to 10 MeV region. Unfortunately, this energy region only contains 5 events. At the same time, the 6 MeV to 6.5 MeV energy region has more events than the 7.6 MeV iron peak region, which is unexpected. However, it could only be a fluke due to the low statistics data sample. Before this final analysis, the same fit had been done with about 76 d of livetime. In this case, the situation was reversed (more events in the 7.6 MeV energy region). In the future, more data can solve this issue.

9.3.3. Systematic errors

Before we can continue with the analysis, errors other than the statistical errors have to be considered. These systematic errors are as follows:

- Different rejection efficiency in the χ^2_β cut for Run008 and Run009. The error has been estimated to be a conservative one with about 28%, if the discrepancy translates 1:1 from the ^{208}Tl $\beta + \gamma$ energy region to the high-energy (n,γ) region.

- The uncertainty on the energy resolution of Run008 and Run009, which is about 10%. The energy resolution has been used in order to smear the simulated rock and tank spectra. The impact of this error can be estimated by smearing the simulated spectra with a 10% higher or lower energy resolution. The resulting difference in the fit (N_{rock}, N_{tank}) is less than 0.5% for both runs. Thus, the error can be neglected, since it is small compared to the statistical error.

- The uncertainty in the NPE- and ADC-Energy. In the fits, the NPE-Energy has been used. The difference of the NPE- and ADC-Energy energy is about 1% (30 keV@2.6 MeV). This is small compared to the statistical error and the systematic 28% χ^2_β cut error.

- The nonlinearity of the energy scale in Run008 ($\approx 2\%$) and Run009 ($< 1\%$). As before, it can be neglected.

- The different energy scale of Run008 and Run009. The 7.6 MeV iron peak position offset between both runs is about 200 keV (3%). This can have an effect on the estimated number of rock and tank events, as the events are counted in the same 5.5 MeV to 10 MeV energy range for both runs. Nevertheless, it is known that the energy scale of Run009 can be considered as the more precise one, due to the nearly complete elimination of the energy scale nonlinearity. Hence, a rough solution would be to count the rock and tank events of Run008 in the 5.3 MeV to 9.8 MeV energy region. Due to the shape of the (n,γ) background, more events would be counted for Run008 data. Thus, this error is conservative as well.

- Minor errors like e.g. the alignment of the data and MC iron peaks. These errors can be neglected.

As a result, the only significant systematic error is the 28% difference in χ^2_β cut efficiency. Consequently, the following results of the analysis should be considered as conservative estimates.

9.3.4. Estimation of an upper limit on Rock and Tank events

Before the reduction factors are calculated, it is also of interest to derive an upper limit on the number of rock and tank events in Run009. The procedure for extracting the upper limit based on the fit results is as follows (only demonstrated for the rock case)[51]:

1. Obtain the χ^2 distribution as a function of α. This can be done by minimizing the χ^2 with a fixed α and a free parameter β. Then, the χ^2 values at each α are defined as χ^2_α. The χ^2_α distribution is shown in figure 9.31a.

2. Calculate the probability for each χ^2_α:

$$\text{Probability} = C \cdot \exp\left(-\frac{\chi^2_\alpha}{2}\right) \tag{9.5}$$

   C is a normalization factor in order to make the integrated probability equal to one. Thus, it can be derived as follows:

$$1 = \int_{\alpha=0}^{\infty} C \cdot \exp\left(-\frac{\chi^2_\alpha}{2}\right) d\alpha \tag{9.6}$$

3. Derive the sum of the probability by integrating the probability from $\alpha = 0$ up to $\alpha = 0.004$ (ideally $\alpha = \infty$) step by step. The result can be found in figure 9.32. Then, the α 90% confidence limit (CL) upper limit, α_{90}, can be found by looking for the α whose summed probability exceeds 0.9. Multiplying the α_{90} with the corresponding simulated energy spectrum (rock, with shield) and integrating from 5.5 MeV to 10 MeV yields the upper limit on the (rock) number of events in the Run009 data at 90% CL.

$$\mathrm{N_{Rock,\ R9}} < 36.2\,\text{evt} \ /\ 132.6\,\text{d} \ /\ 96 \text{ crystals (5.5 MeV to 10 MeV, @90\% CL)}$$

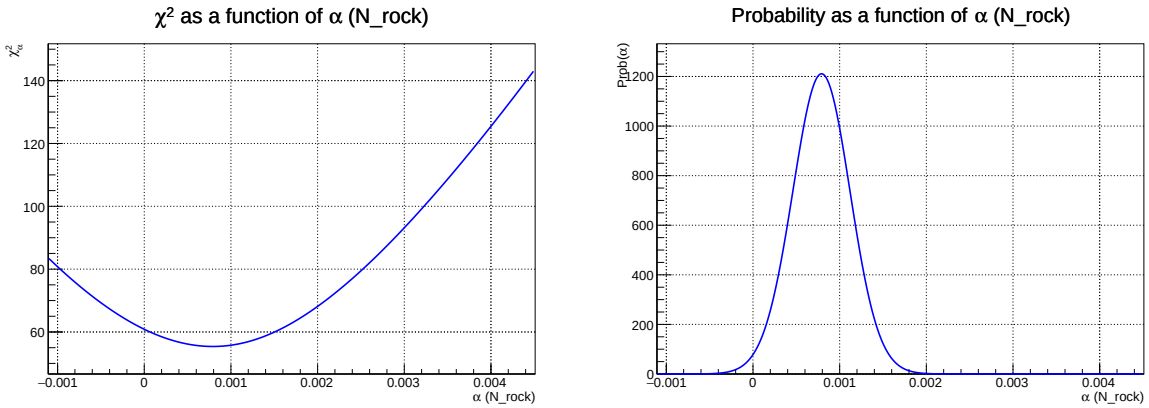

(a) χ^2_α distribution

(b) Probability as a function of α

Figure 9.31.: Chi-square and probability as a function of α for Run009 Physics run data. It can be seen that the χ^2_α distribution has a parabolic shape next to the minimum. Additionally, the χ^2_α minimum at around 0.0009 is related to the fit result that has been shown in subsection 9.3.2. Likewise, the errors of the fit result had been estimated by deriving the parameter region which satisfies $\Delta\chi^2_{\mathrm{P},\alpha} < 1$.

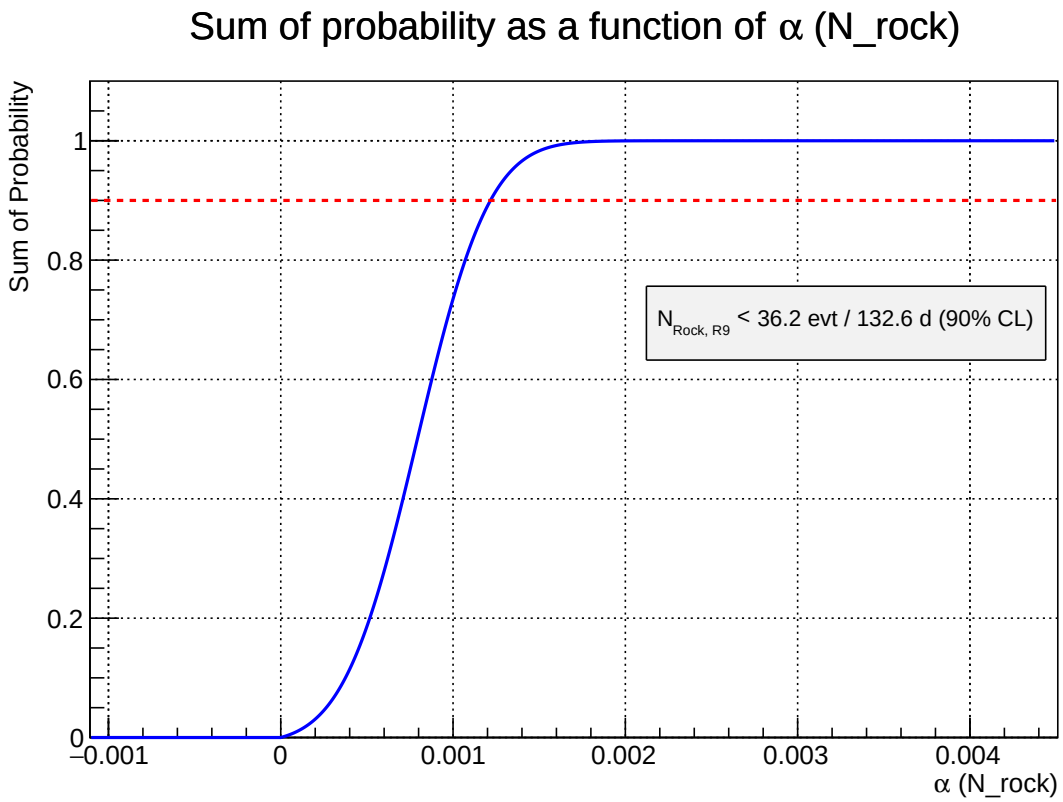

Figure 9.32.: Sum of probability as a function of α (rock) for Run009 data. The 90% confidence level rock upper limit is shown as the dotted red line. It corresponds to the value of α at a summed probability of 0.9.

The same procedure can be applied for the tank (n,γ) upper limit and the results are shown in figure 9.33 and figure 9.34. Thus, the resulting upper limit can be given as

$$\mathrm{N_{Tank,\ R9}} < 36.0\,\mathrm{evt}\ /\ 132.6\,\mathrm{d}\ /\ 96\ \text{crystals}\ (5.5\,\mathrm{MeV}\ \text{to}\ 10\,\mathrm{MeV},\ @90\%\ \mathrm{CL})$$

This is actually nearly the same as for the rock upper limit, due to the higher relative errors in the tank case. Additionally, the non-parabolic shape of the χ^2_β distribution (and thus the log-likelihood) can be seen.

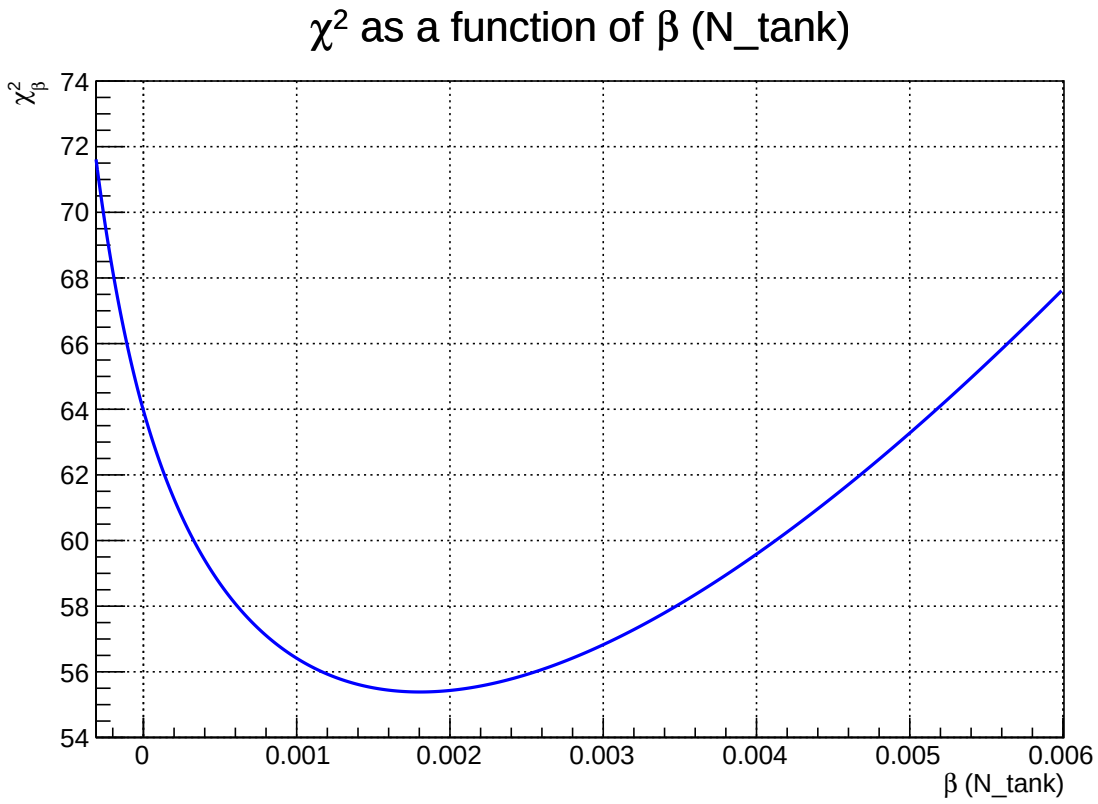

Figure 9.33.: Chi-square distribution as a function of β (tank) for Run009 Physics run data. It can be seen, that the shape of the distribution is not a symmetric parabola anymore. Thus, an asymmetric error on the fit parameter β is found.

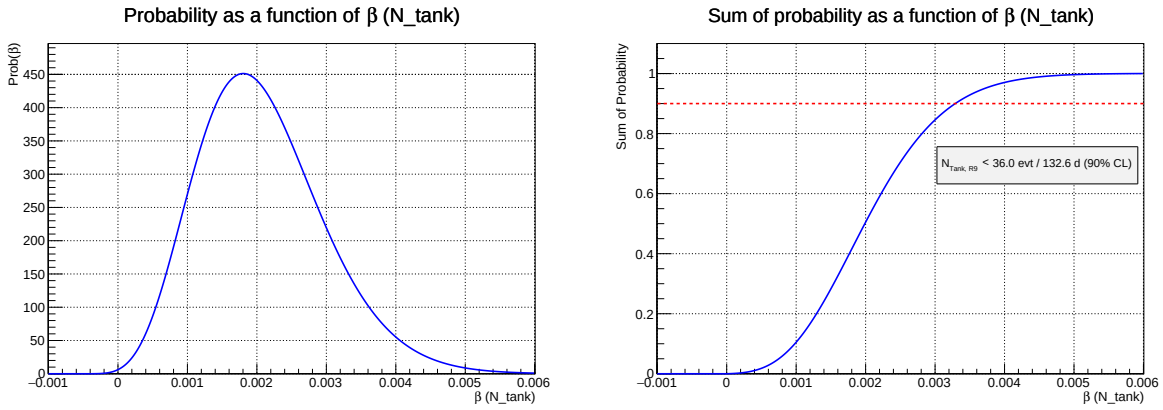

(a) Probability as a function of β

(b) Summed probability of β

Figure 9.34.: Probability and sum of probability as a function of β (tank) for Run009 Physics run data. The resulting upper limit is as follows:
$N_{\text{Tank, R9}} < 36.0\,\text{evt} \;/\; 132.6\,\text{d} \;/\; 96$ crystals (5.5 MeV to 10 MeV, @90% CL).

9.3.5. Calculation of the reduction factors

In this final paragraph of the analysis, the reduction factors for the rock and tank (n,γ) background will be calculated based on the Physics run data fit. For this purpose, the different livetimes of Run008 and Run009 have to be taken into account.

Afterwards, the reductions can be calculated as follows:

$$\text{Reduction}_{\text{Rock/Tank}} = \frac{\text{Event-Number}_{\text{R9, Rock/Tank}}}{\text{Event-Number}_{\text{R8, Rock/Tank}}} \tag{9.7}$$

Here, the "Event-Number" is equal to the (livetime scaled) number of events that has been derived in the fit for Run008 or Run009.
Thus, the principal technique is to calculate a ratio of two independent variables:

$$f(x, y) = \frac{x}{y}$$

Usually, the propagated errors of this function are calculated by expanding the function f in a multidimensional Taylor-series.

$$f(x, y) \approx f^0 + \frac{\partial f}{\partial x} x + \frac{\partial f}{\partial y} y + \cdots \tag{9.8}$$

Then, the expansion is terminated after the first-order and the following equation for the error propagation is derived:

$$\sigma_f^2 \approx \left(\frac{\partial f}{\partial x}\right)^2 \sigma_x^2 + \left(\frac{\partial f}{\partial y}\right)^2 \sigma_y^2 + 2\frac{\partial f}{\partial x}\frac{\partial f}{\partial y}\rho_{xy}\sigma_x\sigma_y \tag{9.9}$$

The last term represents the covariance of x and y through the correlation coefficient ρ_{xy}. In our case, the variables are independent, such that this term can be ignored:

$$\sigma_f^2 \approx \left(\frac{\partial f}{\partial x}\right)^2 \sigma_x^2 + \left(\frac{\partial f}{\partial y}\right)^2 \sigma_y^2 \tag{9.10}$$

For this approximation, it is vital that the errors are Gaussian ones and that f can be approximated linearly in the 1σ error range.

In our particular case, multiple problems exist in the context of the error propagation:

- The Gaussian approximation is only valid as long as the relative errors of the variables are small. Otherwise, a symmetric distribution of e.g. x can lead to an asymmetric distribution of the error in f. In this analysis, the errors are quite large with about 20% in Run008 and 50% in Run009.
- The errors of the fit result for the tank scenario are asymmetric and thus certainly not Gaussian. A common technique is to just add the upper and lower error separately in quadrature. However, there is no theoretical justification for this procedure [52].
- The result of a ratio calculation can be nonlinear. In example, a Gaussian distribution divided by a Gaussian distribution may result in a (asymmetric) non-Gaussian distribution.

As such, propagating the errors with a second method is advisable.

One possible solution is to calculate the associated errors of the reductions based on toy Monte Carlo simulations. This approach uses the already derived probabilities that exist for each run (Run008, Run009) and (n,γ) background type (rock, tank).

The method for the rock (tank) reduction is as follows:

1. Create a random rock event number for Run008 (without shield) and Run009 (with shield) based on the respective probability curves. For this purpose, a Mersenne Twister generator is used to generate random numbers that are distributed according to the normed probability distributions of the rock fit. The Run008 rock probability graph is shown in figure 9.35a.

2. For every pair of rock event numbers (Run008, Run009), calculate the reduction factor:

$$\text{Reduction}_{\text{Rock}} = \frac{\text{Event-Number}_{\text{R9, Rock}}}{\text{Event-Number}_{\text{R8, Rock}}}$$

3. Repeat 1) and 2) until the statistics of the reduction factors is large enough (10^7).

4. Derive the 1σ (68.3%) region of the resulting rock reduction distribution. Then, calculate the distance of the lower and upper edge of the 68% CI to the reduction based on the best-fit values for Run008 and Run009. The rock reduction distribution is shown in figure 9.36. As a result, an upper and a lower error for the rock reduction factor is derived.

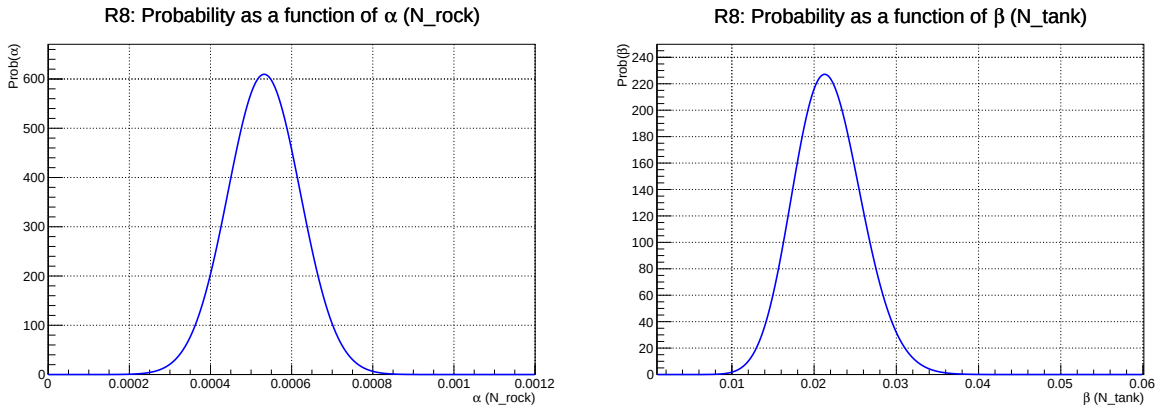

(a) Rock (α) (b) Tank (β)

Figure 9.35.: Probability as a function of α and β for Run008. The shown probabilities are not yet normed to 1. As before, the probabilities have been calculated with aid of the χ^2 distributions whose derivation is specified in subsection 9.3.4. The probabilities are used to generate random event numbers for the rock and tank reductions.

The same can be done for the tank reduction factor, whose distribution is shown in figure 9.37. Finally, the reduction factors for the rock and tank (n,γ) background based on the Physics run data analysis can be concluded.

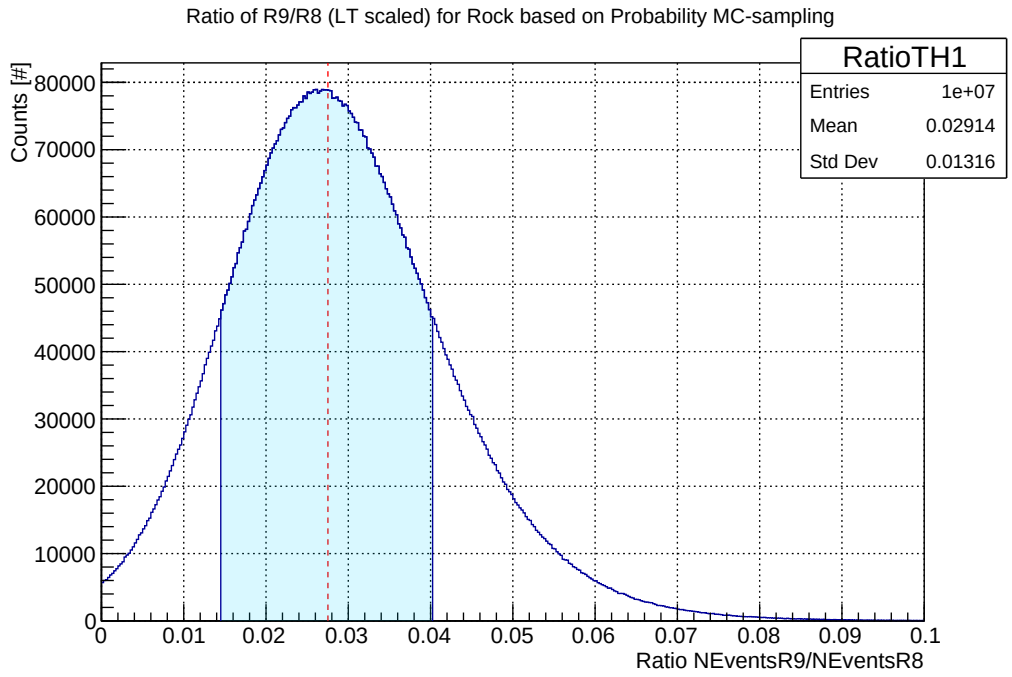

Figure 9.36.: Rock reduction factor distribution generated by a toy Monte Carlo simulation. The best-fit value for the rock reduction factor is shown as the red dotted line. The area shaded in blue is the 1σ region. It can be derived by intercepting the distribution with a down-going vertical line starting from the top. Afterwards, the X-axis values with the same Y-value are used as integration interval boundaries. The 1σ region is reached, when the integration surpasses 68.3% entries of the total distribution.

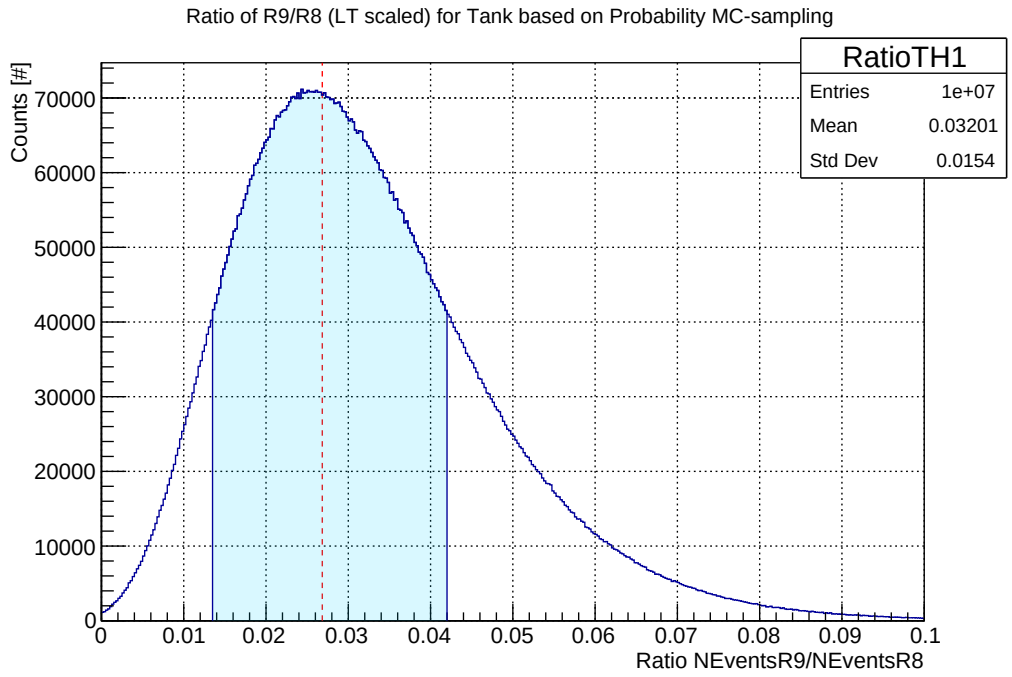

Figure 9.37.: Tank reduction factor distribution generated by a toy Monte Carlo simulation. The best-fit value for the tank reduction factor is shown as the red dotted line. The area shaded in blue is the 1σ region. It can be seen that the distribution is asymmetric.

The results are shown with MC based errors and analytical errors based on equation 9.10. In the latter case, the tank errors are propagated individually for the lower and upper error.

	Toy-MC	Analytical
Rock (n,γ) Reduction:	$0.028^{+0.012}_{-0.013}$	0.028 ± 0.13
R9/R8 (LT scaled)	$\approx 1/36$	$\approx 1/36$
Tank (n,γ) Reduction:	$0.027^{+0.014}_{-0.015}$	$0.027^{+0.016}_{-0.013}$
R9/R8 (LT scaled)	$\approx 1/37$	$\approx 1/37$

Table 9.4.: Final (n,γ) reduction factors (5.5 MeV to 10 MeV) with errors either based on the toy Monte Carlo method or on the analytical error propagation.

It can be seen that the difference between both error propagation techniques is negligible. Thus, it strengthens the belief that the shown statistical errors are accurate. Nevertheless, the already discussed systematic errors have to be kept in mind as well. Based on the toy MC distribution for the tank, it can be estimated that the asymmetry of the errors becomes larger at 2σ errors compared to the shown 1σ errors.

9.3.6. Discussion

At this point, the derived (n,γ) reduction factors of the data can be compared to the expected ones that are based on MC simulations.

Previous MC studies show that the expected tank (n,γ) natural background reduction is expected to be about 1/40. The analysis results of 1/37 agree well with this expectation, though the statistical errors are large (50%). For the rock, a reduction of about 1/350 is expected. This analysis shows a best-fit value of 1/36, and a reduction of 1/350 is not contained in the 68% CI. However, 68% is not a very stringent confidence interval. Thus, it is interesting to estimate if the concluded rock reduction factor is within the 2σ (95.5%) CI. Calculating the 95% confidence interval based on the tank reduction toy MC distribution shows that a reduction of 1/350 is equal to the lower edge of the 2σ region, cf. figure 9.38.

Additionally, the possible conservative 28% error from the χ^2_β cut has to be kept in mind. Consequently, the analysis results of 1/36 agree to the expectations of about 1/350 within the statistical 2σ error region. This subject should be investigated again, when more Physics run data of Run009 is available, as the improved statistics will lead to a more precise result.

As a result, it can be concluded that the Physics run data agrees with the expected (n,γ) reductions. However, the shield effect on the (n,γ) background is so huge, that the surviving background does not provide enough statistics for a detailed analysis with the Physics run data of one third of a year. Hence, it may be advisable to use the derived reduction factors as a basis for a lower limit of the (n,γ) background reduction. In example, the upper 95% CI edge of the rock reduction is about 1/18. In the future, these upper limits can be improved with more available data from Run009.

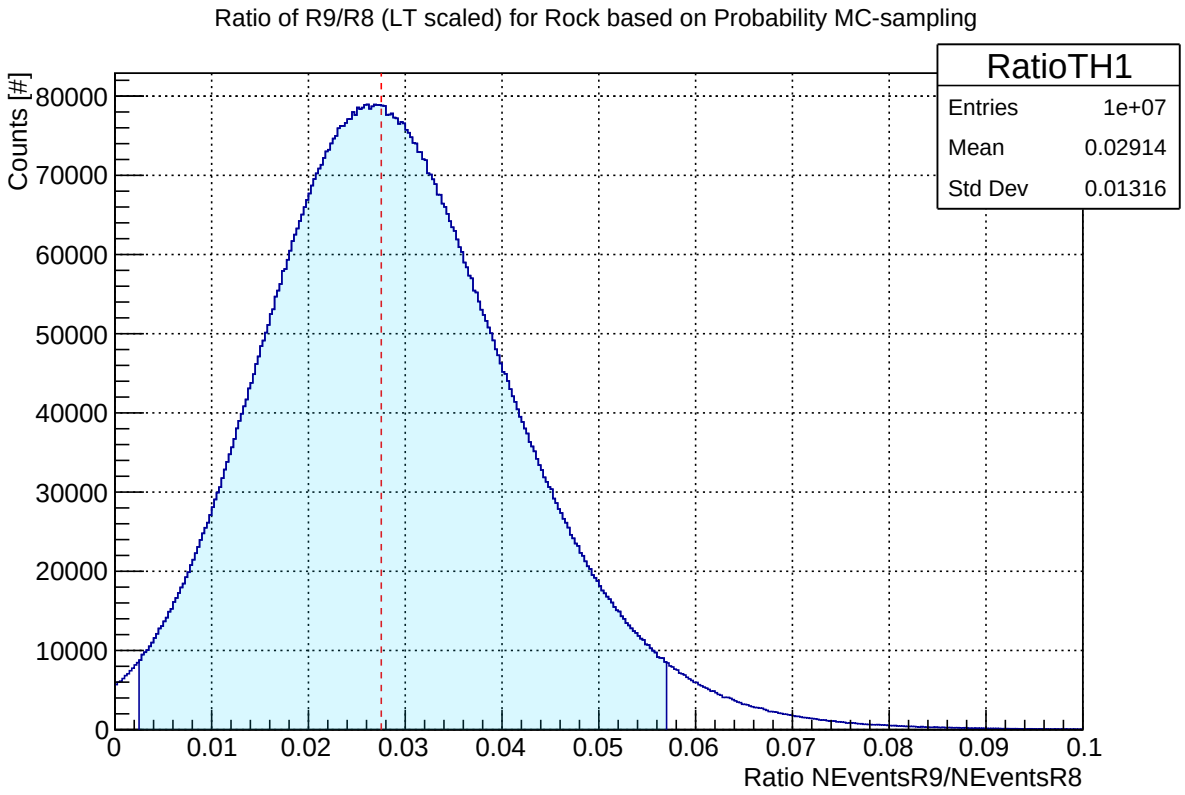

Figure 9.38.: Tank reduction factor distribution generated by a toy Monte Carlo simulation with a highlighted 2σ error region. The best-fit value for the tank reduction factor is shown as the red dotted line. The area shaded in blue is the 2σ region.

10. Summary and outlook

As it has been demonstrated, the search for neutrinoless double beta decay is an active research field with lots of different experimental groups. In CANDLES, we try to observe the neutrinoless double beta decay in a very low to no background condition. The current goal is to reach less than one background event per year and 96 CaF_2 crystals. This is made possible due to the high $Q_{\beta\beta}$ value of ^{48}Ca. Unfortunately, the enrichment of ^{48}Ca proves to be difficult and expensive as of now. However, if a breakthrough could be made in the enrichment, the normal hierarchy may very well be in reach of a future CANDLES detector. For this purpose, one needs to be able to manage a stable detector operation over years and the no background condition should be reached. In this context, two studies have been presented and developed. One focuses on the energy scale stability of the detector, while the other one investigates the (n,γ) background after the installation of a detector shield.

10.1. Detector performance - Energy scale and event rate stability

In the first study, it could be shown that the differently calibrated ADC- and NPE-Energies currently show a large (1% @2.6 MeV) discrepancy for Run009 data. New data that has been available after the analysis of this thesis was finished shows that the problem still persists. As of now, considerable efforts are spent in order to find a solution for the current issues. Thus, it demonstrates how important it is to monitor and confirm the detector calibration over time.
Additionally, it has been concluded that the new fit method for the energy scale analysis lacks precision and reliability. In the current scope, the precision can be considered as good enough. However, a better method should still be developed. One option could be to include the low energy region left of the ^{40}K peak in the fit, whose spectrum is primarily based on the triggering.

10.2. (n,γ) background study

The second main study about the (n,γ) background showed that the background reduction due to the new detector is difficult to estimate precisely right now. In this context, the shield efficiency is so high, that only a little amount of the background survives. Principally, a neutron source like ^{252}Cf can be used in order to derive more statistics. Unfortunately, measurements with a high intensity source are currently not possible due to other adjacent experiments. Additionally, the old source run data which was taken before the shield construction shows inconsistencies. And even then, the different energy spectrum of the ^{252}Cf neutrons compared to the environmental neutrons makes a precise estimation of the (n,γ) background reduction difficult.

Thus, the Physics run data with little statistics has to be used. Based on this data, reduction factors have been derived that agree with the expected reduction. However, the low statistics of the Run009 data sample limits the accuracy of the analysis. Hence, the only solution to this issue is to record more data. Then, the analysis could be repeated after one to two years of data.

At the same time, the analysis methods like the χ^2_β data cut can be improved. Unfortunately, this proves to be a difficult task, as one would principally have to estimate a rejection efficiency for all of the different background types else than beta events. Nevertheless, an investigation has been started in order to get insight on the question why a same rejection efficiency cut based on ^{214}Bi $\beta + \gamma$ events is not sufficient.

As a result, it can be figured that the study of the remaining (n,γ) background in CANDLES is still an interesting research field.

Bibliography

[1] Kishimoto Lab Osaka University. *Neutrinoless double beta decay.* URL: https://wwwkm.phys.sci.osaka-u.ac.jp/en/research/img/r01_img01.gif (visited on 06/30/2016).

[2] Frank T. Avignone, Steven R. Elliott, and Jonathan Engel. "Double Beta Decay, Majorana Neutrinos, and Neutrino Mass." In: *Rev.Mod.Phys.* 80:481-516,2008 (Aug. 2007). DOI: 10.1103/RevModPhys.80.481. eprint: 0708.1033.

[3] Ettore Majorana. "Teoria simmetrica dell'elettrone e del positrone." In: *Il Nuovo Cimento* 14 (1937).

[4] The Super-Kamiokande Collaboration and Y. Fukuda et al. "Evidence for oscillation of atmospheric neutrinos." In: *Phys.Rev.Lett.* 81:1562-1567,1998 (Phys.Rev.Lett.81:1562-1567,1998). DOI: 10.1103/PhysRevLett.81.1562. eprint: hep-ex/9807003.

[5] The KamLAND Collaboration. "Measurement of Neutrino Oscillation with KamLAND: Evidence of Spectral Distortion." In: *Phys.Rev.Lett.* 94:081801,2005 (Phys.Rev.Lett.94:081801,2005). DOI: 10.1103/PhysRevLett.94.081801. eprint: hep-ex/0406035.

[6] The ANTARES collaboration et al. "Measurement of Atmospheric Neutrino Oscillations with the ANTARES Neutrino Telescope." In: *Phys. Lett. B 714* (June 2012). DOI: 10.1016/j.physletb.2012.07.002. eprint: 1206.0645.

[7] Hitoshi Murayama. URL: http://scienceblogs.com/startswithabang/files/2013/07/masses.jpg (visited on 09/05/2016).

[8] Heinrich Päs and Werner Rodejohann. "Neutrinoless Double Beta Decay." In: *New J. Phys.* (July 2015). DOI: 10.1088/1367-2630/17/11/115010. eprint: 1507.00170.

[9] Gary Steigman. "Primordial Nucleosynthesis in the Precision Cosmology Era." In: *Ann.Rev.Nucl.Part.Sci.* 57:463-491,2007 (Dec. 2007). DOI: 10.1146/annurev.nucl.56.080805.140437. eprint: 0712.1100.

[10] Richard A. Battye and Adam Moss. "Evidence for massive neutrinos from CMB and lensing observations." In: *Phys. Rev. Lett. 112* (Aug. 2013). DOI: 10.1103/PhysRevLett.112.051303. eprint: 1308.5870.

[11] K. A. Olive et al. "Review of Particle Physics." In: *Chin. Phys.* C38 (2014), p. 090001. DOI: 10.1088/1674-1137/38/9/090001.

[12] B. Pontecorvo. "Neutrino Experiments and the Problem of Conservation of Leptonic Charge." In: *Soviet Journal of Experimental and Theoretical Physics* 26 (May 1968), p. 984.

[13] S. M. Bilenky and C. Giunti. "Neutrinoless double-beta decay. A brief review." In: *Mod. Phys. Lett. A 27* (Mar. 2012). DOI: 10.1142/S0217732312300157. eprint: 1203.5250.

[14] S. M. Bilenky and C. Giunti. "Neutrinoless Double-Beta Decay: a Probe of Physics Beyond the Standard Model." In: *International Journal of Modern Physics A 30, 1530001 (2015)* (Nov. 2014). DOI: 10.1142/S0217751X1530001X. eprint: 1411.4791.

[15] Michael Wurm. *Neutrino mass hierarchy.*
URL: http://www.staff.uni-mainz.de/wurmm/juno.html (visited on 06/30/2016).

[16] S. Adrián-Martínez et al. "Letter of Intent for KM3NeT2.0." In: (Jan. 2016). eprint: 1601.07459.

[17] H.V. Klapdor-Kleingrothaus. *Seventy Years of Double Beta Decay.* World Scientific, 2010.

[18] Harald Fritzsch, ed.
Massive Neutrinos: Flavor Mixing of Leptons and Neutrino Oscillations.
World Scientific, 2015.

[19] Delia Tosi on behalf of the EXO Collaboration.
"The search for neutrino-less double-beta decay: summary of current experiments."
In: (Feb. 2014). eprint: 1402.1170.

[20] Samoil Bilenky. *Introduction to the Physics of Massive and Mixed Neutrinos.*
Lecture notes in Physics 817. Springer, 2010.

[21] Hidekazu Kakubata.
"Study of Backgrounds in CANDLES to Search for Double Beta Decays of 48Ca."
PhD thesis. Osaka University, Graduate School of Science, 2015.

[22] Kai Zuber. *Neutrino Physics, Second Edition.* CRC Press, 2012.

[23] J. J. Gomez-Cadenas et al. "The search for neutrinoless double beta decay."
In: *Riv. Nuovo Cim.* 35 (Sept. 2011), pp. 29–98. DOI: 10.1393/ncr/i2012-10074-9.
eprint: 1109.5515.

[24] John F. Donoghue, Eugene Golowich, and Barry R. Holstein.
Dynamics of the Standard Model. Second Edition. Cambridge University Press, 2013.

[25] A. Osipowicz et al. "KATRIN: A Next generation tritium beta decay experiment with sub-eV sensitivity for the electron neutrino mass. Letter of intent." In: (2001).
arXiv: hep-ex/0109033 [hep-ex].

[26] Wikimedia Commons.
Beispiel für die energetische Unmöglichkeit eines einfachen Beta-Zerfalls.
URL: https://de.wikipedia.org/wiki/Doppelter_Betazerfall#/media/File:Doppelbeta-massenparabel.png (visited on 06/01/2016).

[27] Yoshiyuki Hirano. "CANDLES detector for the study of Double Beta Decay of 48Ca."
PhD thesis. Osaka University, Graduate School of Science.

[28] S. Dell'Oro et al. "Neutrinoless double beta decay: 2015 review."
In: *Advances in High Energy Physics, Volume 2162659* Advances 2162659 (Jan. 2016), AdvancesinHighEnergyPhysics, Volume2016(2016), ArticleID 2162659.
DOI: 10.1155/2016/2162659. eprint: 1601.07512.

[29] J. Barea, J. Kotila, and F. Iachello. "$0\nu\beta\beta$ and $2\nu\beta\beta$ nuclear matrix elements in the interacting boson model with isospin restoration."
In: *Phys. Rev. C* 91 (3 Mar. 2015), p. 034304. DOI: 10.1103/PhysRevC.91.034304.
URL: http://link.aps.org/doi/10.1103/PhysRevC.91.034304.

[30] Evgeny Akhmedov.
"Majorana neutrinos and other Majorana particles:Theory and experiment."
In: (Dec. 2014). eprint: 1412.3320.

[31] NEXT Collaboration. *Sum of the electron kinetic energies, normalized to the endpoint Q.*
URL: http://next.ific.uv.es/next/images/stories/bbspectra.jpg (visited on 06/14/2016).

[32] Andrea Giuliani and Alfredo Poves. "Neutrinoless Double-Beta Decay."
In: *Adv. High Energy Phys.* 2012 (2012), p. 857016. DOI: 10.1155/2012/857016.

[33] Steven R. Elliott and Petr Vogel. “Double Beta decay.”
In: *Annual Review of Nuclear and Particle Science* 52 (2002).
DOI: 10.1146/annurev.nucl.52.050102.090641.

[34] K. J. R. Rosman and P. D. P. Taylor. *Isotopic compositions of the elements 1997.*
Tech. rep. Pure & Appl. Chem., Vol.70, No 1, pp. 217-235, 1998.

[35] University of Tokyo Institute for Cosmic Ray Research. *About Kamioka Observatory.* URL:
http://www-sk.icrr.u-tokyo.ac.jp/aboutus/index-e.html (visited on 06/30/2016).

[36] S. Umehara et al. “Search for Neutrino-less Double Beta Decay with CANDLES.”
In: *Phys. Procedia* 61 (2015), pp. 283–288. DOI: 10.1016/j.phpro.2014.12.046.

[37] T. Iida et al. “The CANDLES experiment for the study of Ca-48 double beta decay.”
In: *Nucl. Part. Phys. Proc.* 273-275 (2016), pp. 2633–2635.
DOI: 10.1016/j.nuclphysbps.2015.10.013.

[38] T. Iida et al. “Status and future prospect of 48Ca double beta decay search in CANDLES.”
In: *J. Phys. Conf. Ser.* 718.6 (2016), p. 062026. DOI: 10.1088/1742-6596/718/6/062026.

[39] Richard B. Firestone. *Table of Isotopes.* Ed. by Virginia S. Shirley. 8th ed. Vol. 2.
John Wiley & Sons, Inc., 1996.

[40] K. Nakajima et al. “Low background techniques in CANDLES.”
In: *AIP Conf. Proc.* 1672 (2015), p. 110004. DOI: 10.1063/1.4928006.

[41] Temuge Batpurev.
“The study of multi-hit events for reductions of background in CANDLES.”
MA thesis. Department of Physics , Graduate School of Science, Osaka University, 2016.

[42] Li Xialong. “Energy scale and Event rate stability.”
Presentation at the CANDLES collaboration meeting on 30th August 2015.

[43] F. James.
“MINUIT Function Minimization and Error Analysis: Reference Manual Version 94.1.”
In: *CERN Program Library Long Writeup D506* (1994).

[44] Li Xialong. personal communication.

[45] J. F. Dicello, W. Gross, and U. Kraljevic. “Radiation Quality of Californium-252.”
In: *Physics in Medicine and Biology* 17 (May 1972), pp. 345–355.
DOI: 10.1088/0031-9155/17/3/301.

[46] Mark A. Prelas et al. “A review of nuclear batteries.”
In: *Progress in Nuclear Energy* 75 (2014), pp. 117–148.

[47] Takaki Ohata. “Detection efficiency of beta rays.”
Unpublished presentation in the CANDLES collaboration.

[48] K. Nakajima et al. “Study of neutron capture gamma ray background in CANDLES.”
Not yet published (2. Feb. 2017).

[49] Alfred Tang et al. “Muon simulations for Super-Kamiokande, KamLAND and CHOOZ.”
In: *Phys. Rev.* D74 (2006), p. 053007. DOI: 10.1103/PhysRevD.74.053007.
arXiv: hep-ph/0604078 [hep-ph].

[50] Takashi KANO and Satoshi TERAYAMA.
“Meta-dioritic and -gabbroic rocks in the Kamioka mining area, Hida metamorphic region.”
In: *Shigen-Chishitsu* 45.249 (1995), pp. 25–40.
DOI: 10.11456/shigenchishitsu1992.45.25.

[51] Takashi Iida. “Search for Supernova Relic Neutrino at Super-Kamiokande.”
PhD thesis. Department of Physics, School of Science, The University of Tokyo, 2009.

[52] Roger Barlow et al. “Recommended Statistical Procedures for BaBar.” BaBar Analysis Document number 318, version 1.

List of Figures

A. Energy scale and event rate stability plots

A.1. Analysis for Run008

A.1.1. Combined Subrun spectra for NPE/ADC

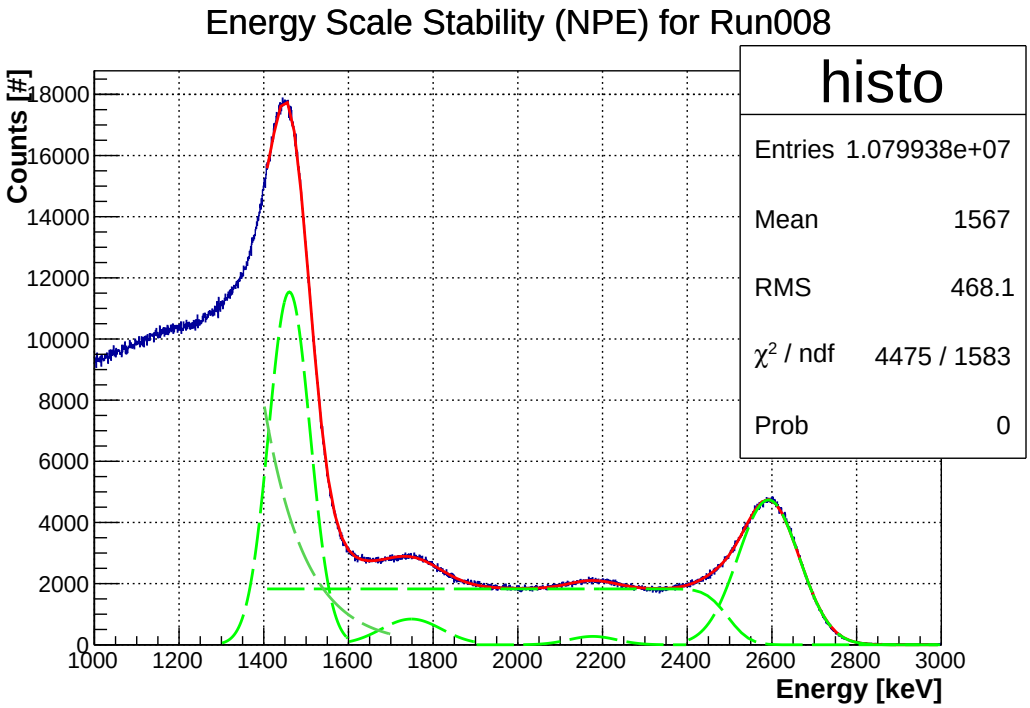

Figure A.1.: NPE energy spectrum for the whole data of Run008.

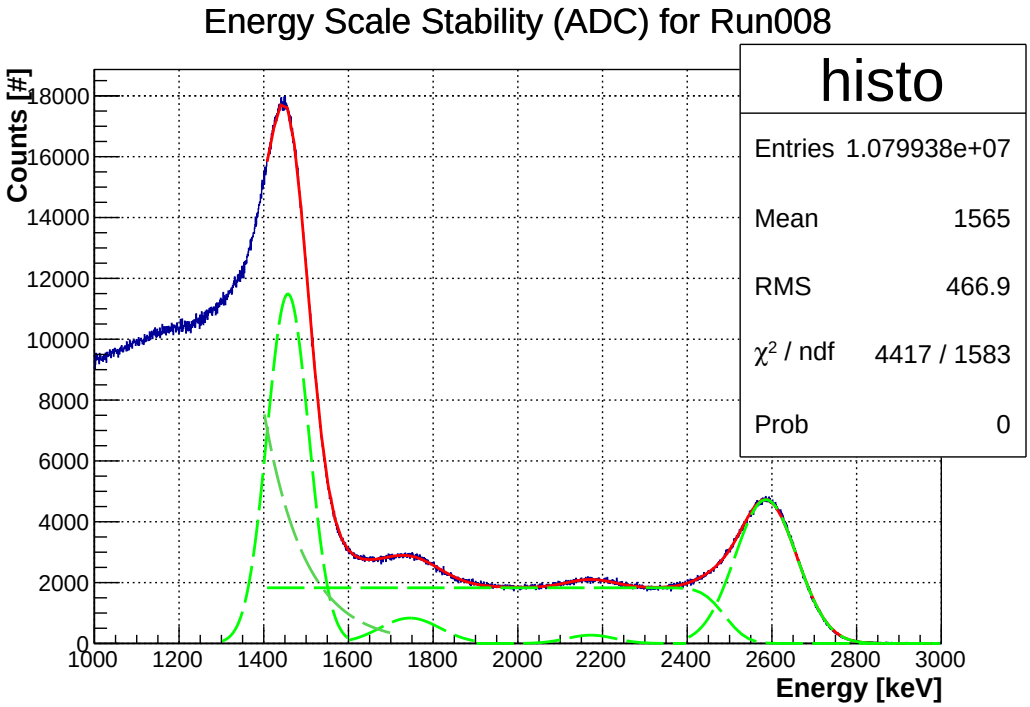

Figure A.2.: ADC energy spectrum for the whole data of Run008.

A.1.2. Peak energy histogram for individual Subrun peaks

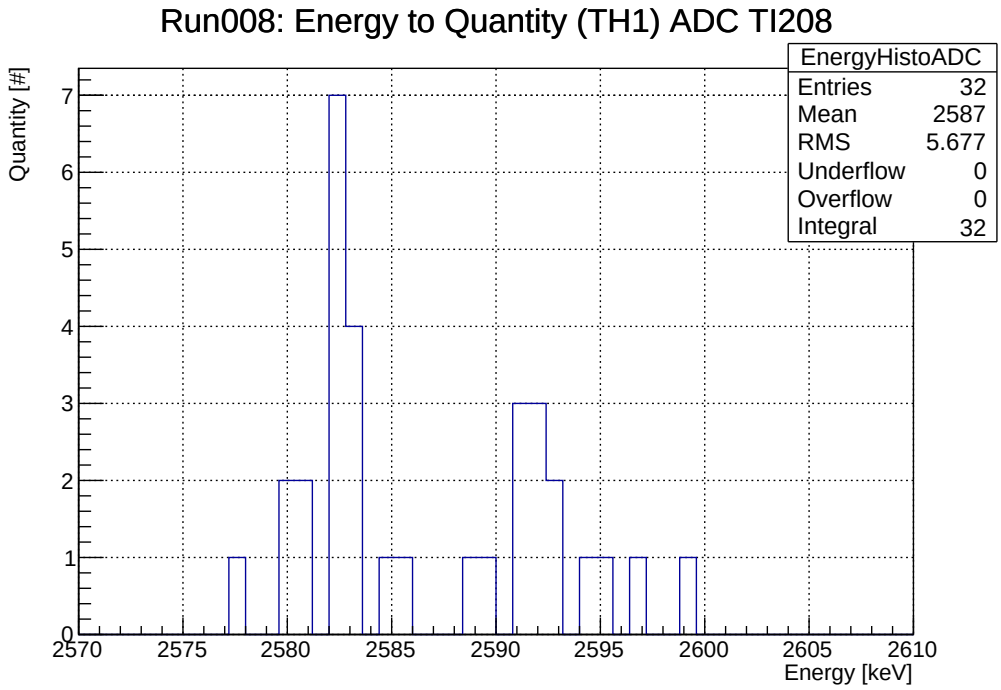

Figure A.3.: ADC energy spectrum for ^{208}Tl that contains the peak positions of all Subruns. RMS/Mean = 0.21%.

A.1.3. Event rate histogram for individual Subrun rates

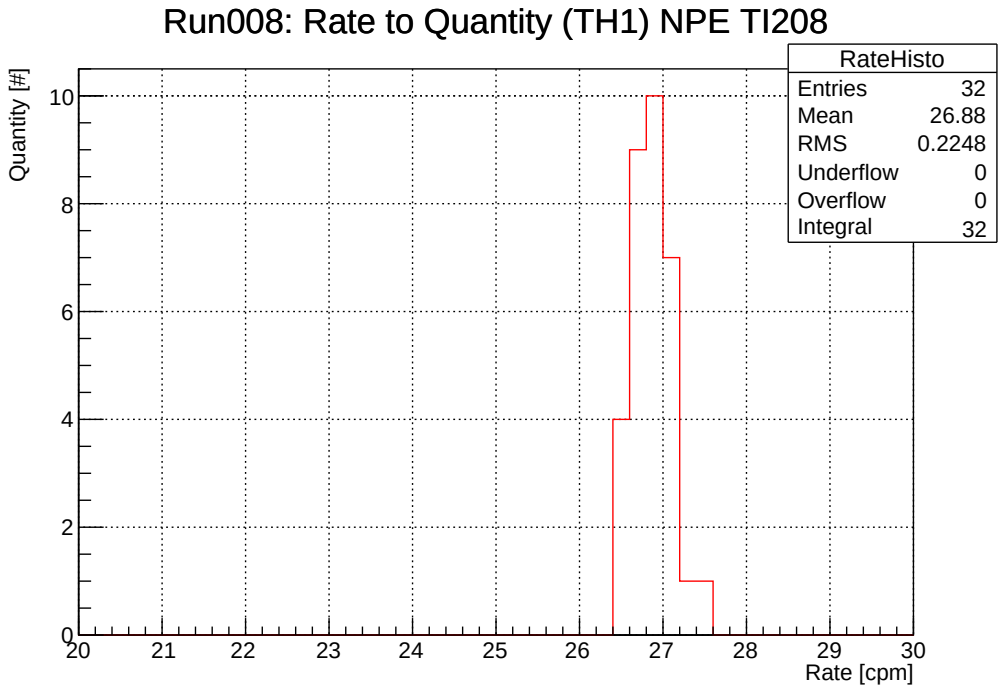

Figure A.4.: NPE event rate histogram for ^{208}Tl that contains the calculated event rates of all Subruns. RMS/Mean = 0.84%.

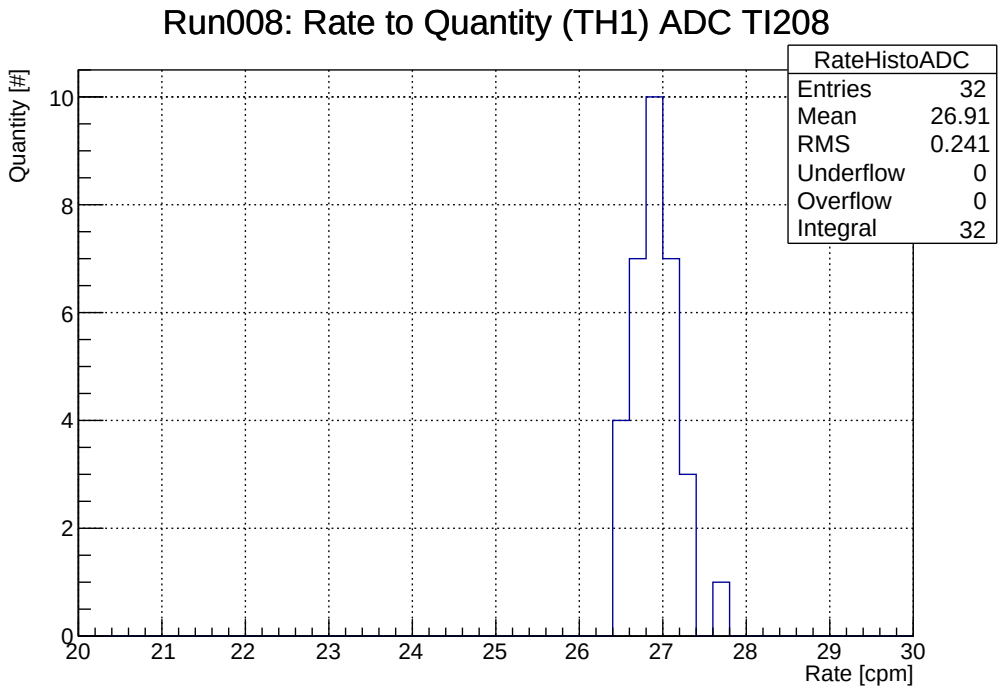

Figure A.5.: ADC event rate histogram for ^{208}Tl that contains the calculated event rates of all Subruns. RMS/Mean = 0.89%.

A.2. Analysis for Run009

A.2.1. Combined Subrun spectrum for NPE

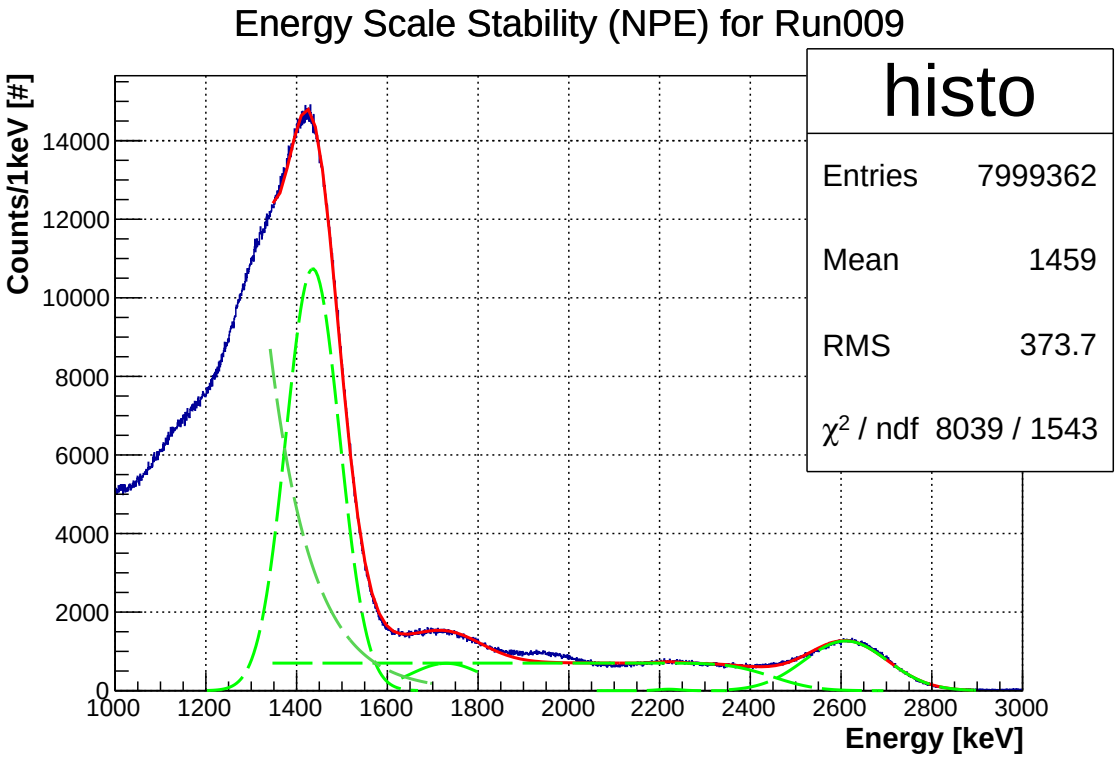

Figure A.6.: NPE energy spectrum for the combined Run009 data (Subrun 69-158).

A.2.2. Energy peak fluctuations

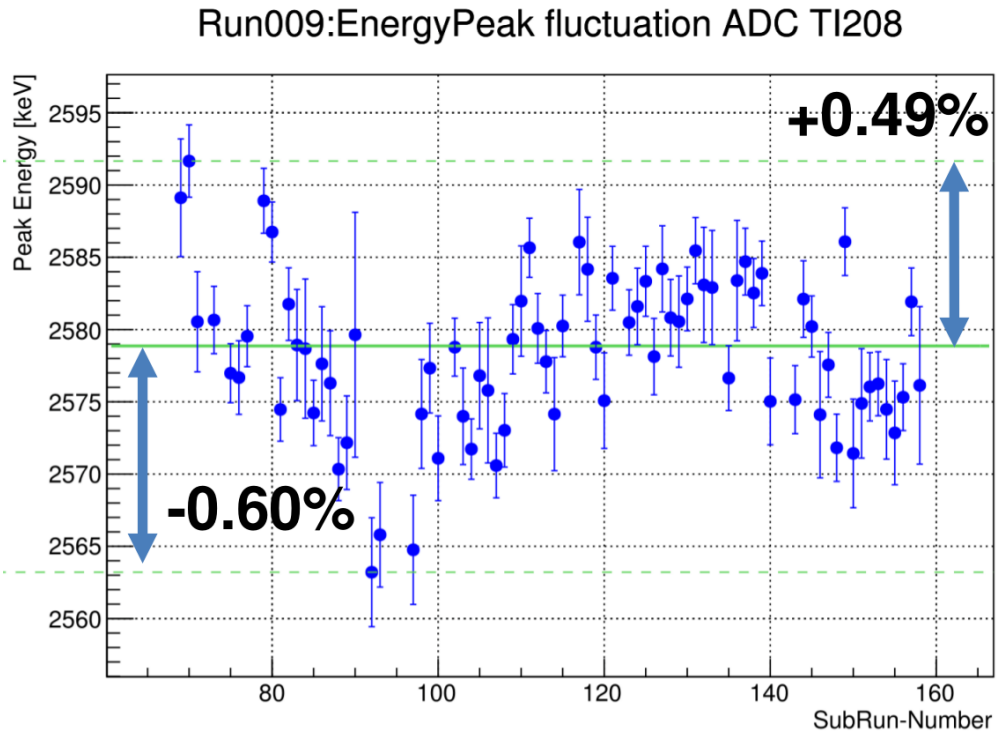

Figure A.7.: ^{208}Tl peak energies (ADC) for each Subrun. The fluctuation of the peaks is estimated with a horizontal fit (green).

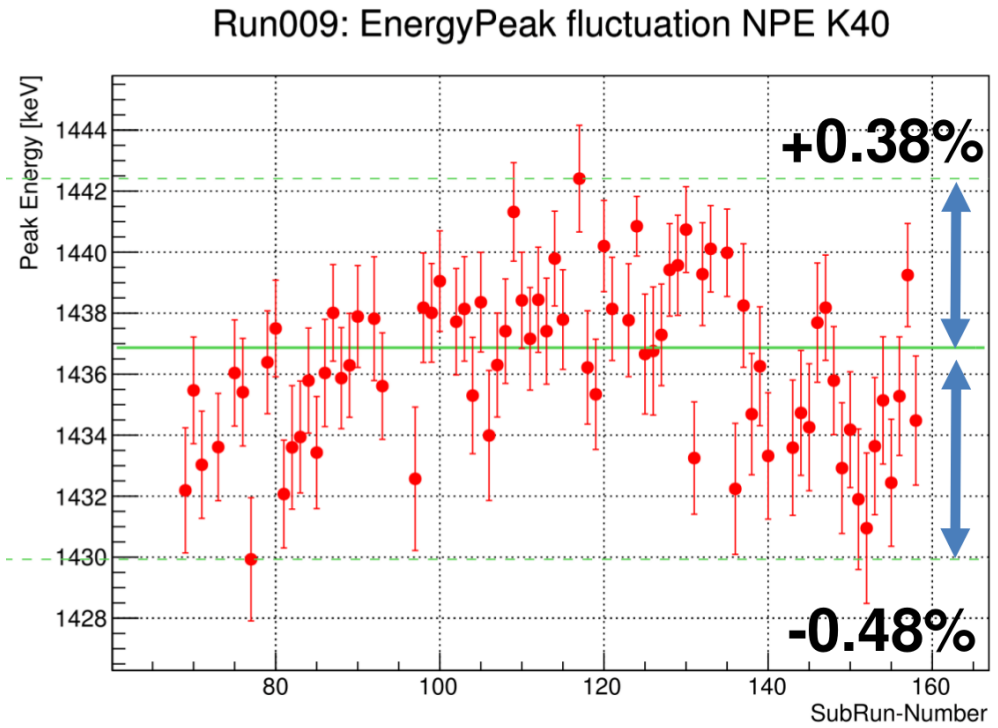

Figure A.8.: ^{40}K peak energies (NPE) for each Subrun. The fluctuation of the peaks is estimated with a horizontal fit (green).

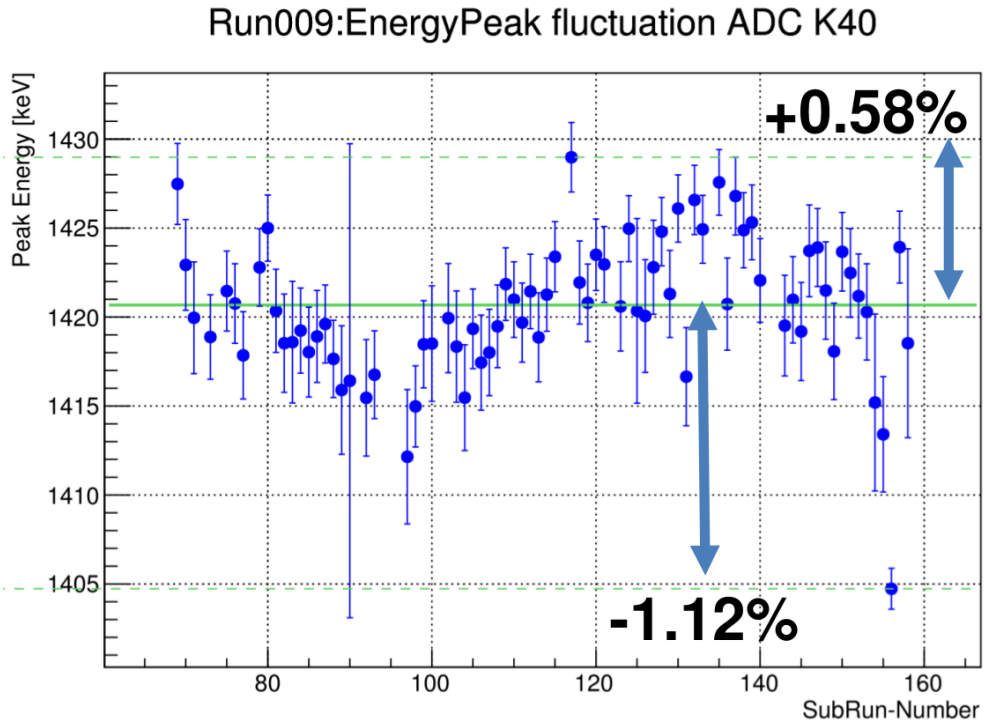

Figure A.9.: ^{40}K peak energies (ADC) for each Subrun. The fluctuation of the peaks is estimated with a horizontal fit (green).

A.2.3. Event rate fluctuations

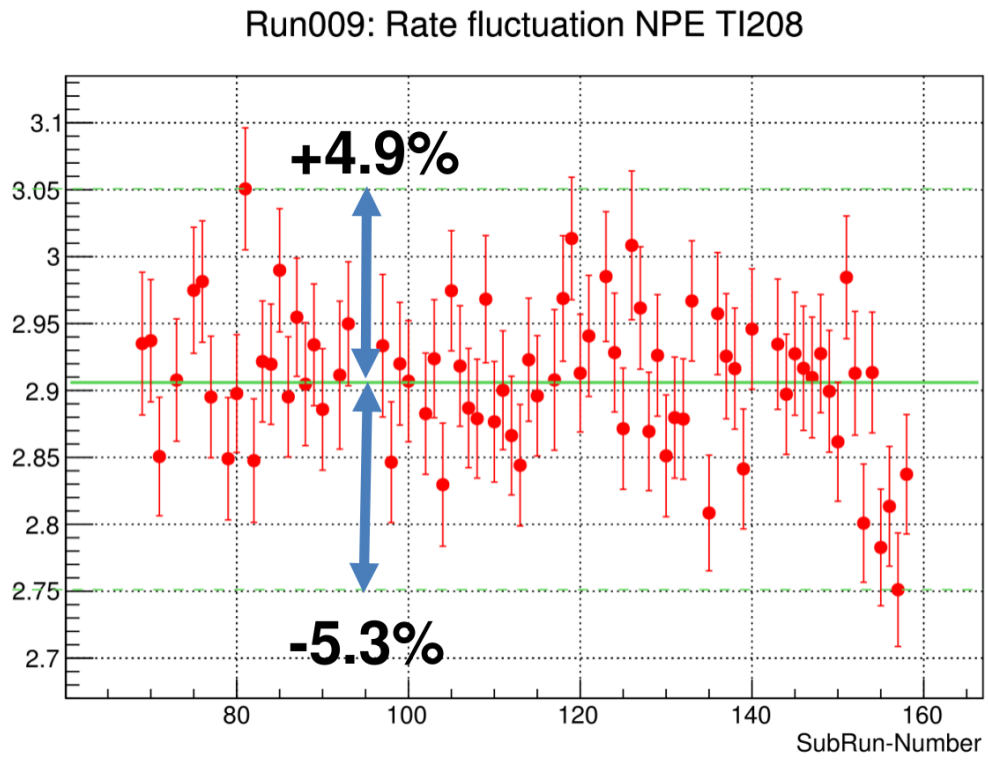

Figure A.10.: ^{208}Tl event rates (NPE) for each Subrun. The fluctuation of the event rate is estimated with a horizontal fit (green).

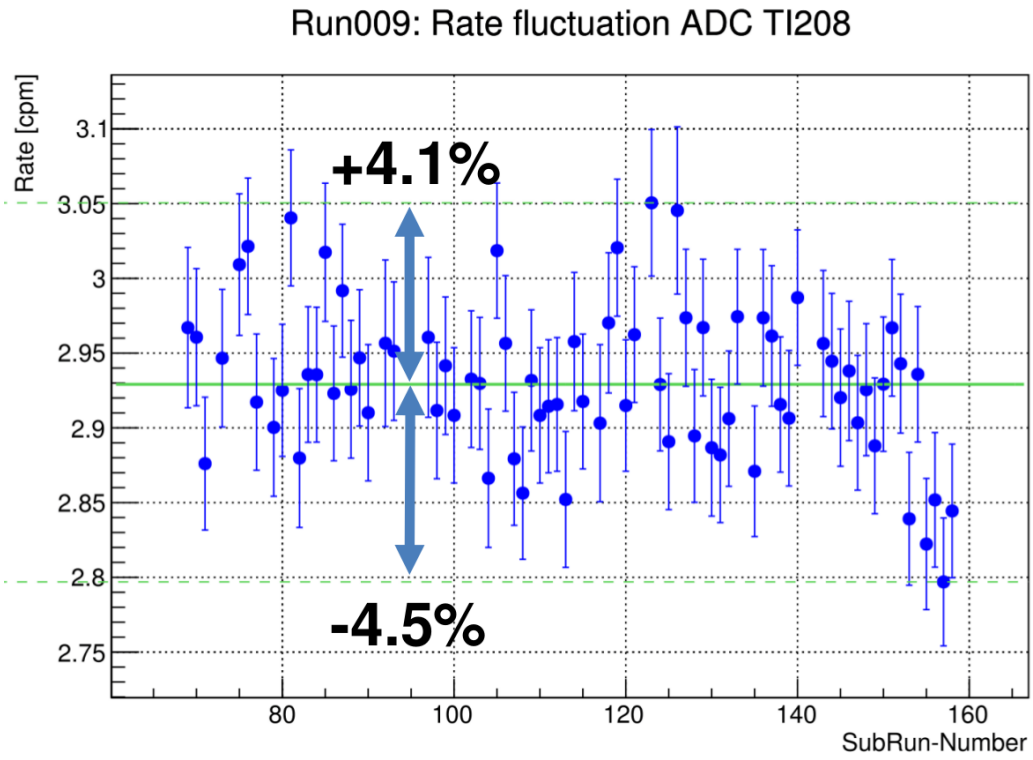

Figure A.11.: ^{208}Tl event rates (ADC) for each Subrun. The fluctuation of the event rate is estimated with a horizontal fit (green).

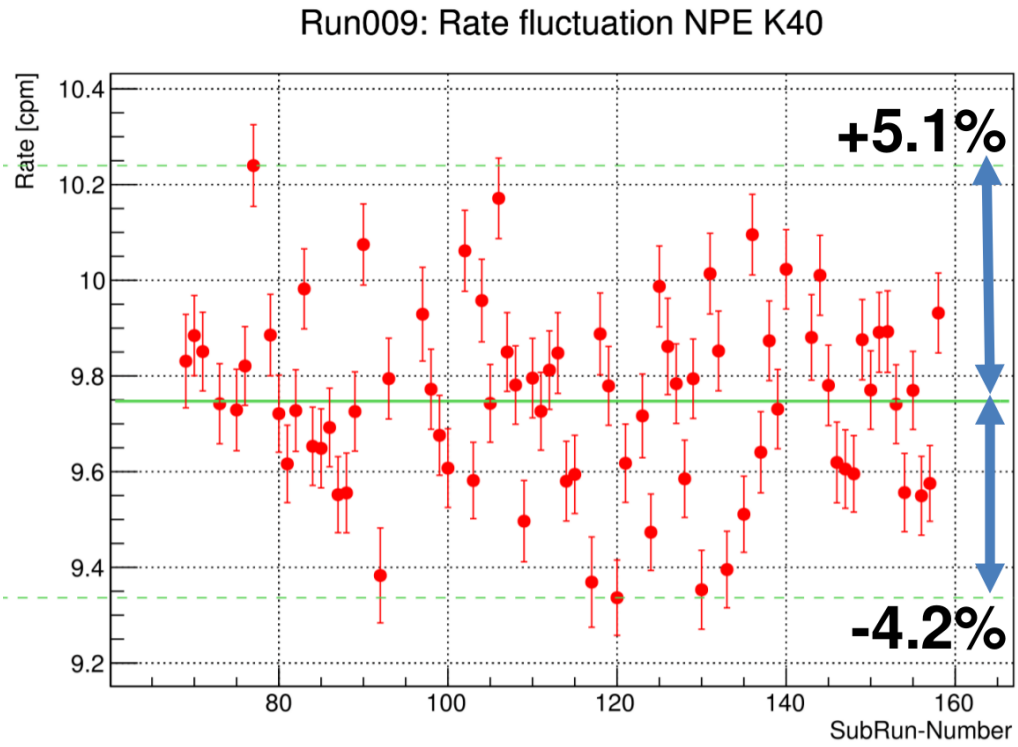

Figure A.12.: ^{40}K event rates (NPE) for each Subrun. The fluctuation of the event rate is estimated with a horizontal fit (green).

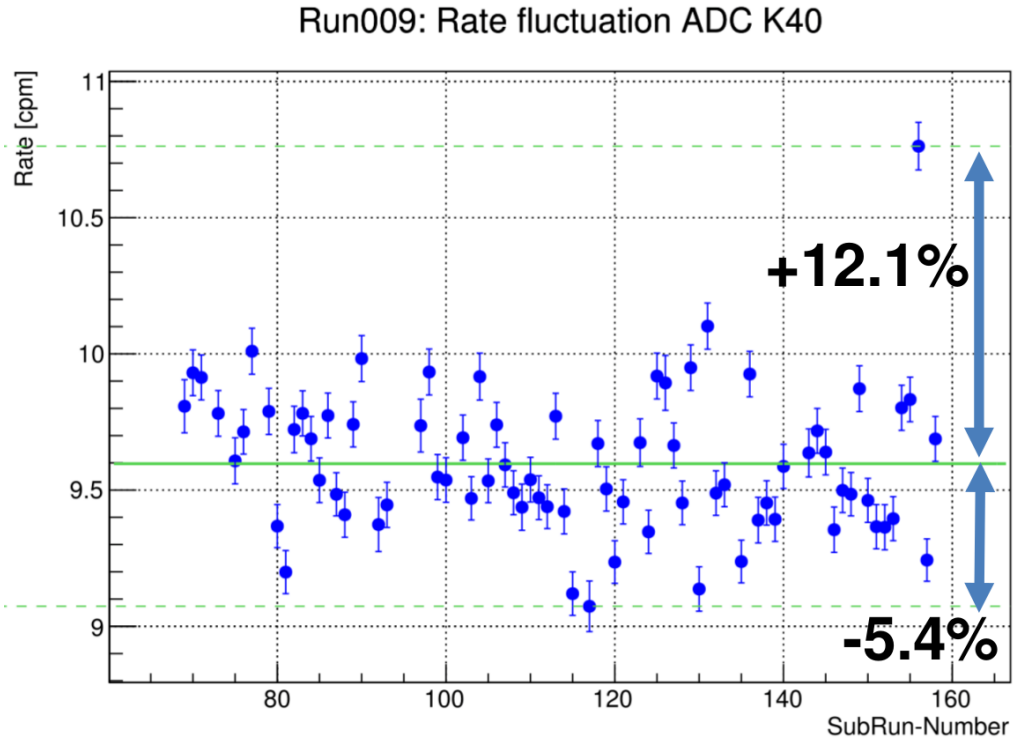

Figure A.13.: ^{40}K event rates (ADC) for each Subrun. The fluctuation of the event rate is estimated with a horizontal fit (green).

B. (n, γ) background study plots

B.1. ^{252}Cf data analysis

B.1.1. Study with a Ratio4us cut

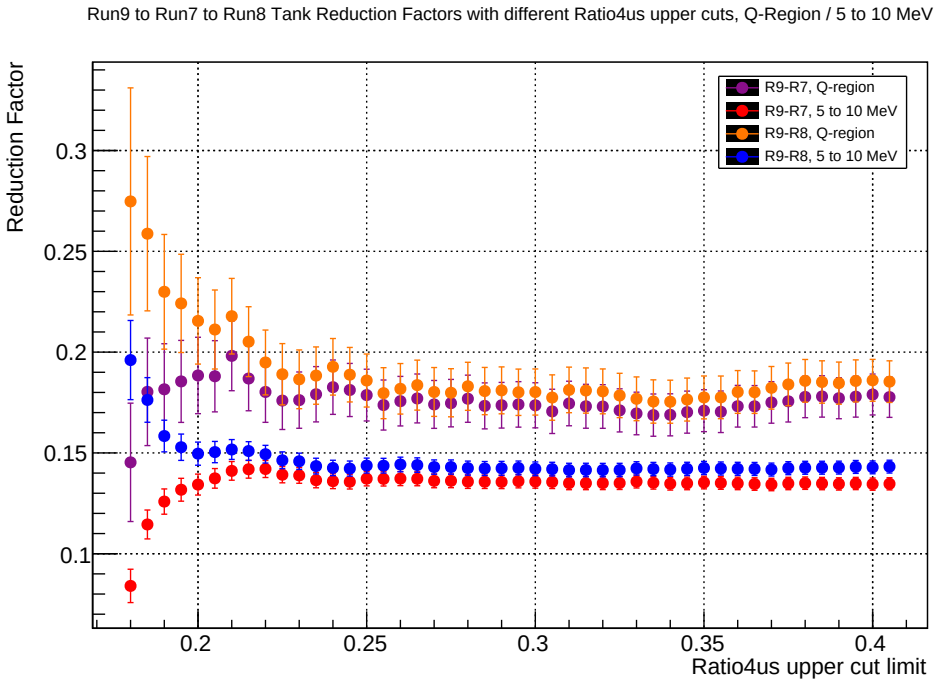

Figure B.1.: ^{252}Cf "Tank" run reduction factors based on different Ratio4us upper cuts. The reduction factors of Run007/Run008 to Run009 for the Q-region are shown in purple/orange, while the reduction factors for the 5 MeV to 10 MeV region are shown in red/blue. The error bars are calculated and propagated based on the assumed poisson statistics ($\sqrt{N}$). It can be seen that the reduction factors are stable after a Ratio4us upper cut of 0.25. Below a value of 0.2, the reduction of Run007 to Run009 gets better, similar to the "Rock" run results. In the case of Run008 to Run009 though, the reduction gets worse. This could be based on the small difference in Ratio4us peak shapes of Run007 and Run008 though. A further study has not been executed, as the final reduction values will be derived based on the Physics run data with a χ^2_β cut.

B.1.2. Study with a χ^2_β cut

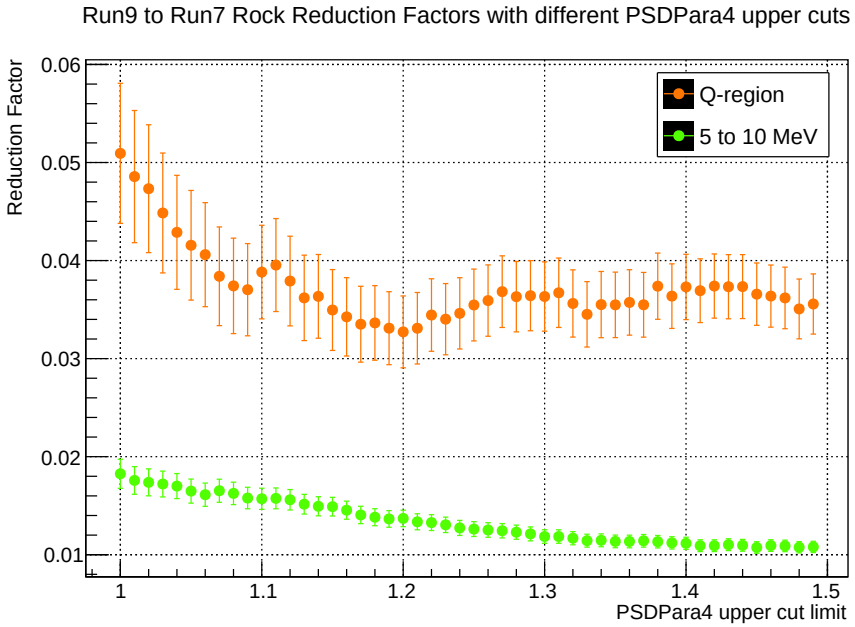

Figure B.2.: ^{252}Cf "Rock" run reduction factors based on different χ^2_β upper cuts. The cuts for each run are made at the same detection efficiency and the shown χ^2_β value is based on Run007. It can be seen that the reduction factors are stable in a reasonable upper cut region (1.3-1.5), if one wants to make a tighter cut (< 1.5) for the 0νββ analysis. Upper cuts lower than 1.3 are already in the χ^2_β peak region of β events and should be neglected.

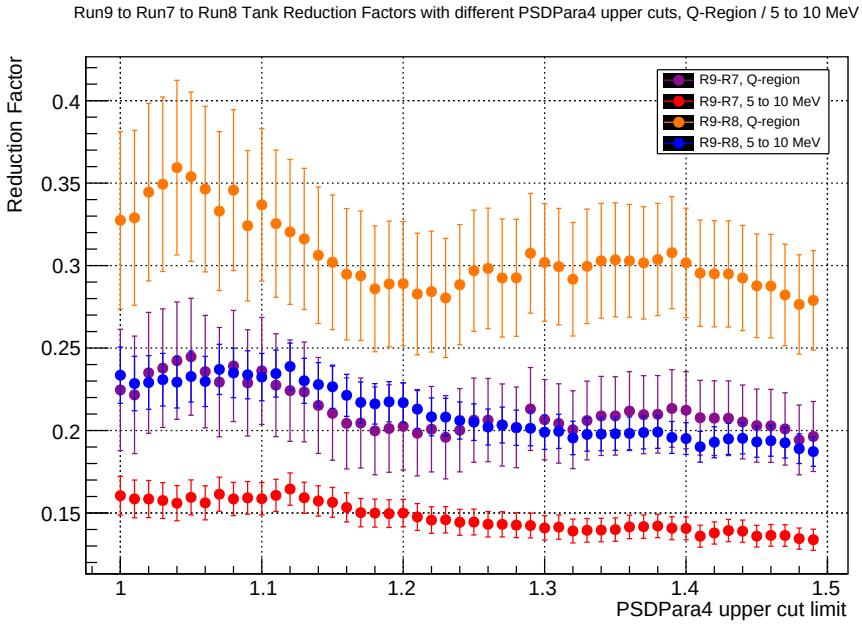

Figure B.3.: ^{252}Cf "Tank" run reduction factors based on different χ^2_β upper cuts. The cuts for each run are made at the same detection efficiency. It can be seen that the reduction factors are stable in a reasonable upper cut region (1.3-1.5).

B.2. Physics run data analysis

B.2.1. Systematic error by χ^2_β cut

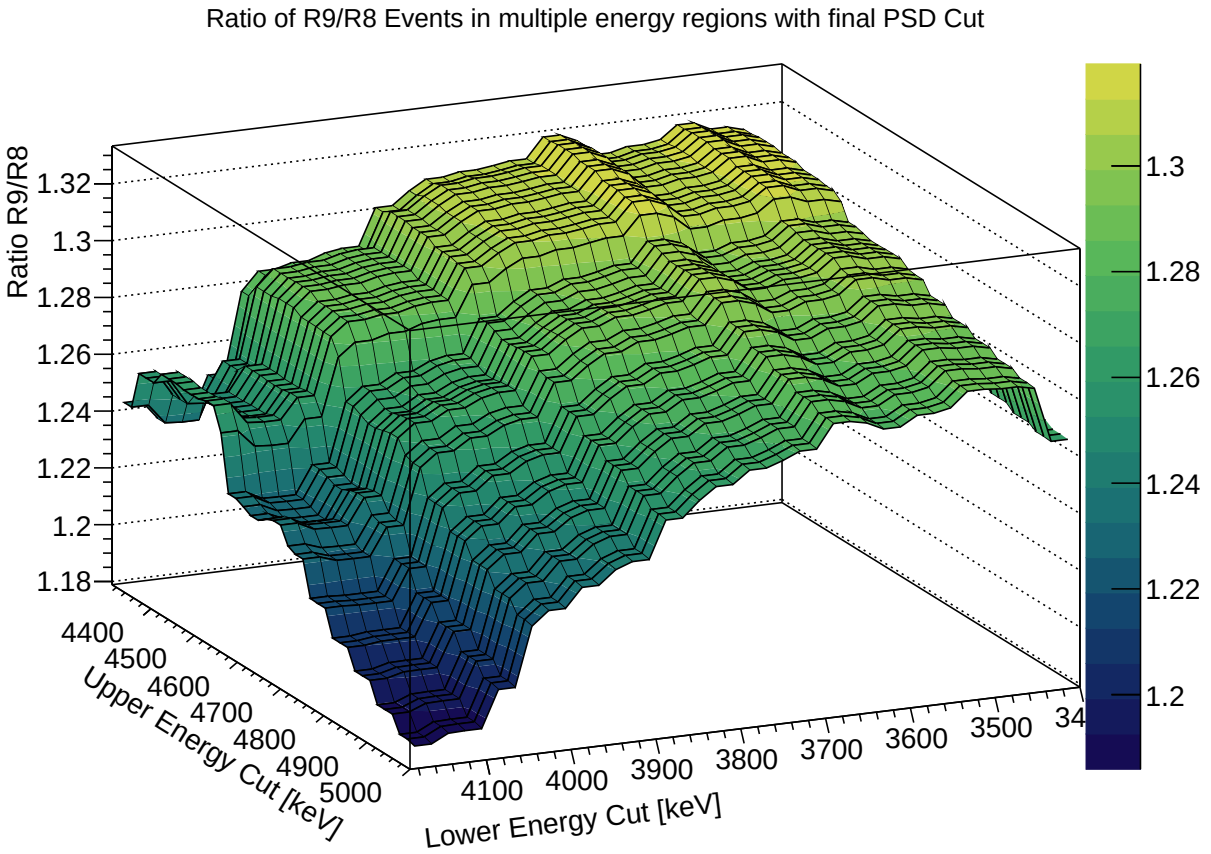

Figure B.4.: Ratio of Run009 to Run008 events in multiple energy regions with the final same χ^2_β rejection efficiency cut. The averaged ratio, derived by a fit, is 1.28.

Statutory Declaration

I declare that I have developed and written the enclosed thesis entirely by myself and have not used sources or means without declaration in the text. Any thoughts or quotations which were inferred from these sources are clearly marked as such. This thesis was not submitted in the same or in a substantially similar version, not even partially, to any other authority to achieve an academic grading and was not published elsewhere.

Michael Moser Erlangen, March 17, 2017

Acknowledgements

At last, I'd like to thank everybody that helped and assisted me in the course of this master thesis and my stay in Japan. I'd especially like to thank:

my family — für die herausragende Unterstützung in meinem Studium und insbesondere während des Auslandsaufenthalts. Eigentlich ist das selbsterklärend, aber ohne euer liebevolles Engagement wäre kein Teil meines Studiums möglich gewesen. Auch unsere gemeinsame Rundreise in Japan war eines meiner Highlights. Deswegen möchte ich euch, Papa, Mama und Christina, nochmal von allen Herzen danken.

Prof. Takashi Iida — for the outstanding support and guidance in my research. You were always open minded for any questions or issues that I had. Working with you has been a pleasure! Additionally, I'll certainly not forget all of the fantastic parties that we had. Let's have another one at a conference some day in the future!

Takaki Ohata — for the stellar assistance during my stay at the lab. No matter which question I had, you've always helped me immediately. Without your help and supporting analysis, this work would not have been possible. I'm deeply grateful for your kindness during my stay.

Prof. Tadafumi Kishimoto — for the possibility to conduct my research in your laboratory, the kind supervision and your helpful comments on my work. Thank you very much!

Prof. Gisela Anton — für die hervorragende Betreuung und Unterstützung meiner Arbeit. Sie hatten immer ein offenes Ohr für mich, egal um welches Thema es sich handelte. Vielen Dank dafür, ich freue mich schon auf die Promotion!

Prof. Kyohei Nakajima — for the generous support on the CANDLES detector simulation and the useful comments on my presentations. Thanks a lot!

Dr. Thomas Eberl — für die sofortige Bereitschaft, der Zweitgutachter dieser Arbeit zu werden. Vielen, vielen Dank Thomas!

my friends in Japan — for all of the outstanding friendships that I could make. Caro, Fatma, Mas, Abzal, Tem, Wylla, Lakmin, Junko & Takaji Sasaki (and the family in general!), Trang, my OUISA family, ... the list could go on forever. Thank you very much for your friendship and for making my stay in Japan so enjoyable! I'll see you again one day in the future!